VUV source for two-color dynamics studies at FLASH2

Von der Fakultät für Mathematik und Physik
der Gottfried Wilhelm Leibniz Universität Hannover

zur Erlangung des akademischen Grades

Doktor der Naturwissenschaften
- Dr. rer. nat. -

genehmigte Dissertation von

M.Sc. Elisa Appi

2021

Referent:	Prof. Dr. Milutin Kovačev
Korreferent:	Prof. Dr. Uwe Morgner
Korreferent:	PD Dr. Robert Moshammer
Tag der Promotion:	19.07.2021

Abstract

Free electron lasers (FELs) and high order harmonic generation (HHG) sources produce ultrafast coherent extreme ultraviolet (XUV) and X-ray radiation. These two powerful sources are optimal tools for time-resolved studies of ultrafast dynamics due to their high spatial and temporal resolution. Common time-resolved studies make use of pump-probe schemes, where a first pulse triggers a dynamics and a second delayed pulse probes the status of the target at a known moment in time. Split-and-delay units are often employed in order to separate the pump and probe pulses provided by a single high photon flux source. Alternatively, a second synchronized source can be added for two-color experiments. In this case, the two photon energies are chosen accordingly to the process under investigation. Typically, the spectral range covered by secondary sources spans from the ultraviolet to the THz range. However, the parameter space can be extended by combining two separate short-wavelength systems, such as a FEL and a HHG-based beamline. Such configuration benefits from the sources complementary properties, opening a new regime for two-color studies in the XUV/X-ray range.

The permanent integration of a HHG-based source in a FEL endstation was recently realized for the first time at the free electron laser FLASH and is presented in this thesis work. Preliminary studies on the source configuration and pressure calculations allowed to design a compact and reliable system, able to encounter the challenging vacuum requirements given by the ultra high-vacuum FEL endstation. The HHG process is driven by a OPCPA laser system, synchronized with the unique FEL burst timing, which delivers femtosecond pulses used for the generation of vacuum ultraviolet (VUV) light in a gas target. The emitted radiation is resolved in a compact in-line spectrometer and can be spectrally tuned by means of a rotatable double filterwheel. A hyperboloidal carbon-coated mirror allows for the coupling in the FEL endstation where the VUV beam is focused into a reaction microscope (REMI). First commissioning results have shown the generation of radiation from 10 to 40 eV with pulse energies up to 0.1 nJ and the successful focusing in REMI down to a 20 µm diameter spot. Photo-electron momentum measurements in argon indicate the source capabilities for future pump-probe experiments.

Keywords: nonlinear optics, high-order harmonic generation, free electron lasers, two colors pump-probe schemes, time-resolved studies.

Contents

1 Introduction **1**

1.1 Outline 3

2 Ultrafast coherent X-ray sources **5**

2.1 Free-electron lasers 5

2.2 High order harmonic generation sources 12

2.2.1 Driving laser technologies 12

2.2.2 Modern advances in HHG technology 13

2.2.3 State-of-art harmonic sources at high repetition rates. . . 14

2.3 Time-resolved studies 17

3 HHG theory **21**

3.1 Nonlinear properties of light-matter interaction 21

3.2 Introduction to high order harmonic generation 23

3.2.1 Single-atom response 23

3.2.2 Macroscopic effects 27

3.3 Energy scaling principle for HHG 31

4 Semi-infinite gas cell as HHG generation configuration **35**

4.1 Basic generation principles in SIGC 35

4.2 Generation at limited pulse energy 37

4.2.1 Signal optimization 40

4.2.2 Energy scaling test 44

5 VUV beamline at FLASH2 **49**

5.1 FL26 beamline 49

5.2 VUV beamline 51
5.2.1 Driving laser optical setup 53
5.2.2 HHG source 57
5.2.3 Filterwheel 60
5.2.4 Inline spectrometer 61
5.2.5 Incoupling mirror 64
5.2.6 Differential pumping system 68

6 Beamline performance **75**
6.1 VUV generation 75
6.1.1 Spectral components 76
6.1.2 VUV pulse energy 81
6.2 Incoupling in the FEL beamline 86
6.3 Commissioning experiment in REMI 89
6.4 Development perspectives for the VUV beamline 94

7 Conclusion **97**
7.1 Summary 97
7.2 Outlook 98

Bibliography **100**

Chapter 1

Introduction

The study and understanding of the inner structure of matter strongly depends on the available temporal and spatial resolutions of the investigation methods. While macroscopic objects can be perceived with our own senses, the development of specialized techniques and detectors allows to enhance our observation capabilities in terms of resolution. The smaller the object under study, the more challenging the investigation becomes. On the microscopic scale, the study of atoms, molecules and their dynamics presents ongoing challenges even to modern cutting-edge research.

Optical science provides fundamental tools for the investigation of matter via the study of light-matter interactions. For instance, intense light pulses enable the investigation of ultrafast dynamics at the molecular and atomic scale. The evolution of dynamics is resolved in time by employing pump-probe schemes [Zew00]: a first pump-pulse triggers a response in the sample, while a second time-delayed pulse probes the sample's state at a specific known time. The delay of the probe-pulse is then varied in the time interval of the dynamics under investigation. Since the time resolution is limited by the temporal duration of the pulses, the pulse duration must be chosen accordingly. Typically, rotational motion of molecules can be resolved with picosecond pulse durations, but vibrational motion and fragmentation dynamics during chemical reactions require pulses in the femtosecond range [Zew00; Kra+18], while electronic dynamics happens in the attosecond time scales [Cal+16].

Particular interest is given also towards short-wavelengths sources. Extreme ultraviolet (XUV) and X-ray sources provide high energetic photons, ideal to investigate direct electronic excitations and ionizations in atoms or molecules down to inner-shell energetic levels. The applications span over a large range of topics, including fundamental atomic and molecular physics [MS20; Cal+21], condensed matter physics [ZDS18; Iri+20] and photochemistry [URM12; Cha+20]. The penetrating properties of this spectral range is also used for imaging of objects with micrometer and nanometer resolution. X-ray crystallography [SM00] and coherent diffraction imaging (CDI) [MSS12] are commonly applied, for instance, to the study of biologic samples [Kim+14].

Nowadays, different types of ultrafast short-wavelength light sources are available. An example of laboratory-accessible systems are laser-driven plasma sources. They usually generate incoherent hard X-ray pulses in the femtosecond regime and are commonly employed in diffraction studies of crystalline structures [Bra+07; Hol+16]. Ultrafast lasers can also be used to drive high order harmonic generation (HHG). This nonlinear process generates a broad coherent spectrum of harmonic orders of the fundamental wavelength via strong-field laser interaction with a target. HHG provides pulses with high temporal and spatial coherence properties [Sal+99; Ben+14] in spectral regions currently not accessible to conventional lasers, including the XUV and soft X-ray spectral range [Mak+20; Fu+20]. The process allows also for the generation of attosecond pulses trains [Pau+01] as well as isolated attosecond pulses [Hen+01]. HHG-based sources are extensively used in many scientific fields. Their range of applications is very broad and includes attosecond physics [PMV19; Li+20], subwavelength coherent imaging [Gar+17], ptychography of nanopatterns [Tru+18] and precision metrology [Pup+21].

In addition, over the last 30 years there has been a remarkable development of accelerator-based sources in large-scale facilities. Synchrotron sources make use of high-energy electrons, confined in storage rings by a magnetic field, for the generation of bright, spectrally-tunable X-ray radiation. They are employed in time-resolved studies of chemical and structural dynamics on nanosecond timescales with applications, for instance, in protein microcrystallography [Yam+17], fluid dynamics [KP14] and imaging for medical applications [ST03]. Recent results have shown also the generation of femtosecond synchrotron pulses via modulation of the electron energy by an external ultrafast laser source [Sch+00].

Femtosecond X-ray pulses are also provided by free electron lasers (FEL), which are another type of accelerator-based source. Unlike synchrotrons, FELs provide coherent radiation in the soft and hard X-ray range, orders of magnitude brighter than previous X-ray sources [HZS19; Sch+19d]. These features make FELs powerful tools in the investigation of dynamics at time and length scales of atomic interactions with a large range of applications [Sed+17]. Common schemes for time-resolved studies at FEL facilities make use of split-and-delay units to temporally separate pump and probe pulses from a single FEL beam [Cas+13; Erk+18; Din+21a]. As an alternative, a secondary source, such as an ultrafast laser temporally synchronized to the FEL, can provide either the pump or the probe pulse allowing for two-color schemes [RR15; Zap+18; Bia+21a]. In this approach, the photon energies of the two pulses can be chosen accordingly to the dynamics under investigation. The spectral range typically covered by secondary sources available at FEL facilities spans from the deep ultraviolet to the THz range [Red+11; Sch+15; Lan+19; Sch+19a].

The parameter space for pump-probe experiments can, however, be extended by combining a HHG-based source with a FEL beamline, opening a new regime for two-color time-resolved studies in the XUV-X-ray spectral range at femtosecond timescales. This combination was recently realized for the first time in a permanent installation at the free-electron laser FLASH in Hamburg. A vacuum ultraviolet (VUV) source has been integrated in the FEL beamline FL26, which features a reaction microscope (REMI) endstation [Sch+19c]. The realization of this novel and unique setup has been the objective of this work. Detailed design, alignment procedure and first proof-of-principle results are described along the thesis. This unique configuration has the potential to be a valuable tool in the investigation of the inner structure of matter, in particular for electron and core-level ionization dynamics in atomic and molecular targets. It will be soon employed for first FEL-pump HHG-probe transient absorption spectroscopy experiments targeting intra-molecular electron dynamics in the oxygen molecule O_2.

1.1 Outline

The work presented in this thesis comprises the design, installation and first commissioning results of the new VUV beamline at the free-electron laser FLASH in Hamburg. In particular, chapter 2 presents the scientific framework

behind the thesis, providing a general overview of state-of-art short-wavelength free electron lasers and high order harmonic generation sources. Chapter 3 dives deeper into high order harmonic generation in gas media with a short introduction to the principles behind the process and presenting a recent energy scaling approach for efficient generation in single-pass sources at high repetition rates ($\gg$1 kHz). Based on these theoretical considerations, preliminary experimental studies on the source geometry, presented in chapter 4, are used to test the underlying concept of operation for the new VUV beamline. Finally, chapter 5 presents the complete technical design of each section of the VUV beamline, including the generation configuration, the incorporated detectors and the integration with the FEL endstation. First commissioning results, comprising the beamline performances and proof-of-principle studies on photoionization of argon atoms in the reaction microscope, are shown in chapter 6. At the end of this work, chapter 7 summarizes the presented results and gives an outlook on improvements and future applications.

Chapter 2

Ultrafast coherent X-ray sources

Ultrafast light sources in the extreme ultraviolet (XUV) and X-ray spectral region prompted great progress in many fields of science, opening new prospects in the investigation of molecular and atomic structure of matter [PSG06]. Two main complementary alternatives have been developed very successfully: accelerator-based and laser-driven sources. The first approach relies on the emission of radiation from high energetic particles which are accelerated to relativistic velocities, and is mostly implemented in large-scale facilities such as synchrotrons. On the contrary, laser-driven sources are a laboratory-scale technology based on ionization of gas or solid targets from an intense laser pulse. In this chapter, the attention is focused on free-electron lasers (FEL) and high order harmonic generation (HHG) sources due to their advantage to provide coherent femtosecond radiation. A basic overview of available table-top FEL and HHG sources is presented.

2.1 Free-electron lasers

The operation of a free-electron laser is based on the propagation of relativistic electrons through a periodic magnetic structure, called undulator. The electrons oscillate in the periodic magnetic field and spontaneously emit electromagnetic radiation. The emission depends on the properties of the undulator strength

parameter K, which is defined as:

$$K = \frac{eB_0\lambda_u}{2\pi mc}, \tag{2.1}$$

where B_0 is the peak magnetic field strength, λ_u the period of the undulator magnetic field, m the electron mass and c the speed of light in vacuum. The electron beam of energy γmc^2, where γ is the Lorentz parameter, emits electromagnetic radiation at the wavelength λ, given by:

$$\lambda = \frac{\lambda_u}{2\gamma^2}\left(1 + \frac{K^2}{2} + \gamma^2\theta^2\right), \tag{2.2}$$

where θ indicates the emission angle with respect to the undulator axis z. For $K > 1$ harmonics of the fundamental radiation are also generated [MBM16; HK00]. Since the emitted wavelength depends on the magnetic field properties and the electrons energy, it can be continuously tuned within a wide spectral range and extended towards regimes not accessible by conventional lasers, such as XUV and X-ray. By making used of this emission process, free-electron laser oscillators can be built employing an optical cavity and using the electron beam in the undulator as gain medium. The first realization of this principle was achieved by Madey and colleagues in the 1970s [Mad71; Dea+77], which demonstrated the generation of coherent infrared radiation. However, it was soon discovered that amplification is also possible via interaction of the emitted radiation with the high energetic electron beam in a single-pass configuration. For a sufficiently long undulator, this interaction induces a periodic density modulation of the electrons (bunching), which results in an intense coherent emission [KS80; BPN84]. No optical cavity or external seeding is required for the amplification process, which is called self-amplified spontaneous emission (SASE). A schematic of the SASE working principle is presented in Fig. 2.1. In a one-dimensional model, the emitted radiation power $P(z)$ grows exponentially with the undulator length z [HK07] as $P(z) \propto \exp(z/L_{gain})$, where L_{gain} is the gain length [Sch+19d] defined by:

$$L_{gain} \approx \frac{\lambda_u}{4\pi\sqrt{3}\rho}, \tag{2.3}$$

with ρ indicating the, so-called, FEL Pierce parameter [BPN84]. At saturation, the peak power is approximately:

$$P_{sat} \approx \frac{\rho\gamma mc^2 I_p}{e}, \tag{2.4}$$

where I_p is the electron peak current and $\rho \propto I_p^{1/3}$ characterizes the efficiency of the process in terms of the electron beam power. Therefore, short undulator periods and high electron peak current allow to reach saturation with shorter undulator lengths leading to more compact apparatuses [HL12].

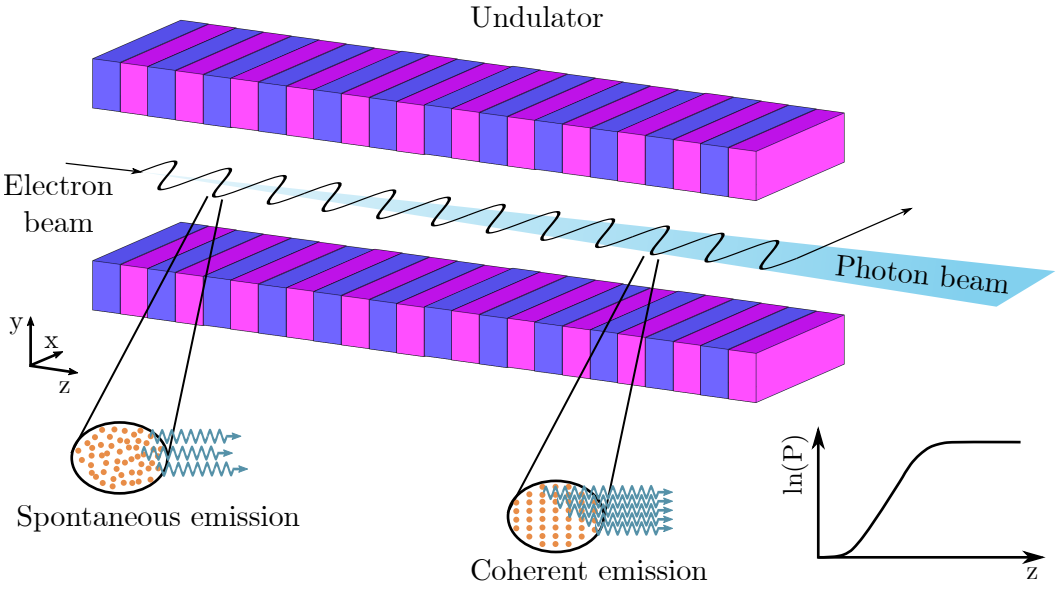

Figure 2.1: Working principle of a high-gain FEL based on SASE. The high energetic electron beam is injected in an undulator. The periodic magnetic field induces spontaneous emission of photons. For a sufficiently long undulator, the interaction of the spontaneously emitted radiation with the electron beam leads to a modulation (micro-bunching) of the electron density and to coherent emission.

While the SASE process leads to good spatial coherence with the selection of a dominant fundamental mode [SSY08; Sin+12], the temporal coherence of the emitted radiation is limited. The time structure of the emitted FEL pulse is determined by the random emission of initial photons which then leads to the amplification. The coherence time can be expressed as:

$$\tau_{coh} \approx \frac{\lambda}{4\pi\rho c} \tag{2.5}$$

and it is proportional to the wavelength λ emitted. Typically the coherence time varies from a few femtoseconds for emission in the XUV [Sin+12] down to below hundred attoseconds in the hard X-ray regime [Zho+20]. Each FEL pulse consists then in many temporal coherent spikes of duration τ_{coh} but with no fixed phase relation to each other. The FEL temporal coherence properties can be improved by triggering the SASE process with a controlled initial photon

pulse [Lam+09]. The seeding pulse can be obtained in the first part of the FEL itself [Ama+12] or it can be provided by an external source [Yu+00].

Nowadays, several facilities worldwide can provide coherent or partially coherent femtosecond pulses in the XUV, soft and hard X-ray wavelength range with peak powers up to the Gigawatt level. In the following, a short overview of the main FEL facilities, and their parameters, is presented. For a complete review see, for instance, [Sed+17; FD18; Sch+19d].

FLASH. The free-electron laser FLASH at DESY in Hamburg holds the record of being the first XUV and soft X-ray FEL [Ayv+06]. It delivers pulse energies in the range from 0.01 to 1 mJ with femtosecond pulse durations in the 10-300 eV [Ack+07]. Differently from other facilities, FLASH operates in a burst-mode where macro-pulses at 10 Hz contain up to 800 micro-pulses. The intra-burst repetition rate of the micro-pulses can be tuned in the kHz up to MHz range, enabling high repetition rate experiments [RSW19]. Two different FEL lines, FLASH1 and FLASH2, are available for users. During parallel operation, the photon energy delivered by FLASH2 can be tuned, by means of variable-gap undulators, around the FLASH1 wavelength. Additionally, the upgrade program *FLASH2020+* will provide significant improvements to the facility [Röh+19]. Fully parallel operation will be achieved due to tunable undulators in both FEL lines. The available spectral range will be increased by external seeding and will cover the full water window (from ∼282 to 533 eV).

LCLS. The LCLS, at the SLAC National Accelerator Laboratory in Stanford, is in operation since 2009. It is the first FEL to provide radiation in the hard X-ray range, with wavelength down to 1.5 Å [McN09; Emm+10]. Currently, it provides pulse energies up to 4 mJ over the spectral range from 280 eV to 11.2 keV at 120 Hz. Within the ongoing LCLS-II upgrades [BDS19], the repetition rate will be increased up to 1 MHz, while the operating photon energy range will be extended up to 25 keV. These improvements will affect fundamental components of the machine, such as a new variable-gap undulator system and implementation of seeding technologies in order to increment spacial and temporal coherence of the emitted radiation.

FERMI. The FERMI free-electron laser at the Elettra-Sincrotrone of Trieste is the first user facility to make use of high gain harmonic cascade generation from an external seed laser, instead of SASE, as the main mode of opera-

tion [All+15]. FERMI operates at a repetition rate from 10 to 50 Hz and consists in two separated FEL lines: FEL1, which covers the spectral range from 14 to 61 eV with pulse energies up to 200 µJ, and FEL2, which covers the range from 60 to 300 eV with pulse energies up to 100 µJ. Both lines are based on variable-gap undulators and externally seeded by a tunable VUV source [All+13b], leading to a high level of spatial coherence, polarization control and wavelength stability [All+12; All+14]. A portion of the optical seed laser is transported to the experimental endstations for pump-probe experiments with a high level of synchronization between the two sources [Dan+14]. Additionally, the FEL can provide both pump and probe in a two-pulse scheme operation, achieved by seeding of the electron beam with two laser pulses [Fer+16] or by tuning the undulator sections at two different wavelengths.

SACLA. The Japanese free-electron laser SACLA, located in Kamigori, is in operation since 2011. Unlike most of the other FELs, it makes use of novel variable-gap vacuum undulators, which allow for very short undulator periods λ_u. It also presents an unique electron-beam injector system, which supports high accelerating electron gradients [HL12]. Due to these advantages the length required in order to reach saturation is shorter than in other facilities, leading to a compact apparatus: 750 m length compared to 3 km of LCLS or 1.1 km of PAL-XFEL. Two main hard X-ray FEL lines, BL2 and BL3, are in operation and provide pulses of <10 fs pulse duration at 60 Hz repetition rate. The maximum pulse energy available is 0.5 mJ and the spectral range spans from 4 to 20 keV [Ish+12]. An additional dedicated beamline, called BL1, operates in the soft X-ray range with photon energy approximately from 40 to 150 eV [Owa+18].

EuXFEL. The European XFEL, located at DESY in Hamburg, was developed as a joint effort of 11 different countries. First lasing light was demonstrated in May 2017, at 6 keV with 1 mJ of pulse energy [WD+17]. It now provides femtosecond pulses up to 2 mJ in a spectral range from 0.2 to 25 keV. It is based on a superconducting linear accelerator, instead of conventional accelerator technology, which allow for a high quality electron beam. The accelerator is followed by three variable-gap undulators, called SASE1, SASE2 and SASE3 [Dec+19]. Similarly to FLASH, it operates in a burst mode at 10 Hz but with a maximum intra-burst repetition rate of 4.5 MHz and up to 2700 micro-pulses. Due to these features, unprecedented high peak and average

X-ray brilliance are achieved (see Tab. 2.1).

PAL-XFEL. The PAL-XFEL of the Pohang Accelerator Laboratory, in South Korea, is available for users since 2017 [Ko+17]. It consists of two FEL lines, HX1 and SX1, both based on variable-gap undulators. The hard X-ray line HX1 [Kan+17] recently extended the available photon energy range, demonstrating emission from 2.5 to 20 keV with pulse energies of 0.5-1.5 mJ. The soft Xray FEL line SX1 [Par+18] delivers photons in the range from 0.25 to 1.2 keV with energies up to 1 mJ. Along with the standard SASE method, users at SX1 can also benefit of a harmonic lasing self-seeding mode to improve temporal coherence of the radiation. With this operational mode, an enhancement of 1.7 in the FEL spectral brightness (defined below in equation 2.6) compared to SASE mode has been demonstrated [Nam+18]. Since 2019, both lines operate stably at 60 Hz of repetition rate with pulse duration <50 fs.

SwissFEL. The SwissFEL at the Paul Scherrer Institute in Villigen demonstrated first lasing at 300 eV in 2017 [Mil+17] and reached full optimization in early 2019 with efficient 1 Å generation [Pra+20]. Similarly to SACLA, it is based on short period length vacuum undulators to minimize the required electron beam energy for a specific emitted radiation. It delivers hard X-ray FEL radiation from 1.8 to 12.4 keV with pulse energies up to 500 µJ and pulse durations of approximately 30 fs at a repetition rate of 100 Hz. A second FEL line [Abe+19], called Athos, will operate in parallel to the first one, Aramis, expanding the spectral range to soft X-ray spanning from 0.25 to 2 keV.

In order to compare the performance of different sources, the spectral brightness or brillance $\mathcal{B}$, which is constant along the optical system (if no losses are present), is usually considered. $\mathcal{B}$ is defined as the photon flux $\dot{N}_{ph}$ per bandwidth per unit area and per unit solid angle at the source [Mil+05]:

$$\mathcal{B} = \frac{\dot{N}_{ph}(\omega)}{A \cdot \Theta \cdot \Delta\omega/\omega}, \tag{2.6}$$

where A is the photon source cross section area in [mm^2], Θ the overall angular divergence of the source in [mrad^2] and $\Delta\omega/\omega$ the relative spectral bandwidth which is usually set at 0.1% bandwidth (BW). An overview of the peak brilliance for the different FELs facilities is presented in Tab. 2.1. The range achieved by such high-gain FELs is several orders of magnitude higher than other X-ray sources. In comparison, the typical peak brilliance achieved in synchrotron

facilities or with table-top HHG sources is limited at the range from 10^{15} to 10^{25} [HZS19].

Table 2.1: Overview of typical short-wavelength FELs parameters. The peak brilliance values refer to maximum photon energy. The burst-mode allows for 10 Hz macro-pulses containing up to 800 micro-pulses for FLASH and up to 2700 micro-pulses for EuXFEL.

Facility	Ph. energy [keV]	Pulse duration [fs]	Rep.rate [Hz]	Peak brilliance $[\frac{photons}{\mathrm{s}\cdot\mathrm{mm}^2\mathrm{mrad}^2 0.1\% BW}]$
FLASH	$0.02-0.3$	$30-200$	burst-mode	1×10^{31}
	$0.01-0.3$	$10-200$	burst-mode	1×10^{31}
LCLS	$0.3-11$	$2-500$	120	2×10^{33}
FERMI	$0.01-0.06$	$40-90$	$10-50$	0.6×10^{30}
	$0.06-0.3$	$20-50$	$10-50$	7×10^{30}
SACLA	$4-20$	$2-10$	60	1×10^{33}
EuXFEL	$0.2-25$	$10-100$	burst-mode	5×10^{33}
PAL-XFEL	$2.5-15$	$5-50$	60	1.3×10^{33}
SwissFEL	$1.8-12.4$	$10-70$	100	1×10^{33}

In summary, free-electron lasers nowadays provide strong energetic ultrashort pulses in the soft and hard X-ray spectral range, approximately from 13 eV to 25 keV. The broad wavelength tunability and the unprecedented brightness of the emitted radiation, make FELs remarkable tools for the investigation of dynamics at the temporal and spatial scales of atomic interactions. Such sources have prompted incredible advantages in X-ray science, with applications in many research fields, including X-ray holography [PE20] and coherent diffraction imaging [Mia+15] for the study of not crystalline structure, atomic, molecular and optical (AMO) physics [MS20; Cal+21], photochemistry [URM12; Cha+20], condensed matter [ZDS18; Iri+20] and structural biology [SM12; BKC13]. However, laser-driven sources still represent a necessary laboratory-scale alternative to large-scale facilities. A successful laser-driven approach to generate coherent ultrafast pulses in the XUV to soft X-ray range is high order harmonic generation, which is presented in the following.

2.2 High order harmonic generation sources

For a basic theoretical introduction on the HHG process and its main features see chapter 3. This nonlinear process provides a comb of harmonics of the driving wavelength via strong-field laser interaction with a target [Hey+16a; GR19]. Due to the high spatial and temporal coherence, HHG can be used to expand the spectral range of common available lasers. In particular, strong efforts were made towards the development of sources in the deep XUV from near and mid-infrared drivers [Mak+20; Fu+20]. The main limitation of the process is the relatively low conversion efficiency, which leads typically to a limited photon flux compared to synchrotrons or FELs performance. However, novel progress in high power ultrafast laser technology and new insights on the generation process progressively push forward the development of table-top competitive HHG-based sources.

2.2.1 Driving laser technologies

The first HHG schemes were driven by different laser sources emitting picosecond pulses in different spectral ranges, such as KrF* excimer laser at 248 nm [McP+87], Nd:YAG laser at 1064 nm [Fer+88] or dye lasers at 616 nm [MS92]. Soon after, the invention of chirped pulse amplification (CPA) [SM85] and the development of Ti:sapphire laser systems [Mou86] led to great advances in ultrafast sources. Amplified intense femtosecond pulses in the near-infrared (NIR) became rapidly the dominant driving source for HHG. The generation of few-cycle pulses, supported by the amplification bandwidth of Ti:sapphire lasers, as well as the stabilization of carrier-to-envelope phase (CEP), has pushed forward the usage of HHG in attosecond science [GZB16], leading to the first observations of isolated attosecond pulses [Hen+01].

Nowadays, further improvements in HHG technology are being prompted by new techniques such as high energy Yb-doped lasers and optical parametric chirped pulse amplification (OPCPA) [DJP92]. The development of fibers [Lim+06], Innoslabs [Rus+14] or thin-disk lasers [Sar+19] based on Yb:doped gain materials has overcome some limitations, such as the challenging heat extraction, typical of Ti:sapphire lasers. These advantages pushed the emission of ultrafast pulses with kilowatt average power in the MHz repetition rate range [Bro15]. Amplifiers based on Yb:doped materials can be used directly as drivers for HHG [Fee+17a; Häd+10] or as pump lasers for OPCPA

systems. These systems allow tthe generation of wavelength tunable radiation, overcoming the limitations due to a fixed central wavelength close to 800 nm of conventional Ti:sapphire laser. OPCPA-based lasers are nowadays commonly used as HHG driving sources [Lai+15; Har+17a; Fen+20]. An alternative is to drive the HHG process directly from a laser oscillator without the need of amplification. This approach, favorable for generation at high repetition rates (MHz range), is currently gaining interest, in particular, due to the advances in the development of high-power Yb thin disk oscillators [Sar+19]. Extra-cavity [Ema+15a], as well as intra-cavity [Lab+19; Kan+20a] and enhancement cavity [Jon+05] configurations have been used for HHG.

2.2.2 Modern advances in HHG technology

In parallel, new insights on the HHG process in gas media have contributed to increase the control on the generated radiation parameters. An example is given by the emission of elliptically, or circularly, polarized harmonics achieved by two-colors driving schemes [Fle+14; Zha+20a]. While this possibility was initially not contemplated in the standard semi-classical picture of the HHG process, it is now also extended to attosecond science and, in particular, to isolated attosecond pulses [Hua+18]. The full control of the emitted polarization has applications in several fields, such as ultrafast spectroscopy of chemical dynamics with the study of chiral systems [Dor+19] or magnetic circular dichroism [Fan+15; Azo+19].

Additionally, the development of guided geometries for HHG allows further control of the phase matching conditions during the generation process [Run+98]. By confining the driving laser in a gas-filled waveguide, the typical Gouy phase contribution (see Section 3.2.2) is replaced by a constant factor due to dispersion in the waveguide. Long coherence lengths can be obtained, allowing efficient generation of high photon energies, extending the HHG cutoff up to the keV spectral range [Pop+12]. Guided geometries are also suitable for quasi-phase matching (QPM) conditions [HSB20] by periodical modulation of the waveguide diameter, leading to an enhancement of the generated radiation [Gib+03]. Several methods for QPM have been applied also to not-guided geometries, such as modulation of the nonlinear medium density [Ser+07] or superposition of the driving laser with a weak static field [Kov+12].

Another example of modern development is the realization of XUV frequency combs for precision metrology [Goh+05; Jon+05]. In this case, a train of

pulses of the driving laser is coupled in a high finesse resonator containing the nonlinear medium for intra-cavity HHG. The comb structure of the driving laser is reflected in the generated harmonic spectrum, where each order consists in a comb of narrow continuous wave lines. These frequency combs are provided at MHz repetition rate by a laser oscillator, without need of amplification, and they can be used in high precision measurements [Pup+21].

In conclusion, the development of HHG-based sources and the improvements in ultrafast laser science are tightly interconnected. While Ti:sapphire technology is a well establish and fundamental driving source for HHG, modern applications based on Yb:doped gain materials and optical parametric amplification are opening new regimes for harmonic sources. In particular, strong effort is being made in the direction of high photon flux XUV emission and efficient generation at repetition rates larger than a few kHz [Red+15]. A brief overview of such sources is given in the following.

2.2.3 State-of-art harmonic sources at high repetition rates.

Many investigations in atomic or molecular dynamics strongly benefit from high repetition rates sources ($\gg 1\,\mathrm{kHz}$). For instance, coincidence spectroscopy [Dör+00; Con01] favors high event rates to improve statistics; XUV frequency-comb spectroscopy [PH19] requires high repetition rates for narrow line spacing and high resolution measurements; time-resolved photoelectron microscopy [Sto+07], as well as 3D coherent diffraction imaging [BMM20], make use of high repetition rates to improve the signal-to-noise ratio. The development of HHG-based sources at repetition rates larger than a few kHz is advancing remarkably due to improvements in the generation techniques and the availability of new powerful driving lasers, which provide the required intensity range ($\sim 10^{14}\,\mathrm{W/cm^2}$) in a large range of repetition rates. A selection of state-of-art HHG sources in gas media, operating in the kHz and MHz range, is presented in Fig. 2.2. The emitted photon flux is reported in Fig. 2.2a, while the pulse energy is reported in Fig. 2.2b. For clarity, all the references in the figures are indicated by numbers, instead of the usual convention, and the same codification of these specific references is used in the following.

Standard single-pass configurations (indicated with small triangles in Fig. 2.2), such as jets [Mak+20], cells [Ye+20] or gas-filled waveguides [Pop+12],

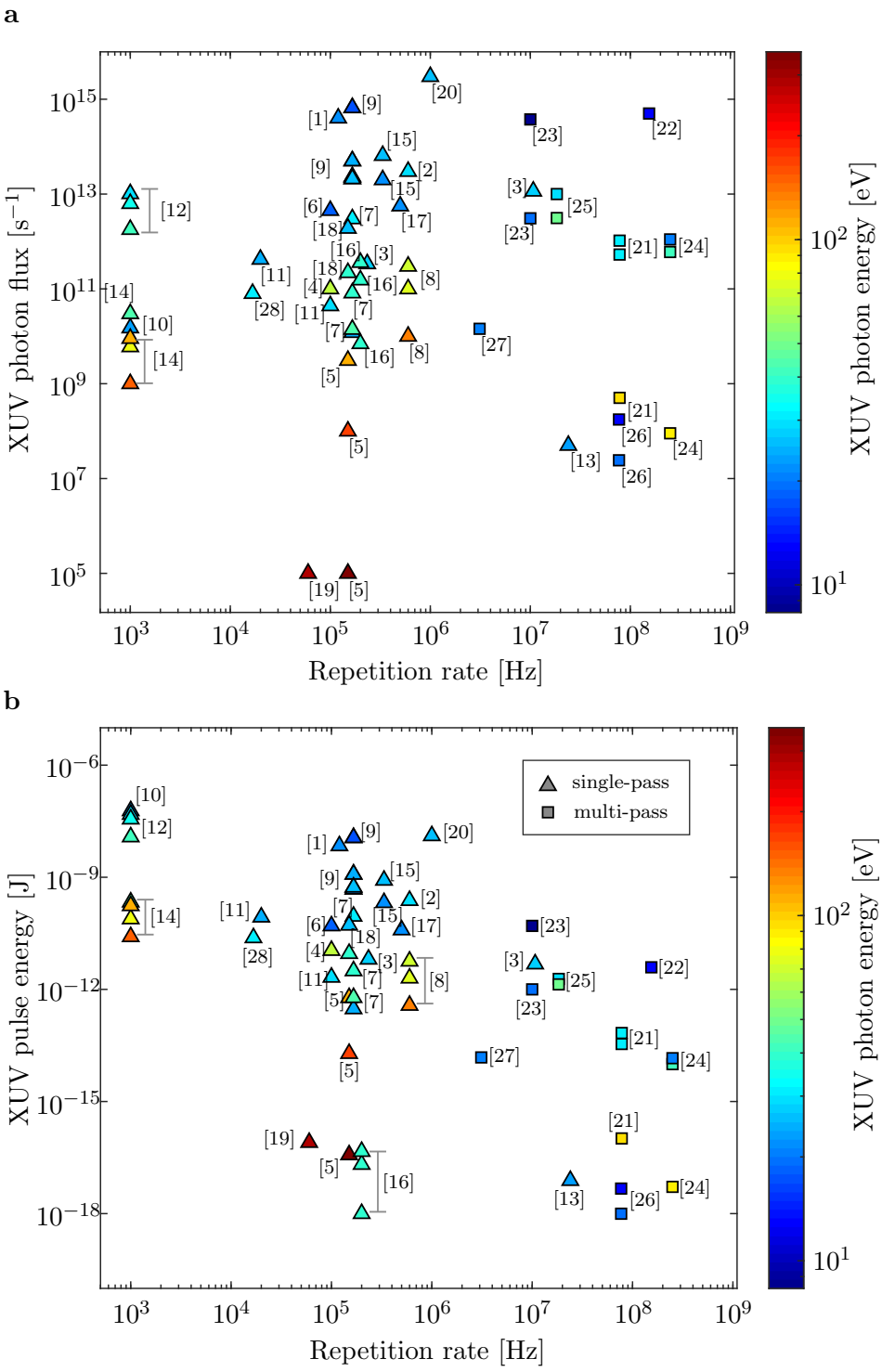

Figure 2.2: Overview of selected papers of HHG in gas media displayed by photon flux (a) and pulse energy (b) emitted in the XUV range at different repetition rates. Single-pass configurations are indicated with triangle markers, while rectangular markers indicate multi-pass configurations. The photon energy emitted is color-coded. All references used [1]- [28] are reported in a separate section of the bibliography for better visualization.

were usually used in loose focusing geometries driven by Ti:sapphire based amplifiers, which provide multi-mJ femtosecond laser pulses in the few kHz range. Recently, the development of new concepts for phase matched emission in tight focused geometries [Rot+14c; Hey+16a], where the Gouy phase shift strongly influences the process (see Sections 3.2.2 and 3.3), allowed single-pass configurations to be efficiently employed in multi-kHz systems. In the range of tens or hundreds of kHz, table-top OPCPAs and Yb:doped based lasers provide pulse energies up to hundreds of µJ, which can be used to drive the generation process in high photon flux XUV sources [8; 9]. By using a 166 kHz Yb-fiber chirped pulse amplification (FCPA) system, Comby *et al.* [9] reported the generation of 6.6×10^{14} photons per second at 18 eV, driven by a 343 nm driver (third harmonic of the fundamental wavelength). Recently, a record photon flux exceeding 10^{15} photons per second at 26.5 eV and 1 MHz, was presented by Klas *et al.* [20]. For this novel result, a frequency doubled Yb-fiber laser post compressed to <20 fs [Kla+20b] was used, reinforcing the importance of Yb-fiber lasers as HHG drivers at this repetition rate range. A promising approach to push the application of single-pass HHG further into the MHz range, is the use of high-power oscillators [13]. Yb:doped gain materials are again the most favorable choice: when used in thin disk oscillators, they can provide pulse energies of tens of µJ in the multi-MHz range [Sar+15; Sar+19]. A typical disadvantage of such drivers is the long pulse duration at around hundreds of femtoseconds. However, this disadvantage can be compensated by making use of external pulse compression stages [13].

At higher repetition rates, up to hundreds of MHz, the HHG process is dominated by multi-pass configurations (indicated with small rectangles in Fig. 2.2). Two main approaches are used: femtosecond enhancement cavities (fsEC) [Jon+05] and intra-cavity HHG in laser oscillators [Lab+19]. In a fsEC, the coherent addition of successive laser pulses leads to pulse amplification with enhancement factors from 100 to 10 000. By using a mode-locked oscillator as seed laser of the passive cavity, kW intracavity average powers in the MHz range are achieved [JY02]. The generation of high order harmonics in a fsEC was demonstrated in 2005 [Jon+05] by placing the gas target inside the passive cavity, and it has been further optimized since then [Pup+21]. However, this configuration suffers from difficult out-coupling of the generated XUV radiation, which can severely reduce the cavity enhancement. While several solutions have been tested to overcome the problem, noncollinear geometries recently stood out as a very promising approach. A record high out-coupling efficiency

of 60% was reported by Zhang *et al.* [22] in a crossed-beam cavity, which allows two laser pulses to be resonantly enhanced simultaneously. With this unique geometry, a photon flux of 5×10^{14} γ/s at 12.8 eV has been reported at 154 MHz. New important improvements have also been demonstrated in case of intra-cavity HHG inside a mode-locked oscillator. Kanda *et al.* [27] reported the generation of two XUV sources at 3 MHz in a single Yb:YAG thin disk laser by applying a two-separate-foci geometry. Such configurations could provide very compact XUV pump-probe schemes for time-resolved measurements.

Despite the great improvements, the HHG process is still less efficient at high repetition rate compared to systems operating at $\leq$ 1 kHz. Therefore, while the generated photon flux benefits from the high repetition rats, the XUV pulse energy decreases, as shown in Fig. 2.2b. In 1999, Constant *et al.* [10] already demonstrated the generation of ∼60 nJ at 50 eV from a 1 kHz Ti:sapphire laser system. While the nJ level has been reached in the multi-kHz range [9; 20], multi-pass sources are limited to tens of pJ [23]. The gap increases even more by considering table-top systems at 10 Hz. Early results employing loose focusing geometries shown a XUV generation in the µJ range [Her+02; TNM02; Tak+02]. More recently, Makos *et al.* [Mak+20] reported a record generation of 150 µJ XUV pulses in a double gas jets configuration by making use of a 9 m focal length. With this source, attosecond pulse trains in the order of 650 as have been measured. This cutting-edge result paves the way for future exceptional achievements in high energetic XUV sources. At the Extreme Light Infrastructure – Attosecond Light Pulse Source (ELI-ALPS) facility, two attosecond beamlines at 1 kHz, based on a similar long loose focusing geometry, are currently under construction [Küh+17]. Such high power HHG beamlines are expected to revolutionize the state-of-art of attosecond sources, reaching unique conditions for laser-driven XUV-pump-XUV-probe time-resolved studies in the attosecond regime.

2.3 Time-resolved studies

Free-electron lasers and table-top high order harmonic sources can provide unprecedented resolution in the spatial domain, down to sub-nanometer wavelengths, as well as in the temporal domain, reaching the attosecond range. These characteristic features make them optimal candidates for unraveling ultrafast dynamic processes in matter. Time-resolved studies are typically

performed in pump-probe schemes, where a first pulse initiates the dynamics in the target and a temporal delayed second pulse probes the state of the target at a defined instance of time. Such technique allows to study, not only the initial and final state of the target, but also transient states during the dynamics with a time resolution which is limited by the time duration of the optical pulses used. With the development of ultrafast laser technology, the monitoring of molecular motion and chemical reactions became possible opening to a new research field, called femtochemistry which concerns the study of chemical process at femtosecond time scales [Zew94]. In 1999, Ahmed Zewail received the Noble Prize in chemistry for his studies on fragmentation dynamics during a chemical reaction using femtosecond spectroscopy [Zew00]. The observation of fragmentation dynamics is achieved with pulse duration typically of hundreds of femtosecond [PHZ94], while vibrational motion in molecules or dissociation reaction require pulses from tens to a few femtoseconds [Zew00]. Even shorter pulse duration are needed for the study of the electronic motion in the attosecond time regime [Cal+16]. XUV and X-ray sources are often used in time-resolved studies for the short pulse durations achievable, down to the attosecond regime, which is not supported by the optical cycle of infrared radiation (typically of a few femtoseconds). But short wavelengths also allow for high spatial resolution and for efficient excitation of high energetic molecular or electronic states [URM12]. In particular X-ray photons access element-specific excitation reaching to the inner-shell energetic levels [Kas+20].

Different type of pump-probe schemes can be employed. The high photon flux delivered by FELs is well suitable for the implementation of split-and-delay units in which one part of the FEL beam is delayed with respect to the other part [RR15]. These units allows to supply both pump and probe pulses from a single high photon flux source and to control their relative delay. This approach results more challenging for HHG-based sources, in which the emitted photon flux is limited by the relative low conversion efficiency of the nonlinear process. However, as shown in Fig. 2.2a, novel XUV table-top setups have demonstrated flux performance comparable to short-wavelength FELs in the vacuum ultraviolet (VUV) spectral range, reaching up to 10^{14}-10^{15} photons per second and opening new perspectives for laser-driven pump-probe experiments [Hil+20b; Mak+20]. Pump and probe pulses can also be provided by separated sources, allowing for two-color schemes where the photon energies of the two pulses are independently chosen accordingly to the dynamics under investigation. Currently, short-wavelength FELs are often used in combination with near-

infrared femtoseconds lasers, often employing complex synchronization and jitter correction systems [Sch+15; Sav+17; Let+20]. Frequency conversion allows to expand the spectral range covered by ultrafast lasers from the deep ultraviolet to the THz range [Red+11; Lan+19; Sch+19a]. Similarly, HHG-based sources in the VUV or XUV spectral range are commonly used in pump-probe schemes in combination with femtosecond optical lasers in a large number of applications [Red+15]. In this case, typically, a fraction of the driving laser is used in combination of the HHG-based source, leading to a much easier synchronization between pump and probe pulses due to the high temporal coherence of the generation process.

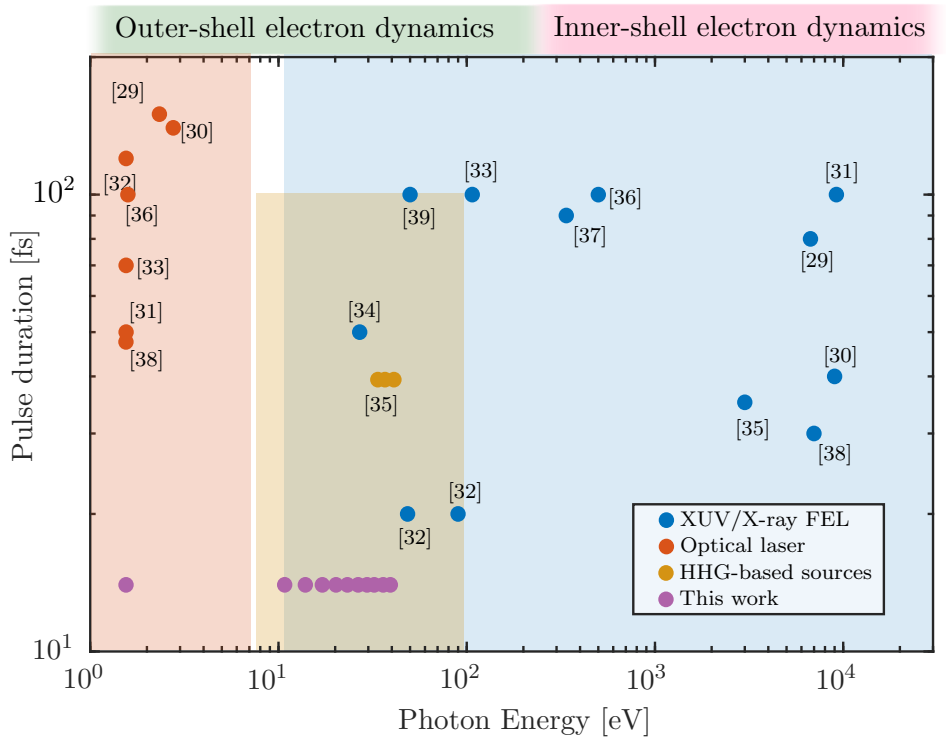

Figure 2.3: Typical pulse duration and photon energy range available of XUV/X-ray FEL (in blue), femtosecond optical laser (in red) including frequency conversion, and HHG-based souces (in yellow). A selection of pump-probe experiments performed at FEL facilities is indicated by colored points depending on the sources used. The results presented in this thesis are shown in violet. All references used [29]- [39] are reported in a separate section of the bibliography for clarity. Figure adapted by [App+20].

Fig. 2.3 shows a short selection of pump-probe experiments performed at short-wavelength FEL facilities and their typical pulse duration, from tens to hundreds of femtoseconds, and photon energy range, from a few eV to tens

of kV. However, the pump-probe parameter space can be further extended by combining a FEL beam with a HHG-based source, opening a new regime for two-color pump-probe experiments in the VUV/XUV spectral range [35]. Such configuration benefits from the complementary properties of both sources. The high pulse energy and narrowband tunability available by free-electron lasers can be combined with the broad spectral bandwidth of the HHG source, particular suitable for the investigation of multiple spectral resonances within a single acquisition. Moreover, the independent tuning of the pump and probe central wavelength in the VUV/XUV spectral range allows to access directly many excitation levels of interest in atomic and molecular targets without relying on the absorption of many less energetic infrared or visible photons.

However, several different aspects must be considered for a successful integration of a HHG-based source in a FEL beamline, including the optimum generation geometry and a reliable high-vacuum system. In order to described how these challenges were addressed during the design of the new VUV beamline at FLASH, a short theoretical introduction on the HHG process is first presented in the following.

Chapter 3

HHG theory

The first observations of the HHG process date back to 1987, when two different research groups reported the detection of a plateau of odd harmonic orders with a sharp cutoff originated by a picosecond laser focused in a gas medium [McP+87; Fer+88]. Due to its unique features, HHG has quickly become an established process worldwide used to provide coherent radiation, especially in the XUV and soft X-ray domain. This chapter provides a short introduction on the basic principles of HHG in gases with particular interest to efficient generation at limited driving pulse energy, which is a common drawback for sources at repetition rates higher than a few kHz.

3.1 Nonlinear properties of light-matter interaction

The propagation of light in a dielectric material, in contrast to the propagation in vacuum, leads to an interaction between the optical electric field $E(\mathbf{r}, t)$ and the electrons in the atoms which results in a macroscopic induced polarization $P(\mathbf{r}, t)$. Depending on the intensity of the optical field, the light-matter interaction can have linear or nonlinear properties. For weak optical fields compared to the atomic potential in the material, the polarization's dependency on $E(\mathbf{r}, t)$ is well described by a linear proportionality: $P(\mathbf{r}, t) = \epsilon_o \chi E(\mathbf{r}, t)$. The proportional coefficients are the vacuum permittivity ϵ_0 and the electric

susceptibility of the material χ, which are independent from the incident field. For stronger optical fields, $E(\mathbf{r}, t)$ is no longer negligible compared to the local atomic fields and, therefore, nonlinear terms must be taken in account. In terms of perturbation theory, the polarization can be expanded into a Taylor series:

$$P(\mathbf{r}, t) = \epsilon_0 \chi^{(1)} E(\mathbf{r}, t) + \epsilon_0 \chi^{(2)} E^2(\mathbf{r}, t) + \epsilon_0 \chi^{(3)} E^3(\mathbf{r}, t) + ..., \qquad (3.1)$$

where the first term $\epsilon_0 \chi^{(1)} E(\mathbf{r}, t)$ denotes the linear polarization, and the following terms indicate additional nonlinear components. Perturbation theory of light-matter interaction explains many nonlinear effects in which the temporal, spectral and spatial properties of the laser field can change during propagation in the medium. Examples of second order nonlinear effects, connected to the first nonlinear term $\chi^{(2)}$, are: second harmonic generation, sum or difference frequency generation and optical parametric amplification in crystals [LNM20]. Third order effects, dominant in isotropic media where $\chi^{(2)} = 0$, include for instance the Kerr effect. This effect leads to an intensity-dependent refractive index, which is directly related to self-focusing, basic principle of Kerr lens mode-locking of laser oscillators [KTK19], and self-phase modulation, that can be used for pulse compression [Gre+20].

Strong field ionization. When the optical field reaches the order of magnitude of the atomic potential, the perturbation approach fails in describing the light-matter interaction. In this case, the optical intensity is sufficiently intense to ionize the material and the problem has to be treated quantum-mechanically. Such high intensities are usually reached with intense short laser pulses, which allow for different ionization mechanisms of the material. At lower intensity, *multiphoton ionization* (MPI) dominates the process with the simultaneous absorption of multiple photons by a single electron. *Above threshold ionization* (ATI) occurs when the number of photons absorbed brings the electron to an energetic state above the ionization threshold providing kinetic energy to the ionized electron. For higher intensity, typically in the $10^{14}\,\mathrm{W/cm^2}$ range, the atomic potential can be so distorted by the optical field to allow *tunnel ionization* (TI). In this mechanism the electron leaves the bonding potential by tunnel effect through the potential barrier. For even higher intensities, the atomic potential is so strongly distorted that the electron is no longer bound. This is the case of *over the barrier ionization* (OTBI). A detailed description of ionization processes in strong fields and their dependencies on the optical

parameters can be found in [Pop04]. Strong field ionization is the basic mechanism for nonlinear processes such as high order harmonic generation [Hey+16a], Brunel radiation [Bru90], filamentation [CM07] and it is the basis of the young research field of strong-field nano-optics [Dom+20].

3.2 Introduction to high order harmonic generation

Due to their high spatial and temporal coherence [Sal+99; Ben+14], HHG-based sources provide laser-like pulses in spectral regions not accessible to conventional lasers, such as in the XUV and soft X-ray spectral range [Mak+20; Fu+20]. As already mentioned, these sources are used nowadays in several research fields including atomic and molecular physics [DLM12; Vil+17], condensed phase systems [Cav+07], and time-resolved studies of more complex systems [Red+15; Cal+14]. The generation of attosecond pulses via HHG, theoretically predicted in [FT92; HMH93] and experimentally demonstrated in 2001 [Pau+01; Hen+01], is an essential tool for attosecond science [Li+20; Cal+16; PMV19]. While several different targets have been tested, such as plasma surfaces [TG09], solid targets [GR19] and liquid targets [Kur+13; Luu+18; ZB20], the process of HHG in a gas medium is the most well-known and established technology. Therefore, in the following, the discussion will be restricted to gas-based harmonic generation.

The radiation emitted via HHG results typically from two contributions: the response of a single atom to the intense laser pulse, *single atom response*, and the macroscopic influence of the emitted radiation propagation through the medium including the interference of light generated at different spatial positions, *macroscopic effects*. Both contributions are shortly introduced in the the following.

3.2.1 Single-atom response

The basic physical mechanism underlying the single atom response involved in HHG can be explained with a simple semi-classical approach, called the "three-step model" and proposed in 1994 by Corkum [Cor93]. For a complete description of HHG, a fully quantum mechanical model is required [Lew+94], but the semi-classical approach is sufficient to understand the basic HHG

properties. As suggested by the name, the three-step model describes the single atom response to the strong laser field in three different parts, sketched in Fig. 3.1 and shortly described below.

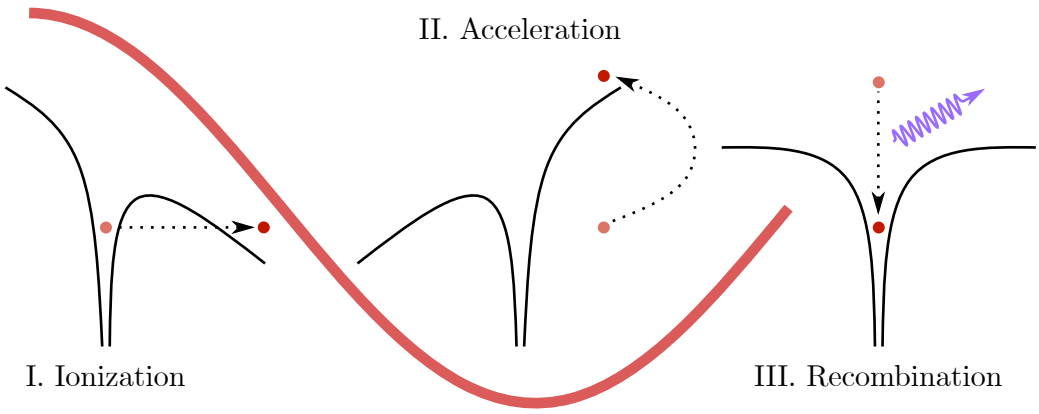

Figure 3.1: Sketch of the three-step model. The oscillating optical field, in red, bends the atomic potential leading to tunnel ionization of an electron (Step I), which is accelerated in the continuum (Step II). As the field changes sign, the electron returns towards the parent ion and it may recombine (Step III), releasing a photon.

Step I: tunnel ionization. In the first step the electron leaves the atom by tunnel ionization with zero kinetic energy. As already mentioned, tunnel ionization is typically the dominant ionization mechanism at laser intensity around $10^{14}\,\mathrm{W/cm^2}$, which sets a necessary condition for efficient HHG. In this process, the oscillating laser field distorts the atomic potential allowing ionization twice per optical cycle. The periodicity of the process in time is then $T/2$, where T is the cycle period of the optical field.

Step II: field acceleration. After ionization the electron is treated as a classical particle which is accelerated by the oscillating field $E(t) = E_0 sin(\omega t)$. The electron's trajectory is then determined classically and depends on the ionization time t_i and on the field properties. Assuming that the electron is ionized with zero velocity at the initial position $x(0) = 0$, its trajectory is given by:

$$x(t) = \frac{eE_0}{m\omega^2}\left[sin(\omega t) - sin(\omega t_i) - \omega(t - t_i)cos(\omega t_i)\right], \tag{3.2}$$

where e is the electron charge and m its mass. During its excursion in the continuum, the electron gains kinetic energy which will then be released as an emitted photon upon recombination with the parent ion (step III).

Step III: recombination. As the field changes sign, the electron is accelerated back towards the parent ion where it recombines with a certain probability. Depending on the ionization time t_i, three main cases can be distinguished: "no recombination", "long" trajectories and "short" trajectories. A sketch of these three cases is shown in Fig. 3.2a. For $t_i < T/4$, the electrons are ionized before the field maximum and do not recombine with the parent ion. However, for $T/4 < t_i < T/2$ they have a certain probability to recombine and contribute to the HHG process. If $T/4 < t_i < T/3$ the trajectory is called "long" due to the longer recombination time t_r, while for $T/3 < t_i < T/2$ is called "short" due to the shorter recombination time.

The kinetic energy of the electron which returns to the parent ion ϵ_r can be expressed in terms of the ponderomotive energy U_p as:

$$\epsilon_r = 2U_p \left[cos(\omega t_r) - cos(\omega t_i)\right]^2, \tag{3.3}$$

where the recombination time t_r is the time between ionization and recombination. The ponderomotive energy is define as the cycle-averaged kinetic energy of a free electron in the optical field [Con98] and can be expressed as:

$$U_p = \frac{e^2 E_0^2}{4m\omega^2} = \frac{e^2 \lambda^2 I}{8\pi^2 m \epsilon_0 c^3}. \tag{3.4}$$

The dependency of ϵ_r from t_i (see equation 3.3) is shown in Fig. 3.2b. The return energy first increases with the ionization time and then decreases for always shorter trajectories. The maximum value is equal to about $3.17U_p$. Consequently, the photon energy emitted via HHG follows the relation:

$$E_{ph} \leq I_p + 3.17 \cdot U_p, \tag{3.5}$$

where I_p is the ionization potential of the medium. Equation 3.5 sets a limit for the maximum value of the photon energy which can be emitted, known as "cutoff energy" E_{cutoff}. Its value increases linearly with the laser intensity and quadratically with the driving wavelength due to its dependency on U_p. For instance, the harmonic spectrum generated in argon (I_p =15.76 eV) will extend more into higher photon energy compared to xenon (I_p =12.13 eV) or for driving wavelength in the mid-infrared compared to visible wavelengths.

The three-step model explains the main features of a typical HHG spectrum, sketched in Fig. 3.3. The emitted spectrum consists on a plateau of consecutive

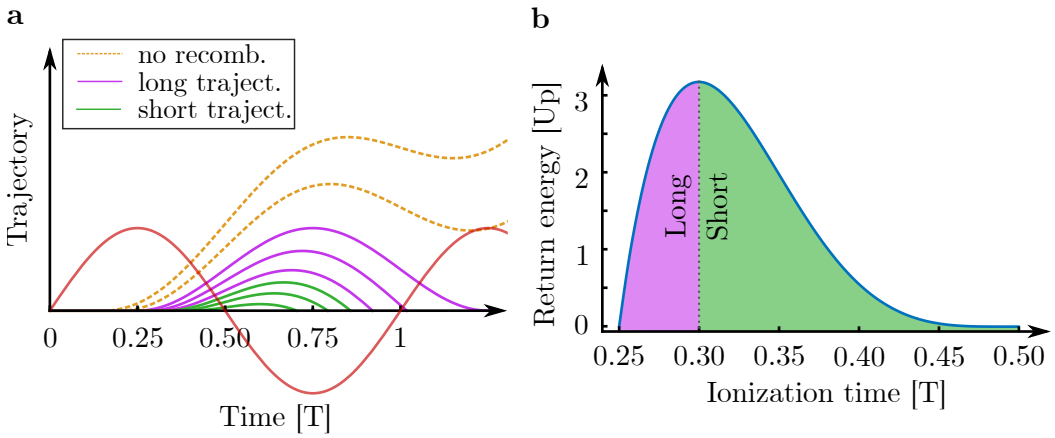

Figure 3.2: Long and short trajectories contributions in HHG. a) Depending on the ionization time t_i, three main types of trajectories are predicted by the semi-classical approach: trajectories which do not recombine ($t_i < T/4$, in yellow), long trajectories ($T/4 < t_i < T/3$, in violet) and short ones ($T/3 < t_i < T/2$, in green). The optical field is shown for comparison (in red). b) The electron return energy shows a maximum value of $3.17U_p$, which sets an upper limit for the emitted photon energy.

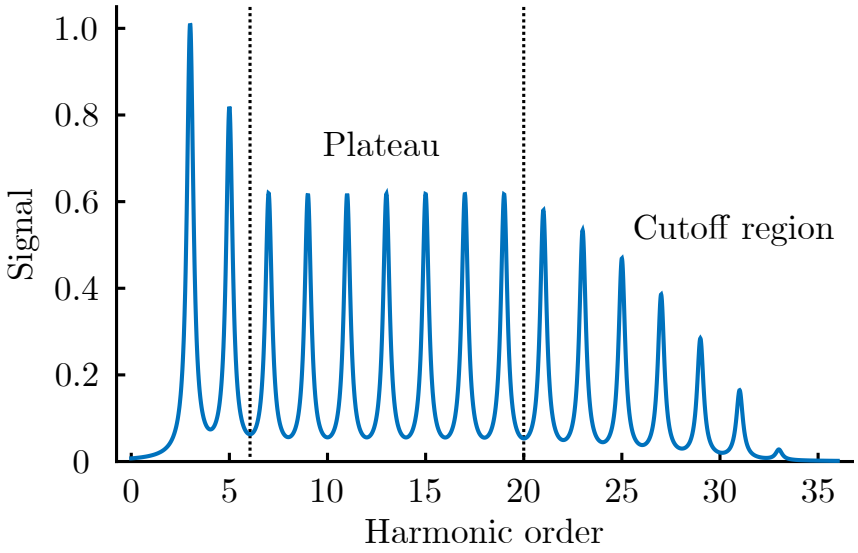

Figure 3.3: Representation of a typical harmonic spectrum. Odd harmonic orders of the driving wavelength are emitted with similar amplitude in the plateau. Follows the cutoff region in which the harmonics intensity quickly drops close to the maximum photon energy E_{cutoff}.

harmonic orders with similar amplitude. These orders correspond to electrons ionized shortly after the maximum of the laser field which recombine with a kinetic energy below the maximum of $3.17U_p$. The similar ionization probability leads to a similar efficiency inside the plateau region. The harmonic intensity decreases sharply in the cutoff region, where the emitted photon energies approach E_{cutoff}. Only odd harmonic orders of the driving wavelength are emitted due to the process periodicity of half cycle in time, which causes a periodicity in frequency of 2ω. The emission of even harmonic orders requires to break the symmetry by applying, for instance, an asymmetric field into the generation process [Gan+20; Say+21].

3.2.2 Macroscopic effects

Besides the single-atom response, the radiation generated via HHG depends on macroscopic effects, such as the propagation in the generating medium and phase matching conditions. A detailed description of macroscopic effects in HHG can be found, for instance, in [Con+99b; GTS08]. In the following, only the basic concepts of phase matched emission are presented in order to highlight their influence on a globally maximized generation signal.

The harmonic signal is not only generated by a single atom, but by several emitters along the medium. Similarly to the case of low order harmonic generation, an efficient frequency conversion can be expected when the process is phase matched. In this case, the generated radiation from all emitters achieves constructive interference in the far field and the overall harmonic yield is maximized. The basic principles of phase mismatch present in harmonic generation can be described using a one dimensional model [Con+99b] by neglecting the off-axis and transverse effects. It should be noted that these effects can be very important, especially in case of non-collinear geometries or strong spatio-temporal couplings [Ell+17; Hög+19]. The signal S_q generated in a harmonic order q is the coherent sum over all single atom contributions in the gas medium of length L. Denoted as d_q the dipole amplitude for harmonic order q, the signal S_q along the optical axis is proportional to [Hey+16a]:

$$S_q \propto \left| \int_0^L d_q \exp\left[i \left(\Delta k + i\kappa_q \right) (L - z) \right] dz \right|^2 , \tag{3.6}$$

where κ_q is the absorption coefficient and $\Delta k = k_q - qk_0$ is the mismatch between the wavevector k_q of the generated harmonic field and the wavector of the

induced polarization at frequency $q\omega$. The term Δk can also be expressed as a phase mismatch $\Delta\phi$ following the relation $\Delta k = \partial\Delta\phi/\partial z$ along the propagation axis z.

Phase matching contributions. For HHG in a gas medium, the wavevector mismatch Δk consists in four main terms [Kaz+03; GTS08]:

$$\Delta k = \Delta k_g + \Delta k_d + \Delta k_n + \Delta k_p, \tag{3.7}$$

where Δk_g indicates the Gouy phase contribution, Δk_d the dipole phase, Δk_n and Δk_p the dispersion in neutral atoms and in plasma, respectively. Each contribution is shortly described in the following.

- Δk_g. The focusing of a Gaussian laser pulse leads to a spatial-dependent phase shift, the Gouy phase shift [FW01], which is due to the curvature of the focused laser wavefronts in respect to an ideal plane wave. Neglecting the small Gouy phase of the harmonic beam, the total geometric wavevector mismatch between the fundamental and the generated harmonic beam can be expressed as:

$$\Delta k_g(r,z) = -q\frac{\partial}{\partial z}\left[\arctan\left(\frac{z}{z_R}\right) - \frac{\pi r^2}{\lambda R(z)}\right], \tag{3.8}$$

  where z_R is the Rayleigh length of the focused fundamental field. The first term denotes the phase offset contribution along the optical axis z, while the second term accounts for off-axis components along the curved wave fronts $R(z) = z\left[1 + (z_R/z)^2\right]$. In case of a guided geometry, Δk_g has to be replaced by a wavevector mismatch arising from propagation in the waveguide [Pop+09a], which is constant over the generation medium in contrast to the wavevector mismatch introduced by the Gouy phase.

- Δk_d. As predicted from the three-step model, two main different trajectories (long and short) of the electron excursion may contribute to the same harmonic order dipole amplitude d_q in the plateau region. In a fully quantum mechanical description of HHG, even further paths of minor influence are possible. During its excursion in the continuum, the electron accumulates an additional phase, called dipole or atomic phase. This phase depends on its trajectory and, therefore, on its recombination time t_r and ponderomotive energy U_p [Sal+98; LSL95]. By considering the dependency of U_p from the laser intensity I (see eq. 3.4), the produced

wavevector mismatch can be approximated as:

$$\Delta k_d(r,z,t) = -\alpha(q)\frac{\partial I(r,z,t)}{\partial z}. \tag{3.9}$$

The coefficient $\alpha(q) > 0$ depends in the harmonic order q and it is smaller for short trajectories than for long ones [GS02]. The dependency of the dipole phase from U_p leads to significant changes of $\Delta k_d(r,z,t)$ following the spatio-temporal structure of $I(r,z,t)$.

- Δk_n. Dispersion due to neutral atoms in the nonlinear medium causes a phase shift between the driving laser field and the generated harmonic orders, similarly to other frequency conversion processes. The resulting wavevector mismatch Δk_n can be expressed as:

$$\Delta k_n(q,\omega) = q\frac{\omega}{c}(n_f - n_q), \tag{3.10}$$

where n_f and n_q are the refractive indexes in the neutral gas for the fundamental and harmonic field, respectively. Following [Hey+16a], the refractive index for the fundamental can be approximated as $n_f \approx 1 + N_0\alpha_{dip}/\epsilon_0$, where N_0 is the neutral atoms density and α_{dip} denotes the static polarizability of the gas [Sch15]. Corresponding values of n_q can be found in [HGD93].

- Δk_p. Similarly to the case of neutral atoms, the dispersion due to free electrons leads to a wavevector mismatch Δk_p which depends on the plasma properties. The refractive index induced by free electrons can be written as:

$$n_q^e = \sqrt{1 - \frac{\omega_p^2}{q^2\omega^2}} \approx 1 - \frac{\omega_p^2}{2q^2\omega^2}, \tag{3.11}$$

where $\omega_p = \sqrt{e^2 N_e/m\epsilon_0}$, is the plasma frequency and N_e the plasma density. The mismatch Δk_p is then given by:

$$\Delta k_p(q,\omega) = q\frac{\omega}{c}(n_f^e - n_q^e) \approx \frac{\omega_p^2}{2qc\omega}\left(1 - q^2\right). \tag{3.12}$$

In order to reach phase matched emission, the four terms must compensate each other and sum up to zero. The Gouy phase contribution Δk_g and the plasma dispersion Δk_p are negative terms, while the dispersion due to neutral atoms leads to a positive term Δk_n. For positions along the optical axis where the nonlinear medium is placed behind the focus ($z > 0$), the dipole mismatch

Δk_d contributes as an additional positive term [LSL95]. Typically, this leads to better on-axis phase matching conditions for the short trajectories [Sal+98], while for the long ones the large value of α leads to strongly time-dependent phase matching conditions. On the contrary, for conditions where the nonlinear medium is placed before the focus ($z < 0$), Δk_d is negative and the phase matching is dominated by off-axis contributions of the long trajectories [GS02].

Optimized emission. In order to achieve a fully phase matched emission, the total wave vector mismatch Δk is required to be zero for all spatial positions at every time t. But due to the rather complex dependency of each Δk_i contribution on several generation parameters, such as focusing geometry or gas pressure, Δk is subject to large spatial and temporal variations. Therefore, usually phase matched HHG can be achieved only during a certain time interval within a part of the generation volume. As a consequence, phase matched generation does not necessarily correspond to an overall maximized emitted photon flux.

In the literature, the wavevector mismatch is often replaced with the coherence length L_{coh} defined for each harmonic order q as:

$$L_{\text{coh}} = \frac{\pi}{|\Delta k|}. \tag{3.13}$$

Due to the phase mismatch, the harmonic yield increases and decays periodically, so L_{coh} indicates the medium length along the propagation direction in which the harmonic emission builds-up. Similarly, the coefficient κ_q is often replaced with the absorption length L_{abs}:

$$L_{\text{abs}} = \frac{1}{2\kappa_q} \tag{3.14}$$

With these definitions, equation 3.6 can be re-written as [Con+99b]:

$$S_q \propto |d_q|^2 \frac{4L_{\text{abs}}^2}{1 + 4\pi^2 \left(\frac{L_{\text{abs}}}{L_{\text{coh}}}\right)^2} \left[1 + \exp\left(-\frac{L}{L_{\text{abs}}}\right) - 2\cos\left(\frac{\pi L}{L_{\text{coh}}}\right)\exp\left(-\frac{L}{2L_{\text{abs}}}\right)\right] \tag{3.15}$$

for d_q and L_{abs} constant along the medium. The evolution of the harmonic signal as a function of the medium length, shown in Fig. 3.4, is then always limited by absorption. Even for an infinite L_{coh}, the emission saturates due to reabsorption (absorption limited emission). In order to ensure that the harmonic emission is more than half of the maximum response, the conditions:

$$L > 3L_{\text{abs}} \quad \text{and} \quad L_{\text{coh}} > 5L_{\text{abs}} \tag{3.16}$$

should be fulfilled for a nonlinear medium of length L. Relations 3.16 give an indication for the optimization of the harmonics signal, that is often achieved by tuning several generation parameters, particularly pressure, intensity, and medium position [Rud+13].

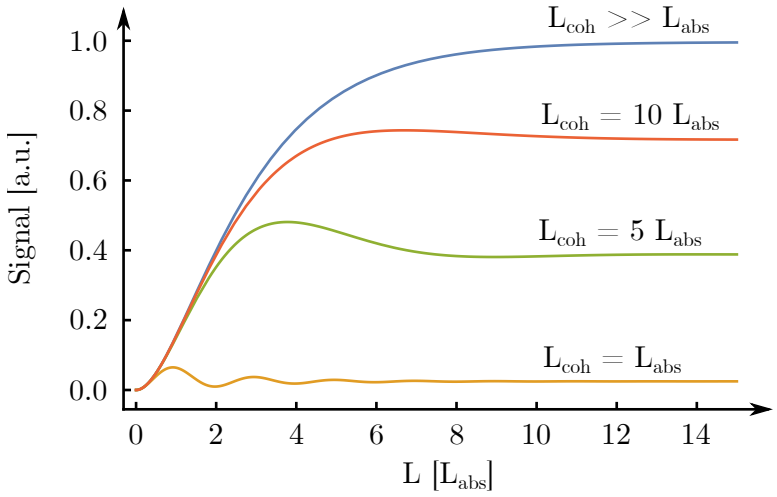

Figure 3.4: Evolution of the harmonic signal as a function of the medium length L in units of L_{abs} for different values of L_{coh}. For more details refer to [Con+99b].

3.3 Energy scaling principle for HHG

The scaling of the HHG process with respect to the generation parameters, such as driving wavelength [Tat+07; Shi+09] and laser intensity [KSK92], have contributed to the improvement of state-of-art harmonics sources performance [Pop+09b; Che+10]. As the interest towards high repetition rates ($\gg$ 1 kHz) sources increased, the dependency of the process on driving pulse energy or average power, which are limited in case of high repetition rates, have become more and more relevant. Initially, a b^3 scaling law of the conversion efficiency was proposed, where $b = 2z_0$ is the confocal parameter of the driving laser beam [Bal+92]. More recently, different efficiency scaling relations have been proposed [MNS08; Tak+02]. A more general concept was introduced in 2016 on invariant scaling of nonlinear phenomena in gases [Hey+16b]. In the specific case of HHG, this general concept supports earlier theoretical and experimental studies on phase matching under tight focusing geometries [Hey+12; Rot+14c]. In the following, only a brief overview of the model is presented in order to introduce the energy scaling relations for HHG. A detailed description of the concept can be found in [Hey+16b; Hey+16a].

Typically, nonlinear propagation of linearly polarized light in gases is described in the frequency domain with a paraxial wave equation, known as forward-Maxwell equation:

$$\left(\frac{\partial}{\partial z} - \frac{i}{2k(\omega,\rho)}\Delta_\perp - ik(\omega,\rho)\right)\hat{E} = \frac{i\omega^2}{2k(\omega,\rho)c^2\epsilon_0}\hat{P}_{NL}, \tag{3.17}$$

where $\hat{E}$ and $\hat{P}_{NL}$ are the frequency representations of the electric field and the induced nonlinear polarization in the medium, respectively. Consistently, $k(\omega,\rho)$ represents the wave number with angular frequency ω at the gas density ρ, c the speed of light in vacuum and ϵ_0 the vacuum permittivity. The first term in equation 3.17 describes the wave propagation along the optical axis, while diffraction and dispersion are represented by the second and the third term, respectively. $\hat{P}_{NL}$ can be a sum of different contributions and can describe several nonlinear processes in gases, such as HHG or filamentation.

By changing the reference system from the laboratory frame to a reference frame moving at the vacuum speed of light c, the electric field and the nonlinear induced polarization are replaced with $\hat{\mathcal{E}} \equiv \hat{E}\exp[-i\omega z/c]$ and $\hat{\mathcal{P}}_{NL} \equiv \hat{P}_{NL}\exp[-i\omega z/c]$. Equation 3.17 can then be re-written as:

$$\left(\frac{\partial}{\partial z} - \frac{i}{2k(\omega,\rho)}\Delta_\perp - iK(\omega,\rho)\right)\hat{\mathcal{E}} = \frac{i\omega^2}{2k(\omega,\rho)c^2\epsilon_0}\hat{\mathcal{P}}_{NL}(\rho), \tag{3.18}$$

where $K(\omega,\rho) = k(\omega,\rho) - \omega/c$. In the special case of propagation in vacuum, equation 3.18 is simplified to:

$$\left(\frac{\partial}{\partial z} - \frac{i}{2k(\omega,\rho)}\Delta_\perp\right)\hat{\mathcal{E}} = 0, \tag{3.19}$$

which is invariant under the following transverse and longitudinal transformations: $r \to \eta r$ and $z \to \eta^2 z$, where η is a scaling parameter. Therefore, if $\hat{\mathcal{E}}(r,z,\omega)$ is a solution of equation 3.19, then also $\hat{\mathcal{E}}(r/\eta, z/\eta^2, \omega)$ will be a solution. Similarly, the more general equation 3.18 is invariant under the same transformation if, additionally, the gas density ρ is scaled as $\rho \to \rho/\eta^2$. Since the energy is proportional to the integral of the absolute square of the electric field, it scales as $\epsilon \to \eta^2\epsilon$. This scaling principle, applied to the specific case of HHG in gases, leads to simple scaling relations of all the generation parameters, which are presented in Tab. 3.1.

Table 3.1: Scaling relations for HHG in gases with respect to the parameter η and the input laser pulse energy ϵ_{in} for a fixed laser diameter before focusing, from [Hey+16b].

	Parameter	Scaling with η	Scaling with ϵ_{in}
input pulse energy	ϵ_{in}	η^2	-
focal length	f	η	$\sqrt{\epsilon_{in}}$
gas density	ρ	$1/\eta^2$	$1/\epsilon_{in}$
gas medium length	L	η^2	ϵ_{in}

The scale-invariant concept connects the generation parameters with each other. Therefore, if any technical condition limits one parameter, the others can be scaled accordingly to overcome the limitation. For a limited input pulse energy ϵ_{in}, the rescaling of focal length f and gas density ρ allows for a constant efficiency of the HHG process. However, this scaling model is based on equation 3.17, which is only valid within paraxial approximation. Therefore, limitations can arise at very tight focusing geometries where this approximation is not applicable.

Chapter 4

Semi-infinite gas cell as HHG generation configuration

The energy scaling concept presented in Section 3.3 is based on invariance properties of the forward-Maxwell equation, which do not depend on the specific experimental configuration. If the input pulse energy is limited to a certain value, all other parameters should be rescaled to obtain the same generation conditions. However, this is possible only if the experimental configuration is suitable for the right parameter rescaling. Depending on the experimental setup used for HHG, high gas pressures or very tight focusing size may be not supported, preventing an efficient generation process. An optimal experimental configuration must then be adapted for each special case. In this chapter, a *semi-infinite gas cell* (SIGC) is presented as HHG generation configuration and tested for input pulse energies of few hundreds of µJ.

4.1 Basic generation principles in SIGC

Commonly used configurations for HHG are gas nozzles [Hey+18; Mak+20], which often consist in pulsed valves to reduce the residual gas flow in the vacuum system, cell-based configuration [Bri+09; Ye+20] and gas-filled capillaries for guided-wave phase-matching [Run+98; Pop+12]. The semi-infinite gas cell [Pap+01; Sut+04; Bri+09; Ste+09; Kre+13] is a cell-based configuration

with the advantage of an abrupt transition from the gas part to vacuum. For this reason, it can be particularly suitable in case of critical vacuum requirements [CHW16].

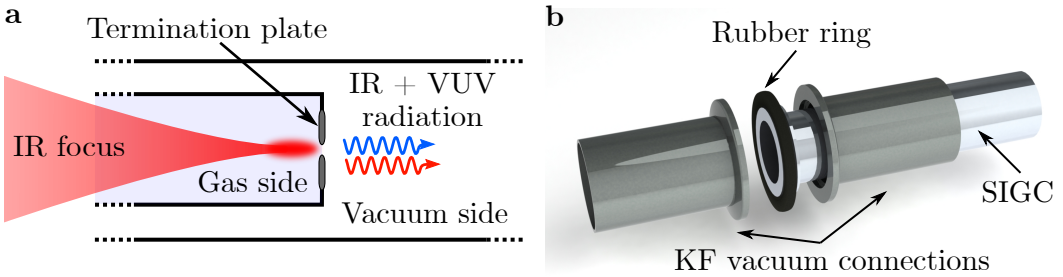

Figure 4.1: HHG in a semi-infinite gas cell (SIGC). a) Working principle: the laser focus drills a small opening in the metallic termination plate of the cell, which separates the gas from the vacuum side. b) Design of connection between a SIGC and the vacuum system where the cell is sandwiched between two standard KF flanges.

The working principle is presented in Fig. 4.1a. The system consists of a gas-filled cell, which is terminated by a metallic plate. The laser used to drive the harmonic generation is focused in the gas medium and drills an opening on the termination plate, comparable to the laser focus size. This laser-drilled hole is the only open connection between the gas and vacuum side and allows for the propagation of the generated radiation in the system. The termination plate acts as a differential pumping section limiting the gas load released in the vacuum side. This feature allows for a pressure difference of several orders of magnitude between the inside and the outside of the cell. Therefore, the SIGC configuration can be advantageous in systems with high-vacuum requirements and limited available space.

Another advantage of this configuration is the ease of implementation. The input laser does not need to be aligned to any already existing opening and any vacuum-compatible pipe can be used as body of the cell and inserted in the vacuum system. In the experiments described in the following, a stainless steel tube (see Fig. 4.1b) was used. The tube was directly connected to the vacuum system by means of a rubber ring sandwiched in a standard KF connection. The KF connection can then be easily and quickly opened to remove the cell when needed. The gas cell is then limited from a laser input window on one side and from the termination plate on the opposite side. In the presented implementation, a 0.5 mm thick aluminum disk was used as termination plate. A rubber ring on the inner side of the cell and a stainless steel connector, which

can be screwed onto the cell end, keep the Al plate in position and also ensure the air tightness of the gas cell. Without the laser-drilled opening, up to 8 orders of magnitude in pressure difference are achieved between the inside (1 bar of air) and outside (10^{-5} mbar) of the cell proving a complete isolation from the rest of the vacuum system. Moreover, the cell length can be adjusted as needed, such that the driving laser intensity does not damage the input window. However, possible nonlinear propagation effects within the SIGC could distort the driving laser pulse in case of high gas pressure, especially for short pulses with a large laser pulse spectral bandwidth. In this special case, a limitation on the cell length could arise.

The SIGC also inhibits typical disadvantages common to most of the gas cell configurations. Due to the unavoidable gas emission along the HHG propagation direction, a gas cell configuration can be affected by re-absorption of the harmonics photons after the generation point. In the specific case of low input pulse energies, a tight focus geometry and a high gas pressure is required, leading to short absorption lengths and to a potentially severe re-absorption of the generated XUV photons. The re-absorption can occur both inside the cell, depending on the position of the focus in the gas medium, and immediately outside the cell, in the gas jet emitted from the plate output opening. The re-absorption depends on the generated photon energies, on the gas medium used and on the residual gas present in the beampath behind the generation point. Specific pumping schemes can be implemented to minimize the gas emission, and consequently, the re-absorption outside the cell.

4.2 Generation at limited pulse energy

In order to test if the SIGC can be a suitable candidate configuration in case of limited input pulse energy, preliminary studies were performed with a customized commercial titanium-sapphire CPA laser system (Dragon, KMLabs Inc.). It generates laser pulses with 35 fs duration and a central wavelength of 790 nm. The output power of 1 W at 1 kHz repetition rate leads to a maximum pulse energy of 1 mJ, which can be reduced by means of an attenuator.

Fig. 4.2 shows a scheme of the experimental setup. After the attenuator, the beam is focused by a lens in gas, contained in the SIGC, for harmonics generation. In the experiments presented here, different focal lengths have been used accordingly to the selected driving pulse energy. The lens is placed on

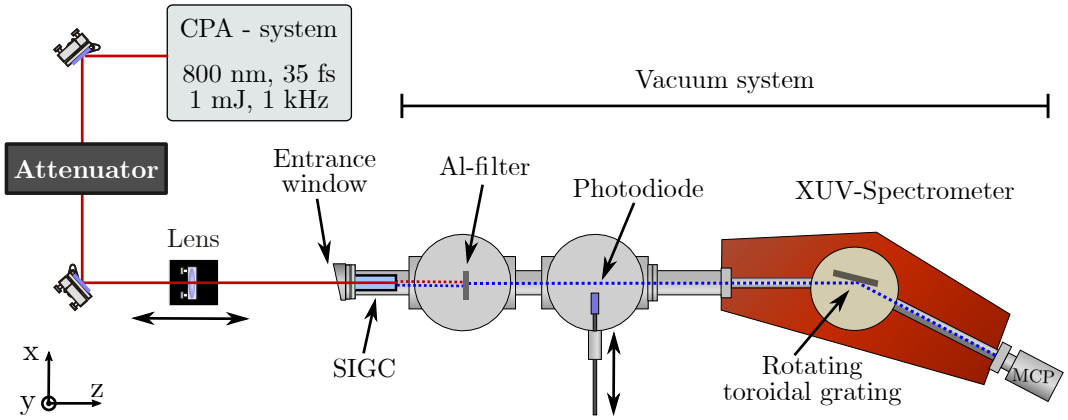

Figure 4.2: Scheme of the experimental setup used for preliminary studies on HHG in a semi-infinite gas cell. The output of a CPA laser system is focused in gas for the generation of high-order harmonics detected with a XUV spectrometer and photodiode.

an automated linear stage (M-UTM150CC.1, Newport) used to optimize the position of the laser focus with respect to the fixed position of the termination plate. The SIGC is inserted in a vacuum system with different pumping sections which terminates on a grazing incidence XUV-spectrometer (LHT 30, Horiba-Jobin-Yvon, 500 lines/mm) where the pressure is kept in the 10^{-7} mbar range. The harmonic spectrum is detected by a Chevron microchannel plates (MCPs) configuration with a metal anode. The anode signal is then amplified by a two phase lock-in analyzer (5208 Princeton Applied Research) and acquired on the computer. An example of harmonic spectrum generated in argon is presented in Fig. 4.3. Harmonics up to order 33, corresponding to ∼24 nm or 51 eV, are resolved. Side peaks visible in the spectrum (indicated with the blue numbers in the figure) are due to the grating's second order of diffraction which cannot be completely suppressed.

While the XUV spectrometer analyzes the spectral information of the harmonic radiation, the generated pulse energy can be measured by means of a calibrated photodiode, which is also an useful tool for the optimization of the generation process. For this purpose, a large area XUV photodiode (AXUV576, OptoDiode) is inserted in the beampath before the spectrometer (see Fig. 4.2). Due to its sensibility to the IR light (detector photon responsivity from datasheet >0.4 A/W for 800 nm compared with ∼0.26 A/W for 50 nm), it is important to block the remaining fundamental light before the detector. To this end, aluminum filters of different thicknesses can be inserted in the

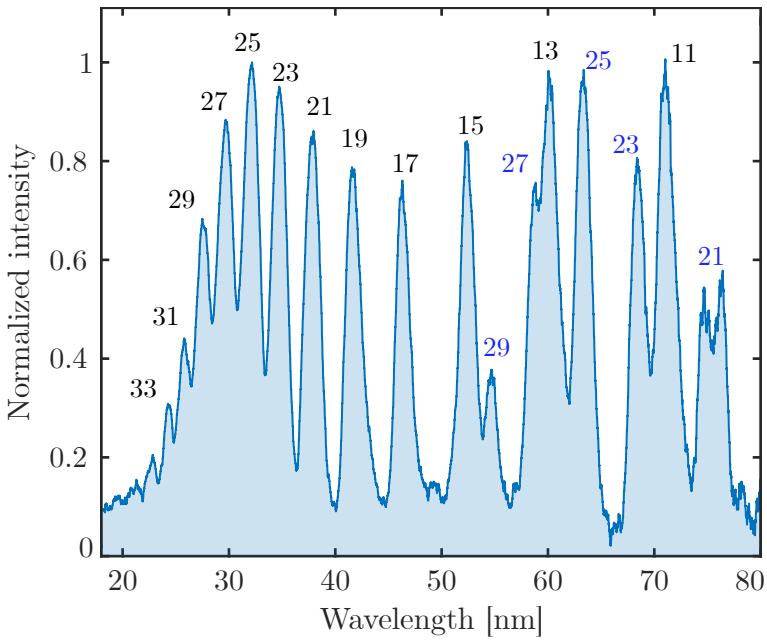

Figure 4.3: Harmonic spectrum generated with 90 mbar of argon in the SIGC. Input laser pulse energy of 300 µJ focused with a 300 mm focal length. The black numbers indicate the harmonic orders. The blue numbers correspond to harmonics of the grating's second order of diffraction.

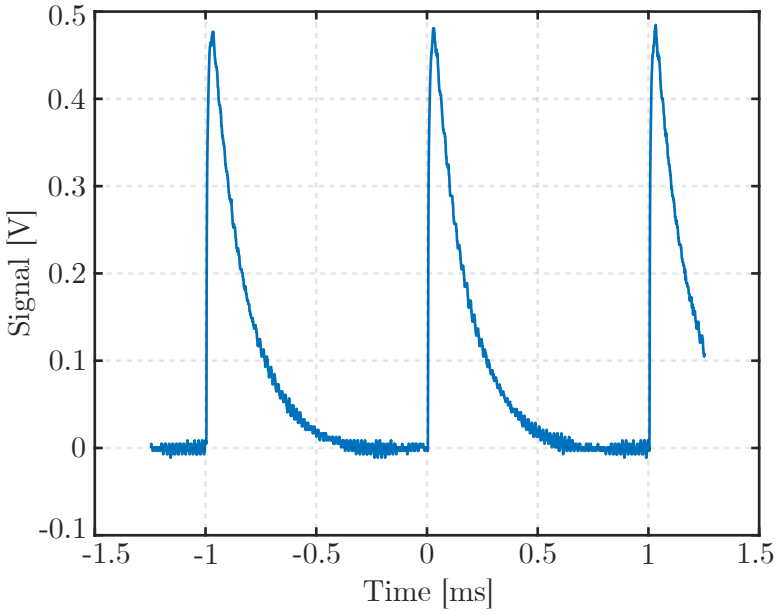

Figure 4.4: Typical photodiode trace of the harmonic signal after blocking of any remaining IR radiation by two aluminum filters.

beampath in a rotatable filterwheel. An additional 0.1 µm thick Al filter is placed just in front of the photodiode to filter out any scattered infrared or visible light. The detector is then connected to a low-noise preamplifier (SR570, Stanford Research Systems) and the signal is recorded by an oscilloscope. Fig. 4.4 shows a typical photodiode trace of the harmonic signal. Due to the repetition rate of 1 kHz, the contribution of every pulse is temporally resolved. By taking in consideration the sensitivity chosen on the preamplifier and the photodiode response function, the generated VUV pulse energy can be estimated from the area under the trace. For details on the necessary analysis see Section 6.1.2.

4.2.1 Signal optimization

By taking advantage of the direct feedback given by the photodiode signal, the generation parameters can be optimized with respect to the VUV signal detected. The optimization procedure was realized for three different ranges of input pulse energy ϵ_{in} at: 700 µJ, 500 µJ and 300 µJ. The parameters under consideration were the gas pressure in the cell p, the laser focus position in the gas medium z_f and the laser intensity, which was varied through the input pulse energy ϵ_{in} and the focal length f for a constant input beam diameter.

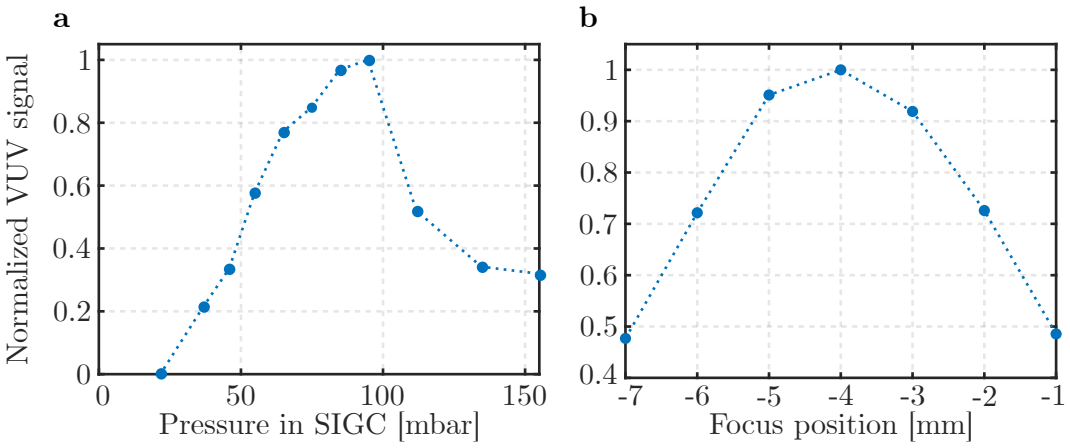

Figure 4.5: Normalized VUV pulse energy as a function of: a) the argon gas pressure p in the SIGC and, b) the focus position in the gas medium z_f, where negative values indicates positions inside the cell. Input IR pulse energy $\epsilon_{in} = 300$ µJ and focal length $f = 300$ mm.

Each of these parameters was optimized in such way that the harmonic signal detected on the photodiode reached saturation. Fig. 4.5 shows an example of

the VUV signal trend with respect to the argon gas pressure and focus position for a fixed input energy of 300 µJ and focal length equal to 300 mm. In both cases the VUV signal reaches a maximum value before decreasing. Similarly, in order to find the optimal IR intensity, several focal lengths from 200 to 750 mm were tested for each of the three input pulse energies considered. A scan of the IR pulse energy around the value of interest ensures that energy saturation of the VUV signal is achieved. Fig. 4.6a shows the VUV pulse energy for different focal length f with an input IR pulse energy around the value of 300 µJ. Clearly, the maximum signal is achieved in case of a focal length of 300 mm. Note that for each focal length considered, the gas pressure and the focus position in the cell were optimized in order to reach the maximum VUV signal. As expected the same focal length does not maximize the signal for all input pulse energies. Fig. 4.6b shows the conversion efficiency of the HHG process for a focal length of 300 mm, optimized around each range of the input pulse energies under investigation. Clearly the maximum conversion efficiency is achieved for $\epsilon_{in} \sim 300$ µJ. Instead, at higher input pulse energies the laser intensity is not optimal, and the generation process is less efficient despite the optimization of gas pressure and focus position.

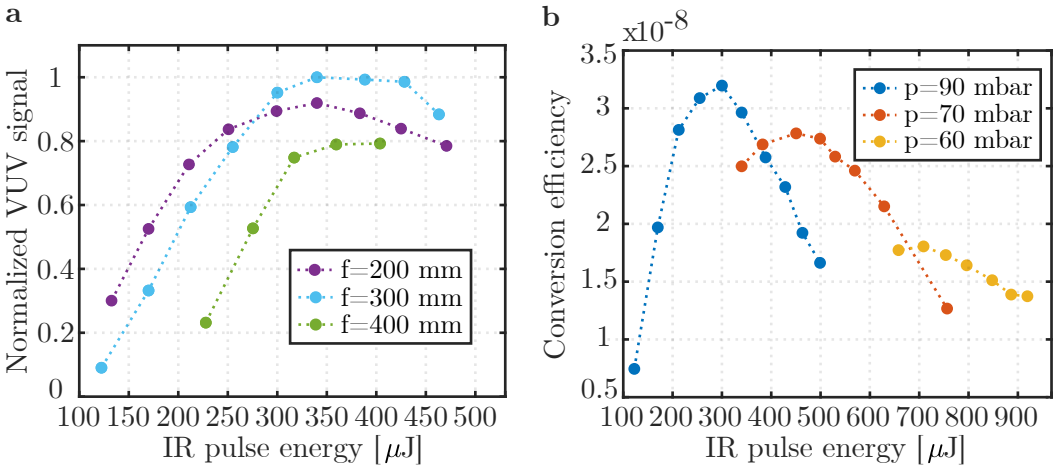

Figure 4.6: Optimization of focal length with respect to the input pulse energy. a) Energy saturation for different focal lengths with IR pulse energy around 300 µJ. b) Conversion efficiency of the HHG process for a fixed focal length of 300 mm. The argon gas pressure and the position of the laser focus in the cell are optimized for each curve.

Spectral dependency on generation parameters. It should be noted that, by changing the generation parameters, not only the VUV pulse energy

changes but also the spectral information itself does. In the work of Steingrube *et al.* [Ste+09], an extensive study of the phase-matching in a SIGC is presented and the dependency of the process on different generation parameters is addressed. Fig. 4.7 shows the measured harmonic spectrum as a function of focus position z_f in the cell. As also reported in [Ste+09], the lower order harmonics are more efficiently generated for focus positions outside the SIGC, i.e. $z_f \geq 0$, while higher order harmonics emission prefers focus positions inside the cell, i.e. $z_f < 0$. This behavior can be explained by considering the spatial distribution of the laser intensity. The intensity required for the generation of higher orders is confined in a narrow volume around the laser focus. For $z_f \geq 0$, the focus is located mostly outside the gas medium, preventing the generation of higher orders. The interaction volume is, however, extended for lower orders and can still partially overlap with the medium even for $z_f \geq 0$, allowing therefore their generation. For focus positions inside the SIGC, all orders are generated but their yield is determined by absorption, which is stronger for lower orders, leading to a rapid decay of their signal and a slower one for higher orders.

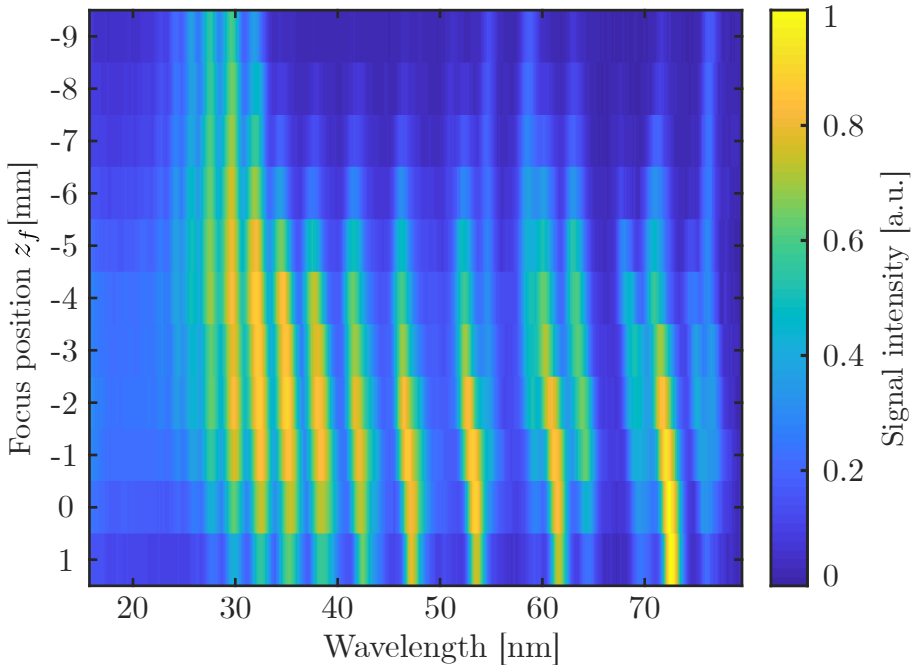

Figure 4.7: HHG spectrum as a function of focus position z_f. Parameters used $p = 90\,\text{mbar}$ of argon, $\epsilon_{in} = 300\,\mu\text{J}$ and $f = 300\,\text{mm}$. Lower orders are more efficiently emitted for $z_f \geq 0$ (outside the cell), while higher orders for $z_f < 0$ (inside the cell).

The harmonic spectrum can change also with respect to the focal length f and the gas pressure p. The focal length, as well as the input driving energy, is

strongly related to the laser intensity, which determines the spectrum cutoff energy E_{cutoff} (see Section 3.2.1) and the ionization rate in the medium. Typically, high ionization rates cause depletion of the generation medium and defocusing of the driving beam by free electrons, precluding phase matching [BCG01]. Moreover, the temporal profile of the laser intensity, especially for ultrashort pulses, can lead to spectral broadening and spectral splitting in the HHG spectrum. As mentioned in Section 3.2.2, the wavevector mismatch Δk_d is induced by the dipole phase accumulated by the electron during its excursion in the continuum. This phase contribution depends on the laser intensity and on its evolution in time. Alike the case of self-phase modulation in a Kerr medium, this time-dependent phase modulation leads to a chirp of the harmonic radiation. A blue (red) shift is induced at the rising (falling) edge of the laser pulse, leading to a *non-adiabatic* spectral broadening or splitting of single harmonic orders in the frequency domain [SLL95; Kan+95]. Similar effects can be caused by the free electrons density, which depends on the ionization rate in the medium and it also varies with the temporal intensity profile. During the rising edge of the pulse, the ionization rate increases leading to a higher free electrons density compared to the falling edge of the pulse. Therefore the plasma index of refraction n_q^e and the wavevector mismatch Δk_p are time-dependent. This rapid change of the phase induced by free electrons results in a *adiabatic* blue shift and spectral splitting in the HHG spectrum [Wan+00; Zho+00]. In contrast to the previous case, adiabatic effects depend also on the gas pressure, which influences the ionization rate in the medium. Non-adiabatic and adiabatic effects have both been reported for HHG in SIGC configurations [BIJ08; Ste+09].

In conclusion, there is a strong dependency of the HHG process on the harmonic order q (see Section 3.2.1 and 3.2.2) and the generation parameters should be optimized with respect to the spectral range of interest in order to achieve an efficient generation process. However, the aim of the optimization procedure presented here is to maximize the average harmonics signal emitted in the full HHG spectrum. No specific harmonic order is selected. The only restriction is due to the presence of Al filters in the beampath, which limits the photon energy range detectable by the XUV photodiode to >17 eV. Therefore, the influence of the generation parameters on the HHG spectral components is neglected in this study, but it should be taken in consideration if a specific spectral range is selected.

4.2.2 Energy scaling test

As already mentioned, in order to test the high order harmonic generation in a SIGC configuration at different input pulse energies, the optimization procedure described in Section 4.2.1 was repeated for $\epsilon_{in} = 700\,\mu J$, $500\,\mu J$ and $300\,\mu J$. The optimum generation parameters found are presented in Tab. 4.1 indicated as "Exp."-values.

Table 4.1: Optimal focal length f and gas pressure p for HHG at different input IR pulse energies ϵ_{in} with resulting VUV pulse energy ϵ_{out}. The "Exp."-values are found experimentally, while the "Calc."-values are calculated downscaling the ϵ_{in} =700 µJ experimental case by the energy scaling relations of Tab. 3.1.

	ϵ_{in} [µJ]	f [mm]	p [mbar]	ϵ_{out} [pJ]
Exp.	700	500	35	20.8
Exp.	500	400	50	15.5
Calc.	500	423	49	14.9
Exp.	300	300	90	9.6
Calc.	300	327	82	8.9

As expected, for lower ϵ_{in} tighter focusing geometries and higher gas pressures are necessary in order to reach the laser intensity and ionization rate in the medium required for efficient HHG. The performance of the HHG process is given by the VUV pulse energy generated, indicated as ϵ_{out} in the table. Assuming that the optimized parameters allow for the same generation conditions at all ϵ_{in} considered, the VUV pulse energy ϵ_{out} is expected to decrease linearly with the decreasing input energy. The absolute conversion efficiency of the process would therefore be constant with respect to the input energy. The experimental data acquired are in good agreement with this prediction. As shown in Fig. 4.8, the conversion efficiency of the generation process reaches comparable maximum values for each IR input pulse energy range that has been considered for the optimized generation parameters. Moreover, the experimental case of ϵ_{in} =700 µJ can be downscaled to 500 µJ and 300 µJ following the energy scaling relations reported in Tab. 3.1. These relations do not depend on the specific experimental configuration used for HHG, but are only based on invariance properties of the Maxwell equations. A comparison between the experimental and downscaled parameters, indicated as "Calc."-values in Tab. 4.1, shows a good agreement ensuring the validity of the procedure followed.

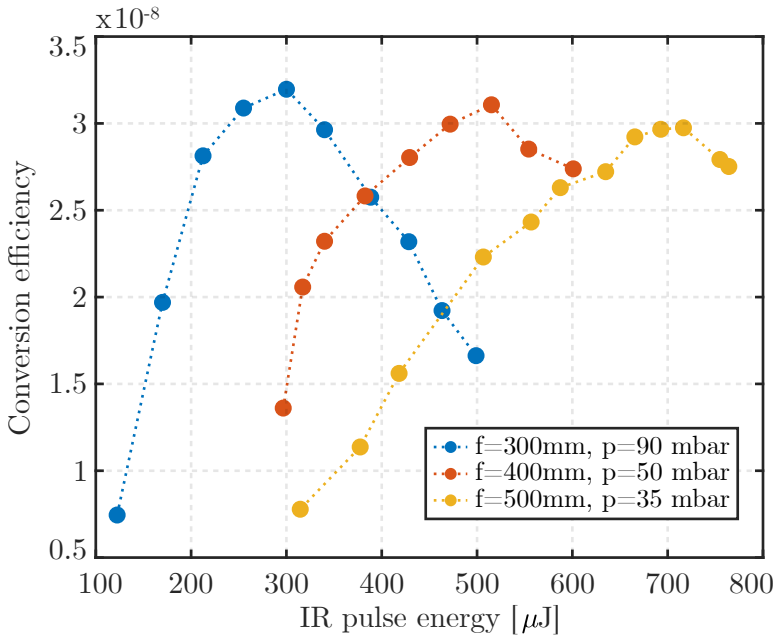

Figure 4.8: Maximum conversion efficiency achieved at the three investigated input pulse energy ranges: 300 µJ (blue curve), 500 µJ (red curve), and 700 µJ (yellow curve). Focal length and gas pressure used are found by applying the optimization procedure described in Section 4.2.1 for each case.

It should be noted that the conversion efficiency of the generation process depends on the dipole emission of the single atom response and on macroscopic effects. In order to achieve table-top efficiencies both mechanisms must be optimized, including parameters which were not investigated and kept constant in the presented procedure. As already mentioned, the single atom response is strictly connected to the gas species used. The cutoff equation 3.5 implies that, for constant laser intensity, higher ionization potentials allow to extend the harmonics spectrum to shorter wavelength. However, the smaller ionization cross-section reduces the overall process efficiency when compared to heavier gas species with lower ionization potential. The conversion efficiency depends strongly also on the driving laser wavelength λ. Theoretical and experimental studies [Tat+07; Sch+07; FMS08; Shi+09] have shown a scaling $\propto \lambda^{-[5-6]}$ at constant intensity due to the spreading of the electron wavepacket in space and time. Therefore, the generation of a specific harmonic order in the plateau region is more efficient if driven with shorter laser wavelengths than longer ones. The harmonic spectrum is, however, influenced by λ as well. Due to the quadratic dependence of the ponderomotive energy U_p on the driving wavelength (see equation 3.4), the cutoff energy is higher for long driving

wavelength allowing the generation of higher harmonic orders but with lower efficiency. The dipole emission depends also on the driving laser intensity I. The harmonics yield increases with higher laser intensities up to a saturation level, as shown in Fig. 4.6. The laser intensity in the medium, however, does not depend only on the input pulse energy and the focal length, which are included in the optimization procedure, but also on the focus beam quality. Optical aberrations or poor M^2-factors can lead to a focus spot very different from the ideal case of a diffraction-limited beam. The spatial distribution of the laser energy in the medium is then not optimum and the effective intensity available for the HHG process is affected. A measurement of the focal beam size with respect to the propagation distance for the laser system used in the experiments is depicted in Fig. 4.9. The measurement shows a M^2-factor of (1.24 ± 0.08) along the x-axis and of (1.65 ± 0.02) along the y-axis, leading to an elliptical focus spot. The beam is also affected by residual astigmatism visible in the not-coincident focus positions for the two axes. A correction of these not ideal focus conditions could lead to a more favorable spatial distribution of the laser energy in the medium. Optimum conversion efficiencies are obtained for laser intensities just below the saturation level over a large emitting gas volume. To this end, a fine tuning of both the input energy and focal size is required, including a fine optimization of the beam size before focusing [Her+02].

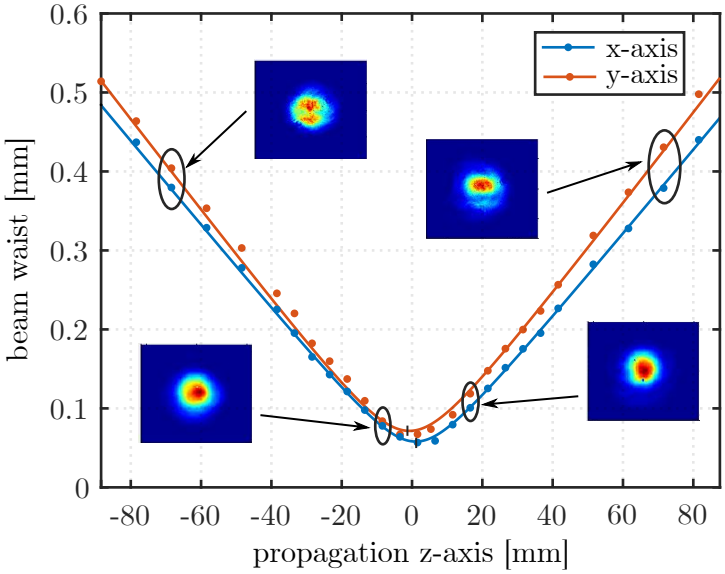

Figure 4.9: Spatial evolution of the laser beam waist $w(z)$ as a function of the beam propagation z-axis position. A M^2-factor of (1.24 ± 0.08) is calculated along the x-axis and of (1.65 ± 0.02) along the y-axis.

In conclusion, in order to achieve table-top conversion efficiencies all parameters influencing the HHG process, both in the single atom response and in the macroscopic effects, must be optimized with respect to the harmonic spectral range of interest. Nevertheless, the analysis presented here is based on the comparison between the relative performance of the SIGC configuration at decreasing input pulse energies, despite the maximum conversion efficiency achieved. Therefore, the trend observed in Fig. 4.8, which shows that similar generation conditions are achieved for all investigated input pulse energies, remains valid.

From the results presented in this Section, no limitation on the use of the SIGC as generation configuration is observed in the considered input pulse energy range of few hundreds µJ. Nowadays, this energy range is provided by state-of-art femtosecond lasers at repetition rates which vary from few Hz up to hundreds of kHz. Shorter pulse durations are also achievable, which allow to reach the required intensity for efficient HHG with less tight focusing geometries. Note that there is no implicit lower limit for the value of ϵ_{in} as long as the required generation conditions are met. In particular, the SIGC was chosen as suitable generation configuration for the new VUV beamline at FLASH. In this specific case, the generation of high-order harmonics in gas is driven by an infrared OPCPA laser system with intra-burst repetition rate of 100 kHz. The system provides pulse energies up to 225 µJ with pulse duration of <20 fs at the HHG source. The resulting peak power available is of the order of 10-12 GW, which is included in the range tested in Tab. 4.1 where the peak power spans from 8 to 19 GW. A detailed description of the beamline and its commissioning results is given in the following chapters.

Chapter 5

VUV beamline at FLASH2

In this chapter the new vacuum ultraviolet beamline design for pump-probe experiments at the free-electron laser FLASH in Hamburg is presented. The VUV source is based on high-order harmonic generation from a femtosecond laser and is integrated in the already existing FL26 beamline, which features a reaction microscope [Ull+03] for the investigation of ionization processes dynamics in gas targets. With this unique setup, the combination of a FEL and a HHG-based source can be achieved, opening new opportunities for two-color pump-probe studies in the VUV/XUV spectral range.

5.1 FL26 beamline

FLASH is the world's first XUV and soft X-ray free-electron laser (see Section 2.1). It operates in SASE mode and presents two distinct undulator beamlines which work in parallel [FPA+16]: the FLASH1 and the FLASH2 beamlines. In the FLASH1 experimental hall, four experimental stations are available for users: the beamline BL1 which features the CAMP endstation for electron- and ion-spectroscopy and imaging experiments, BL3 which combines the XUV FEL pulses with THz pulses for pump-probe experiments, and the beamlines PG1 and PG2 equipped with high-resolution plane grating monochromators for photoelectron spectroscopy, X-ray diffraction and holography. In the experimental hall of FLASH2 two more additional beamlines are available:

FL24 which covers the full wavelength range of FLASH2 and can be combined with users endstations, and FL26 which features a reaction microscope (REMI) as permanent endstation and it is now integrated with the novel HHG-based VUV source for two-color experiments.

Fig. 5.1 shows a CAD drawing of the REMI endstation [Sch+19c]: the FEL beam is aligned through several differential pumping stages and reaches the XUV optics chamber. Here a split-and-delay unit can be used to perform single-color pump-probe experiments. It consists of a split mirror which divides the FEL in pump and probe pulses while controlling their relative delay. The FEL radiation is then focused by an ellipsoidal mirror into the reaction microscope, where various atomic or molecular targets can be injected by means of a supersonic gas-jet.

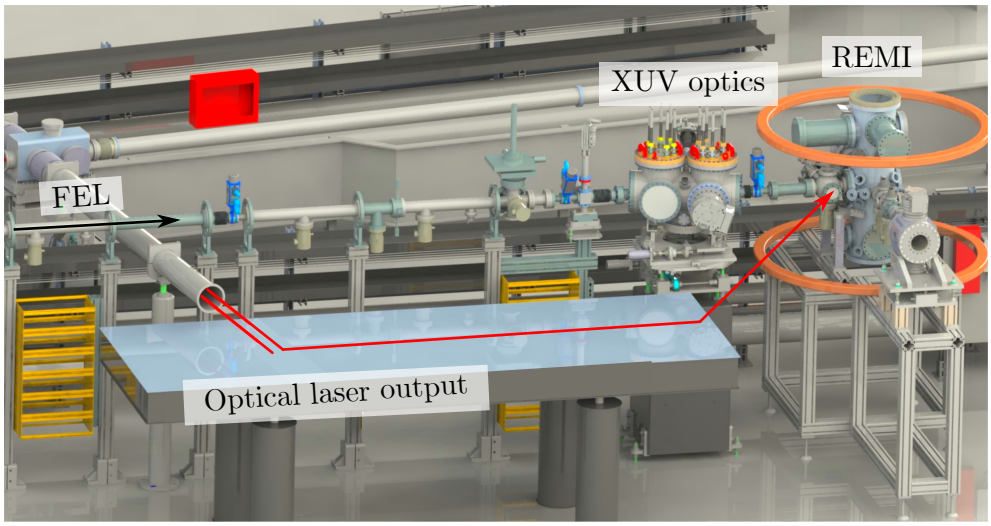

Figure 5.1: CAD design of the REMI endstation at the FL26 experimental beamline before the installation of the VUV source. For a complete and detailed overview of the REMI endstation at FL26 see Schmid *et al.* [Sch+19c].

Additionally, the infrared optical laser of the experimental hall [Lan+19], synchronized to the pulse pattern of the FEL, can be coupled into the beamline for XUV-IR pump–probe experiments. The laser enters the beamline, after a 50 cm focusing lens, under a 90 degrees angle and it is coupled collinear to the FEL. By making used of the different size of the two beams, a incoupling mirror with a central hole allows the propagation of the small FEL diameter (< 3 mm in this position), while reflecting the bigger IR beam. The two foci are then spatially and temporally overlapped on the target.

In REMI, the ionization and fragmentation dynamics of the target can be studied by reconstructing the 3D momentum of ions and electrons that emerge from the fragmentation. The coincidence detection of ions and electron, with 4π acceptance angle [Mos+96], is achieved by guiding the fragments onto time and position sensitive detectors [Cza+07] thanks to a specific arrangement of electric and magnetic fields [Ull+03]. An overview of the recent results obtained at the REMI endstation can be found in Meister *et al.* [Mei+20]. Three different schemes of operation have been implemented: the focus of a single FEL pulse, a FEL-pump FEL-probe scheme by making use of the split-and-delay unit, and a XUV-pump IR-probe configuration. Moreover, the endstation will be soon extended with a XUV spectrometer placed downstream of REMI. The spectrometer will allow for shot-to-shot analysis of the FEL pulses and can be employed in transient absorption spectroscopy experiments.

In this already innovative setup, the addition of a HHG-based vacuum ultraviolet beamline establishes a unique combination of a reaction microscope with three state-of-the-art light sources for time-resolved studies.

5.2 VUV beamline

The VUV setup installed at the beamline FL26 can be divided in three main parts, which are described in details in this chapter: the HHG source (see Section 5.2.2), where high-order harmonics of the driving wavelength are produced, the inline spectrometer (see Section 5.2.4) for the detection of the VUV light and the incoupling chamber (see Section 5.2.5) placed in the crossing point with the FEL beamline.

Fig. 5.2 shows the general scheme of the setup. The NIR optical laser is focused in a gas medium in order to drive the generation of high-order harmonics. The emitted beam propagates in the vacuum system up to the inline spectrometer where the VUV spectral components are resolved. At the crossing point with the FEL beamline, an incoupling mirror can be inserted in the beampath. In this configuration, the VUV beam does not reach the inline spectrometer but it is reflected toward REMI. After this position, both FEL and VUV beams propagate parallel to each other and are focused by the ellipsoidal mirror. The split-and-delay unit can then be used to control the temporal delay between them for FEL-VUV pump-probe experiments.

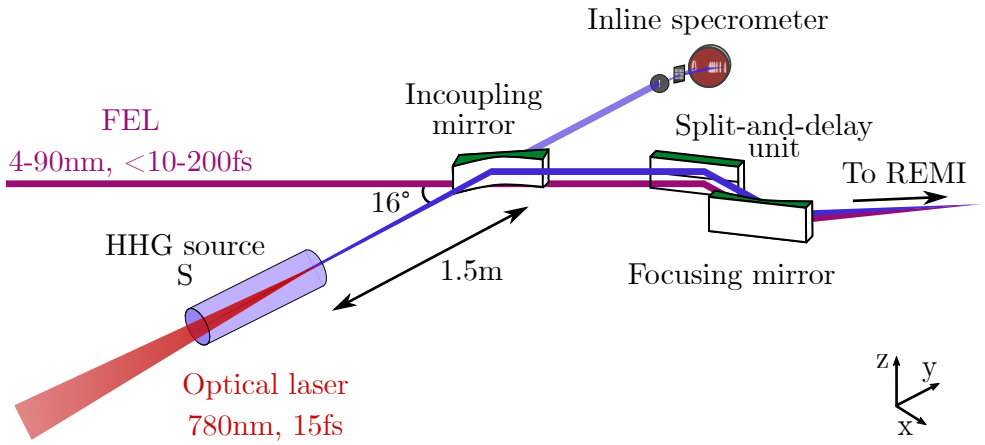

Figure 5.2: Schematic of the VUV beamline. Ultrashort, near-infrared laser pulses are focused in gas for the generation of high-order harmonics (HHG source, S) in the VUV spectral range. The beam is then coupled in the FEL beamline and focused in a reaction microscope (REMI). The split-and-delay unit of the endstation can be used to control the temporal delay between FEL and VUV pulses.

Since the early stages of the beamline's design, it was of great importance to fix two main critical parameters: the distance from the HHG source S to the incoupling mirror and the angle between the two beamlines. The setup had to be very compact to be suitable for the limited available space in the experimental hall. However, the connection of a high-pressure gas target for HHG to an ultra-high vacuum FEL beamline requires an adequate differential pumping system along the length of the setup. Taking these requirements in consideration, the distance from the HHG source and the incoupling mirror was fixed to 1.5 m after a first initial design. This distance allows for the installation of a filterwheel, essential to suppress the remaining infrared light after the generation process, and for several differential pumping stages, which ensure the required pressure ($<10^{-7}$ mbar) at the intersection point between the two beamlines.

Additionally, the incidence grazing angle of the VUV beam on the incoupling mirror was fixed to 8° (see Section 5.2.5 for more details) which corresponds to a total angle of 16° between the two beams. With this small grazing angle, the carbon coating of the mirror provides a reflectivity >70% in the VUV spectral range. An even smaller grazing incident angle could increase the VUV reflectivity on the mirror, but would make the angle with the FEL and VUV beamlines too narrow for the practical installation of the vacuum components.

Following these preliminary decisions, the work proceeded with the detailed design of the whole VUV beamline, depicted in Fig. 5.3, which was installed from June 2018 to May 2019 and it is presented in the following.

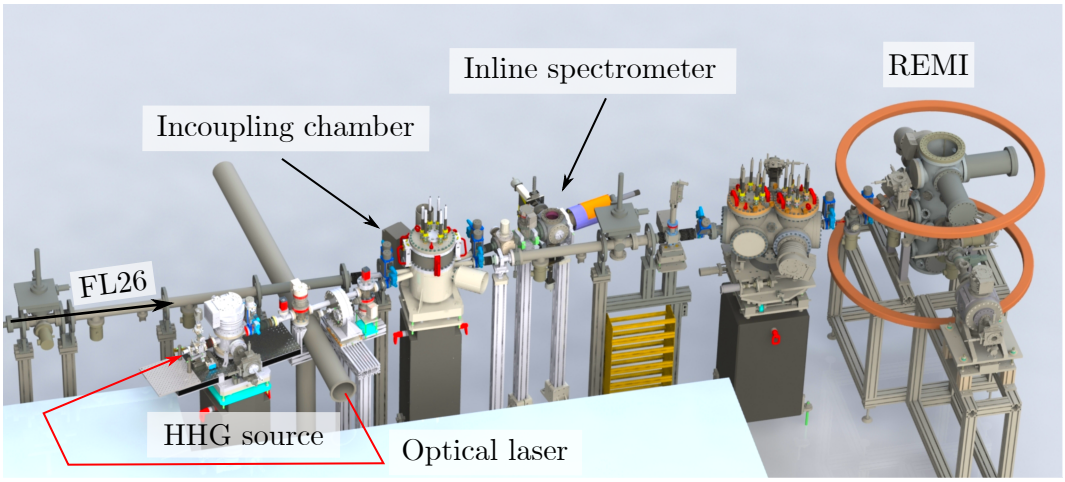

Figure 5.3: CAD drawing of FL26 and the REMI endstation after the installation of the VUV beamline. The optical laser beam is focused in gas for the generation of VUV light, which is coupled into FL26. The FEL and VUV beamlines are connected by means of the incoupling chamber, where the pressure is required to be $<10^{-7}$ mbar for a safe operation of the REMI endstation.

5.2.1 Driving laser optical setup

The pump-probe laser [Lan+19] available at the FLASH2 experimental hall, is based on optical parametric chirped pulse amplification. It consists of two chirped pulse laser amplifiers: a sub-500 femtosecond Yb:fiber laser for the generation of broadband OPCPA seed pulses, and a picosecond Yb:YAG Innoslab laser system, which provides a high power pump. Both CPAs are seeded by a common low-noise Yb laser oscillator optically synchronized to the FEL master oscillator via length-stabilized fibers [Sch+15]. Timing drifts in the amplifier system introduced by environmental changes are actively compensated below 6 fs rms [Sch+19a]. The system matches the burst-mode timing structure of the FEL featuring pulse trains with 10 Hz repetition rate. The maximum burst duration in the pulse train is 800 µs and the intra-burst repetition rate can vary up to 1 MHz. The typical operation mode at the REMI endstation presents 100 kHz intra-burst repetition rate, leading to a total of 80 laser pulses in one burst with peak-to-peak pulse energy stability of <5 % rms.

The radiation of central wavelength 780 nm, selected from the OPCPA

spectral range tunable from 680 to 920 nm, is transported in vacuum via a 40 m long relay-imaging beamline to a modular optical delivery setup (MOD) close to FL26. The MOD2.6 consists on a laser tent which contains the optical setups for the optical beam, as well as part of the VUV beamline. The beam enters the MOD2.6 through a laser shutter, as shown in Fig. 5.4, with a typical beam waist of 3 mm and an average pulse energy of 350 µJ. An active drift stabilization system compensates for the beam pointing to 8% rms of the beam diameter measured over 120 hours (similar to the laser performance before beam transport). The stabilization system consists of two piezo actuated mirrors (M1 and M2 in Fig. 5.4) connected to a two-camera system. A 0.5 mm thick beamsplitter (BS1) sends ∼4% of the beam to a first beam camera (C1) which monitors the position of the unfocused collimated beam. A small reflection of the beam is instead focused and monitored by a second camera (C2). This two-camera system provides then the feedback to actively correct the alignment of the two piezo actuated mirrors.

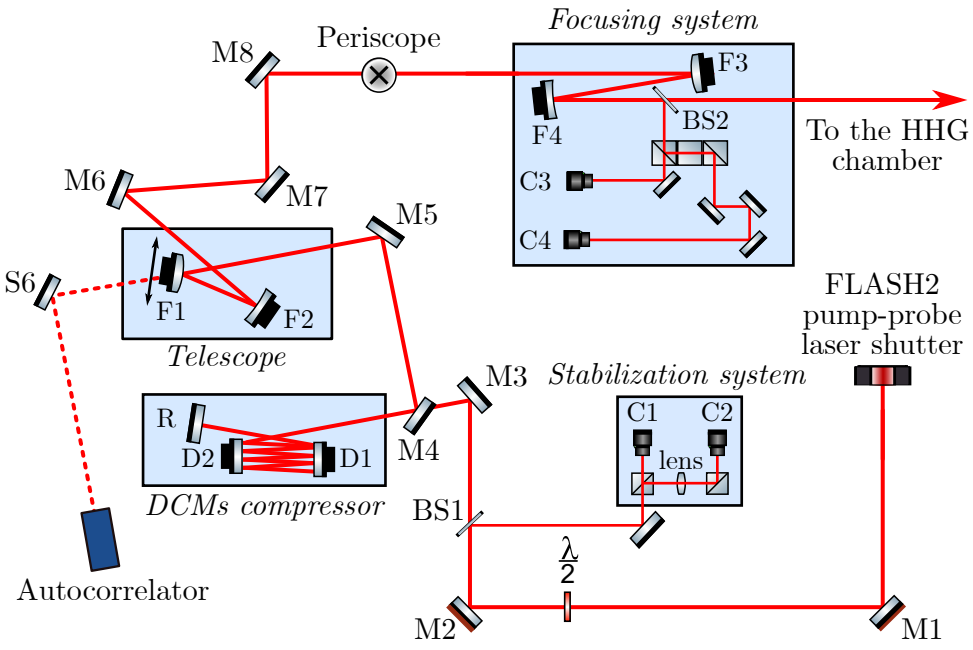

Figure 5.4: Schematic of the optical setup in the MOD2.6 for the VUV generation. The beam pointing is actively corrected with a drift stabilization system based on cameras, C1 and C2, and two piezo actuated mirrors, M1 and M2. The pulses are then compressed down to 15 fs in a DCMs compressor and focused for the generation of the VUV light into the HHG chamber.

The laser pulses are then compressed by a pair of double-chirped mirrors

(DCMs). The beam enters the compressor (from mirror M3 in Fig. 5.4) and, after 8 bounces on the chirped mirrors, it is reflected backward from a retroreflector (R) lowered by ∼1 cm in height. The beam is then reflected again for 8 bounces on the chirped mirrors for a total negative dispersion of $-1200\,\mathrm{fs}^2$ ($-75\,\mathrm{fs}^2$ per bounce). A D-shaped mirror (M4) steers the outcoming beam to the next part of the optical setup. By means of an autocorrelator, accessible directly after the compressor, it is possible to measure the pulse duration and change the number of bounces on the chirped mirrors accordingly. Glass plates of different thickness, as well as a pair of thin glass wedges, are available in the MOD2.6 and can be easily installed in the beampath for fine readjustment of the dispersion. During commissioning of the VUV beamline, a pulse duration of 15 fs (FWHM) was achieved, as shown in Fig. 5.5.

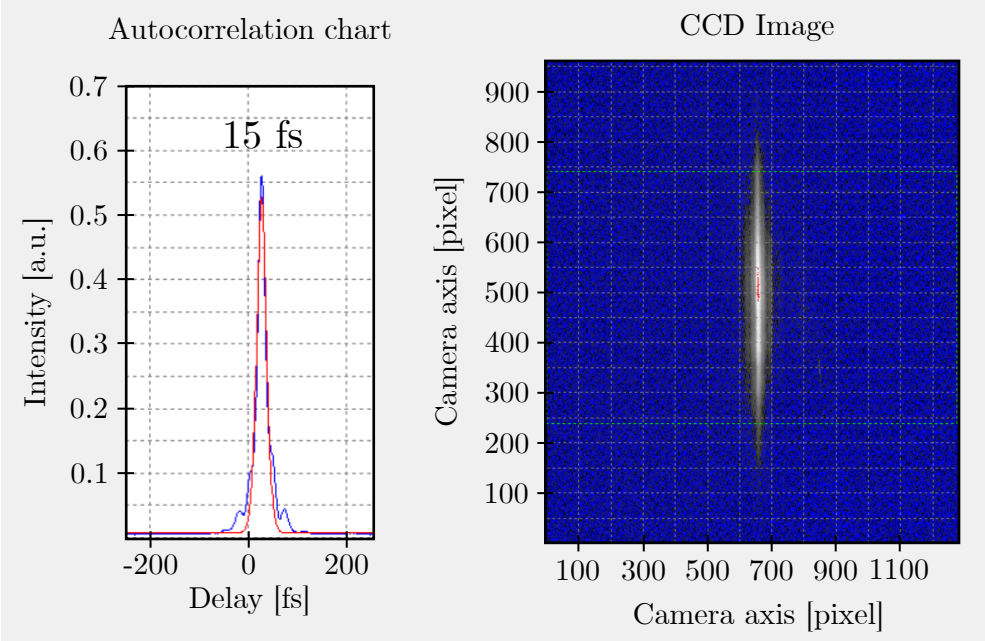

Figure 5.5: Autocorrelator trace after the DCMs compressor.

In order to optimize the focusing conditions for the generation process, two telescopes are installed in the optical beampath: a first one for the astigmatism correction and a second to focus the beam at the required position inside the HHG chamber. Since the beamline is ∼1.5 m to the ground, higher than the optical table, the focusing telescope (mirrors F3 and F4) is placed on a breadboard fixed close to the vacuum system together with a two-camera system, similar to the one used for the stabilization of beam pointing. These two cameras (C3 and C4) are used as reference for the alignment of the IR

beam through the full VUV beamline up to the inline spectrometer. However, the place available on the breadboard is limited and does not allow for much flexibility in the adjustment of the mirrors and their incidence angles. For this reason, it is convenient to use the previous telescope (mirrors F1 and F2 in Fig. 5.4) in order to compensate for astigmatism and minimize the laser focus size in the gas medium. To this end, the angles of incidence of the two mirrors are optimized while monitoring the virtual focus of the beam on the breadboard (camera C4). To avoid any distortion or artifacts in the virtual focus, the direct focus beam can be observed by simply exchanging the beamsplitter BS2 with a flat mirror, as long as enough neutral-density (ND) filters are used to protect the camera chip. The distance between the mirrors of the telescope is chosen in order to ensure the collimation of the beam, which is therefore guided by a periscope on the breadboard. Here, pulse energies up to 225 µJ have been measured.

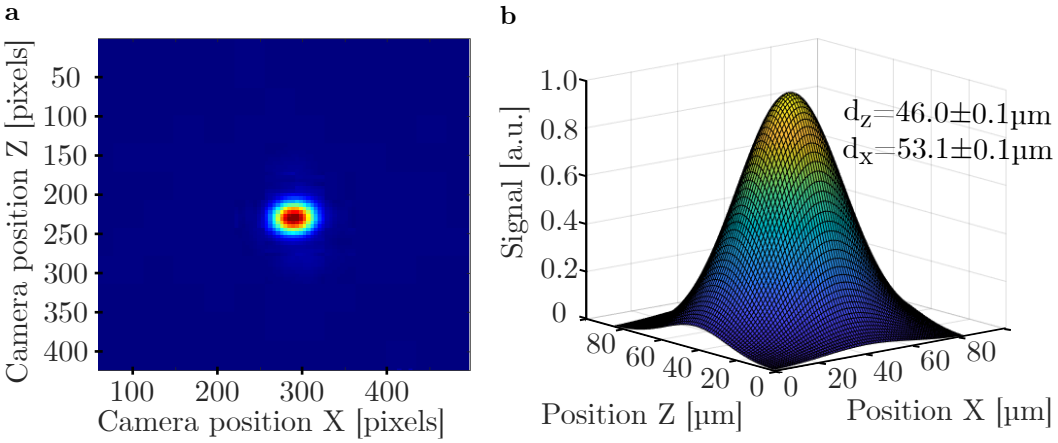

Figure 5.6: Focused driving beam for HHG. a) Camera image of the focused infrared beam in the HHG chamber. b) 2D Gaussian fit of the spot estimates a beam size around 50 µm. The focusing conditions need to be adjusted with respect to the laser performance to reach a peak intensity $>10^{14}$ W/cm^2 for high-order harmonic generation.

As already mentioned, the HHG process requires an intensity in the order of 10^{14} W/cm^2. During different commissioning experiments, the focal lengths used in the two telescopes, have been adjusted to achieve the intensity of interest with respect to the laser performance in terms of pulse energy. An example of focused beam is shown in Fig. 5.6. In this case, the first telescope consists of one defocusing mirror and one focusing mirror, of focal length -250 mm and 375 mm respectively, and acts as beam expander to increase the beam

waist to approximately 4.5 mm. The distance between the mirrors is fixed at 125 mm. On the breadboard, to accommodate the big beam size, 2 inches mirrors are used. Focal lengths of −150 mm and 200 mm respectively, with 165 mm distance, are then used to focus the beam down to a diameter of 50 µm.

5.2.2 HHG source

The first part of the vacuum beamline, depicted in Fig. 5.7, consists in the HHG chamber in which a semi-infinite gas cell for the generation of VUV radiation is inserted, followed by a series of differential pumping stages and a filterwheel used to tune the spectral range of the source.

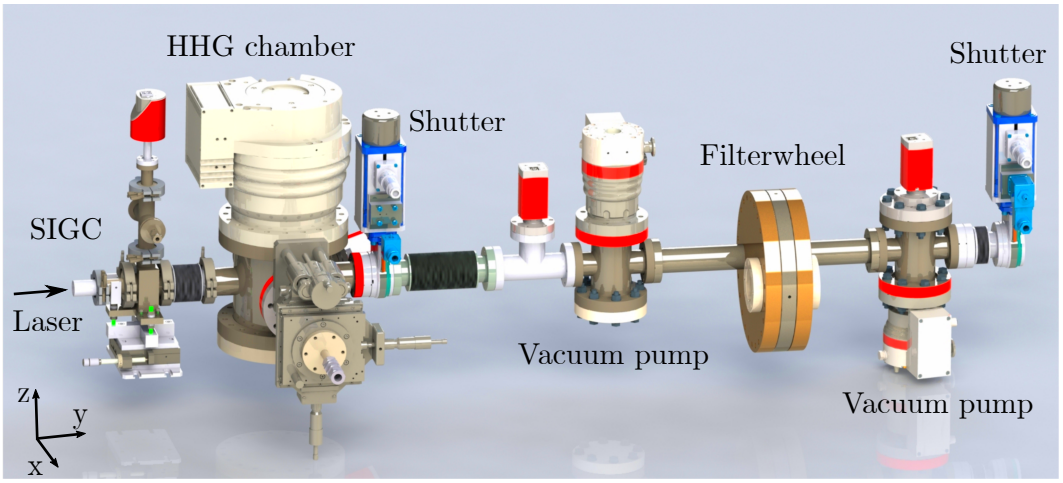

Figure 5.7: Design of the VUV source from [App+20]. The optical laser pulses are focused in a SIGC for the generation of VUV light. The produced radiation propagates in the beamline along the y-axis and through a double filterwheel, which can be used to select the spectral range of interest.

As mentioned in the previous Section, the ultrashort near-infrared pulses of the optical laser are focused by a telescope into the gas medium contained in the SIGC. The cell extends from a 1 mm thick fused silica input window to a 0.5 mm thick aluminum termination plate, for a total length of 30 cm. Since the focused beam is placed close to the termination plate, this long cell length ensures an intensity on the laser input window below the damage threshold. Noble gas can be inserted in the cell from a gas inlet and it can be pumped down by a rough vacuum pump, as shown in Fig. 5.8a. Connected to the vacuum pump side, a regulating valve (EVR 116, Pfeiffer) actively controls the gas pressure via a PID feedback. During operation, the valve keeps the

pressure oscillations in the gas cell <0.2 mbar. The termination plate is fixed to a 19 cm long tube (red tube in Fig. 5.8) in a configuration similar to the one described in Section 4.1. The infrared beam drills a <100 µm diameter hole in the plate, enabling the propagation of the VUV radiation along the beamline. When required the plate can be replaced or completely removed. To this end, it is necessary to isolate the HHG chamber from the rest of the vacuum beamline by means of a vacuum shutter installed directly after the chamber (see Fig. 5.7). With the shutter closed, the HHG chamber can be vented and opened for the removal or exchange of the termination plate. Usually, the same plate can be used for several days if no change in the laser focus position are made.

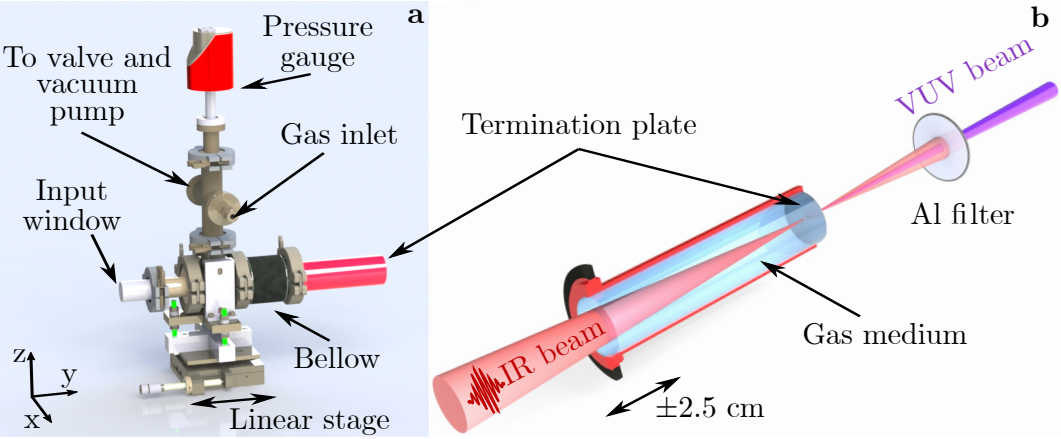

Figure 5.8: Implementation of the semi-infinite gas cell configuration. a) Detailed design of the installed SIGC. The vacuum system is placed on a linear translation stage. By moving the linear stage, the cell position is optimized with respect to the laser focus. b) Principle of the HHG source. The focused driving IR beam drills a hole in the termination plate allowing the propagation of the produced VUV light outside the cell under vacuum conditions. An aluminum filter can be used to suppress the remaining IR light.

By means of the small laser-drilled opening, the required pressure gradient between the inside of the cell and the rest of the beamline, i.e. the abrupt transition from hundreds of mbar to high vacuum, is maintained. The working principle of the VUV generation in the SIGC is sketched in Fig. 5.8b for clarity. The remaining infrared radiation can be blocked afterwards by means of filters. The entire gas cell system is inserted and connected to the HHG chamber by means of a bellow. With such configuration, the laser focus position is fixed at the HHG chamber center, keeping the previously fixed distance of 1.5 m between the VUV source point and the incoupling mirror (see Fig. 5.2). However, in

order to optimize the generation conditions for HHG in the gas medium, the cell can be moved with respect to the laser focus position by a manual linear translation stage (LT1, Thorlabs). The stage allows a movement along the beam propagation direction (y-axis) of ±2.5 cm that is accommodated by the bellow length.

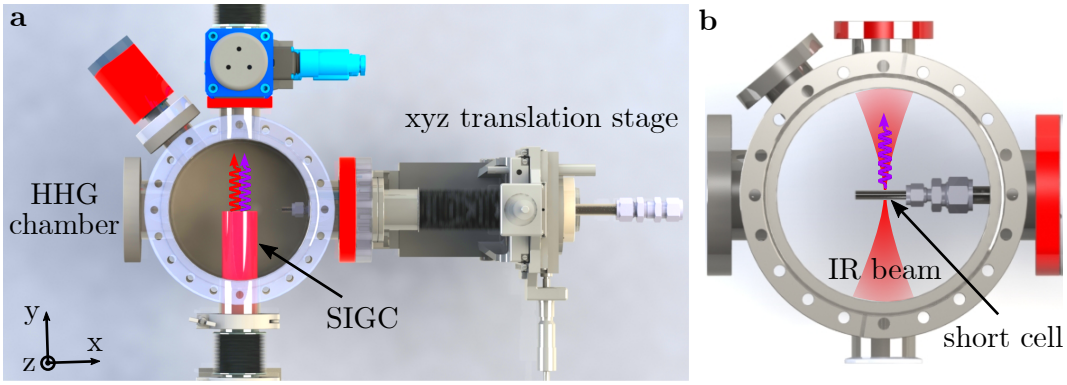

Figure 5.9: Top view of the HHG chamber. a) After the generation in the SIGC, the radiation propagates along the beamline towards the filterwheel. b) Alternative approaches to the SIGC, such as gas nozzle or a short gas cell, can be used for HHG. These configurations can be inserted in the beampath through a xyz translation stage on the chamber side.

While the SIGC is a robust and easy to implement configuration for HHG, the flexibility in readjustments of the laser alignment is very limited after the drilling on the termination plate. Moreover, depending on the focusing geometry and on the gas pressure required, the long gas volume could, in principle, lead to nonlinear propagation effects. For these reasons, alternative configurations can be used instead. By means of a xyz translation stage mounted on the side of the HHG chamber, see Fig. 5.9a, a gas nozzle or a short gas cell can be inserted in the beampath. Their position can be optimized with respect to the laser focus for an efficient HHG process. Note that, in this case, the red tube of the SIGC must be removed to not limit the movement of the new configuration. During commissioning of the VUV source, a 4 mm long gas cell, see Fig. 5.9b, was tested as possible generation configuration. However, this implementation suffers of a high gas load released in the vacuum chamber and requires a more sophisticated pumping system. More details on the comparison between the tests performed with the short gas cell and the SIGC are reported in chapter 6.

5.2.3 Filterwheel

After the generation process, the VUV radiation propagates in the beamline together with the remaining driving IR beam, which can be suppressed by means of filters. To this end, a rotatable double filterwheel, depicted in Fig. 5.10, allows to install filters of different thickness and materials. In order to block the IR light, a 0.1 µm thick aluminum filter with a supporting nickel mesh (5 µm thickness, 86% transmission, 36 µm pitch, Lebow Company) was used. Due to the edge around 70 nm in its transmission curve [HGD93], aluminum is a common choice to suppress IR radiation, leaving the harmonics of order ≥ 11 to propagate. Considering a filter transmission around 80% from 20 to 60 nm in addition to the mesh transmission, the VUV signal after the filter is reduced by about 31%.

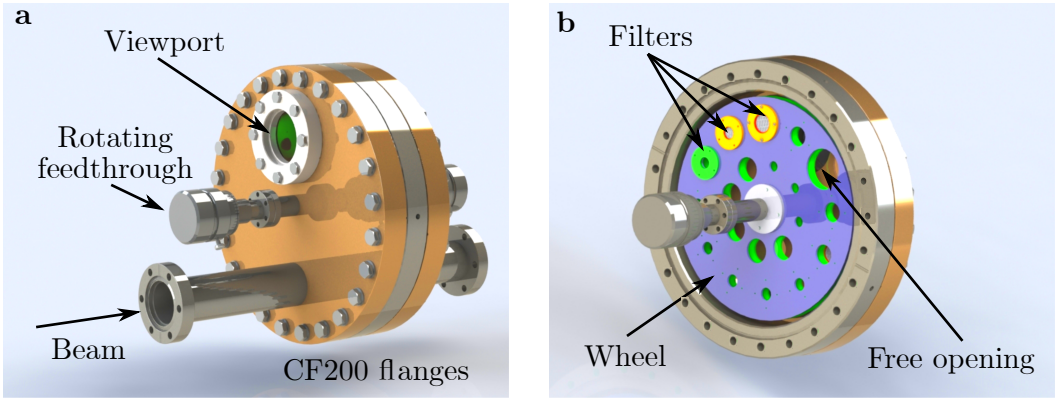

Figure 5.10: Filterwheel CAD drawing. a) The beam propagates from left to right through the selected filters. A CF50 viewport eases the installation and inspection of the filters in the wheel. b) Inner view of the design. On each wheel 11 openings for filters, plus one for the unfiltered propagation, are present. A second wheel (in light green) is behind the first one (in violet) with a mirrored design.

Filters can also be used to select a specific spectral window of interest in the VUV spectrum. The design includes two wheels that can be rotated independently to each other, allowing for combination of filters with different materials. Each wheel consists of a stainless steel disk with multiple openings, see Fig. 5.10b, connected to a manual rotating feedthrough. A total of 11 filters of different dimensions can be installed per wheel: 7 filters of 10 mm and 4 filter of 15 mm inner diameter. One opening is left free in both wheels to allow the propagation of unfiltered light. Fig. 5.11 depicts the transmission curves of the currently available filters at the VUV beamline.

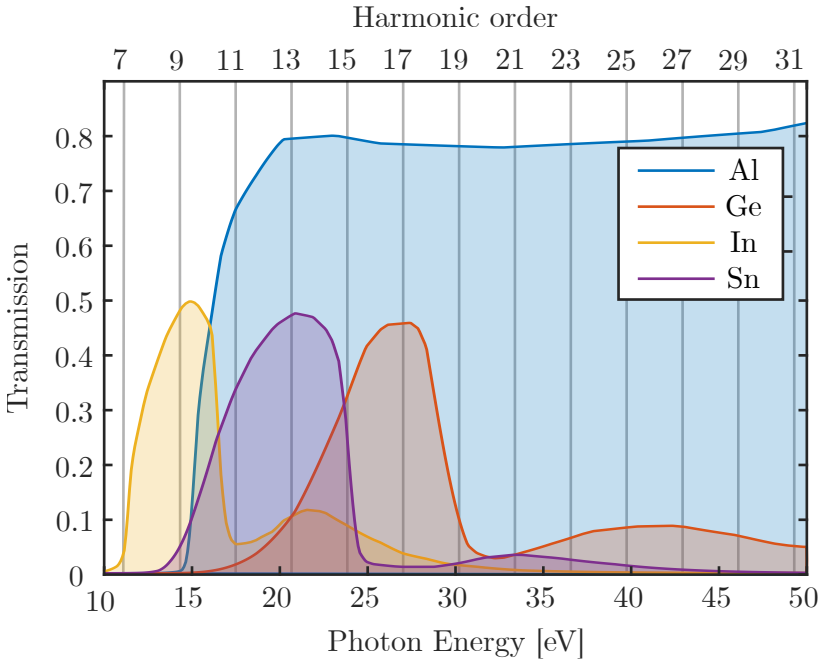

Figure 5.11: Transmission curves from [HGD93] of the available filters at the VUV beamline: 0.1 µm think aluminum, 0.15 µm thick germanium, 0.1 µm thick tin and 0.1 µm thick indium foil. No mesh is included in the reported transmission curve. The vertical lines indicate the photon energies corresponding to high-order harmonics of 780 nm.

5.2.4 Inline spectrometer

The harmonic spectrum can be characterized by means of a compact inline spectrometer installed behind the crossing point between the VUV and FEL beamlines. As shown in Fig. 5.12b, it consists of two vacuum cubes with multiple feedthroughs for a complete free-standing setup where each component can be moved independently with respect to the others. Inside the first vacuum cube, a photodiode (AXUV576, OptoDiode) is installed on a vertical feedthrough to measure the VUV pulse energy. The large detector active area (24 x 24 mm^2) ensures that the full divergent VUV beam is collected. Similarly to the setup described in Section 4.2, any remaining scattered infrared light is blocked by a 0.1 µm thick Al filter placed directly in front of the detector, as shown in Fig. 5.13a. The entire assembly can be moved in and out of the beampath thanks to the vertical feedthrough. The signal from the photodiode is then collected by a low-noise preamplifier (SR570, Stanford Research Systems) and can be read out by an oscilloscope (DPO 5204, Tektronix).

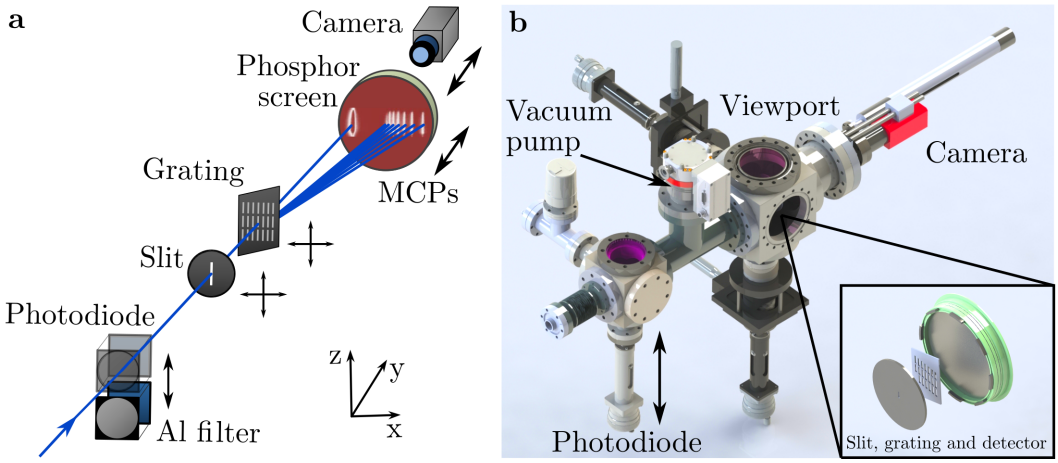

Figure 5.12: Schematic of the inline spectrometer. a) The spectral components of the VUV beam are spatially separated by a transmission grating and detected by a MCPs detector. A photodiode can be used for estimations of the VUV pulse energy. b) CAD drawing of the spectrometer. The inner components are installed in two vacuum cubes connected with a turbo vacuum pump. Figure from [App+20].

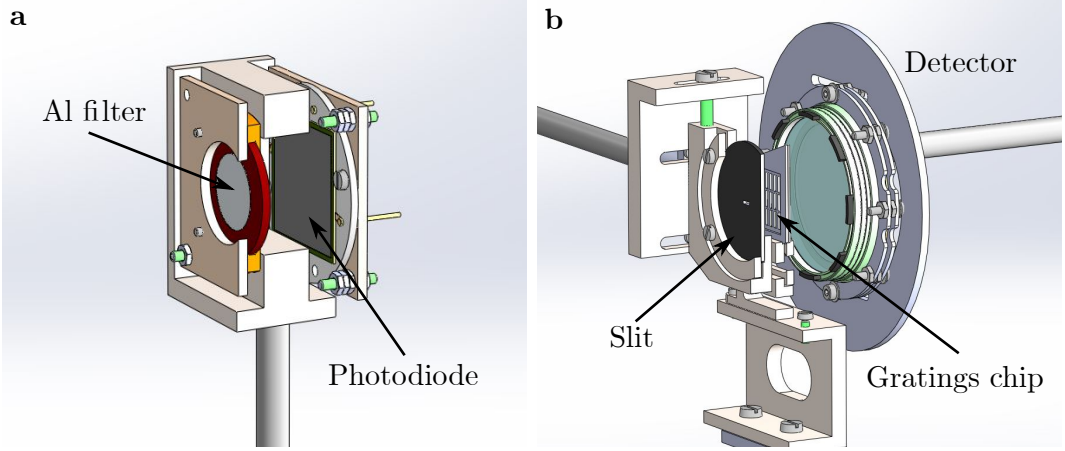

Figure 5.13: Inner parts of the inline spectrometer. a) CAD drawing of the photodiode holder. A 0.1 µm Al filter placed in front of the detector blocks any remaining infrared scattered light. b) Slit, transmission grating and MCPs detector are mounted on individual holders for complete flexibility in the alignment.

In the second vacuum cube, a transmission grating allows to spatially separate the spectral components of the VUV beam in a very compact geometry, suited to the limited working space of the experimental hall. The spectrometer makes use of a free standing chip with several transmission gratings of different periods from 500 to 10 000 lines/mm [Goh+15]. The complete $15 \times 15\,\mathrm{mm}^2$ chip consists of 3 lines and 7 columns, in which the single grating of $1.0 \times 4.0\,\mathrm{mm}^2$ are arranged, see Fig. 5.14. A slit of $0.8 \times 3.8\,\mathrm{mm}^2$ is placed in front of the grating of interest, in order to avoid illumination of multiple gratings. By means of a combination of linear feedthroughs and 2D translation stages, the slit and the chip can be aligned, independently from each other, with respect to the VUV beam position. The spectral components, spatially separated by the grating, are detected by a double microchannel plate (MCP) system combined with a phosphor screen (DD 2561 ZV, Proxivision). The image of the screen is then recorded by a camera (acA2040–25gm, Basler) placed outside the vacuum system. The distance between the grating chip and the detector can be optimized in a range from 1 to 15 cm, depending on the required acceptance angle.

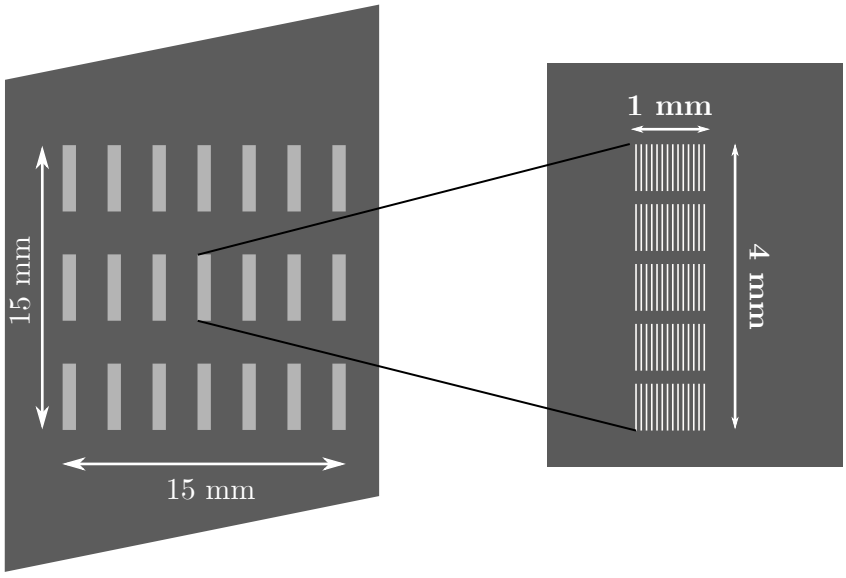

Figure 5.14: Schematic of the free standing chip with transmission gratings of different periods. A single grating is $1.0 \times 4.0\,\mathrm{mm}^2$ and can be selected by means of a slit. A complete description and characterization of a similar chip can be found in [Goh+15].

5.2.5 Incoupling mirror

As already mentioned, in order to couple the VUV beam into the FEL beamline, a mirror can be inserted on the beampath in the incoupling chamber, see Fig. 5.15a. The vacuum chamber, provided by FMB-Berlin GmbH, has 4 arms, two of which are connected to the VUV beamline and two to the FEL beamline. In each arm, a vacuum shutter is installed in order to allow for a complete isolation of the chamber. On the side, a camera observes the mirror's surface through a viewport.

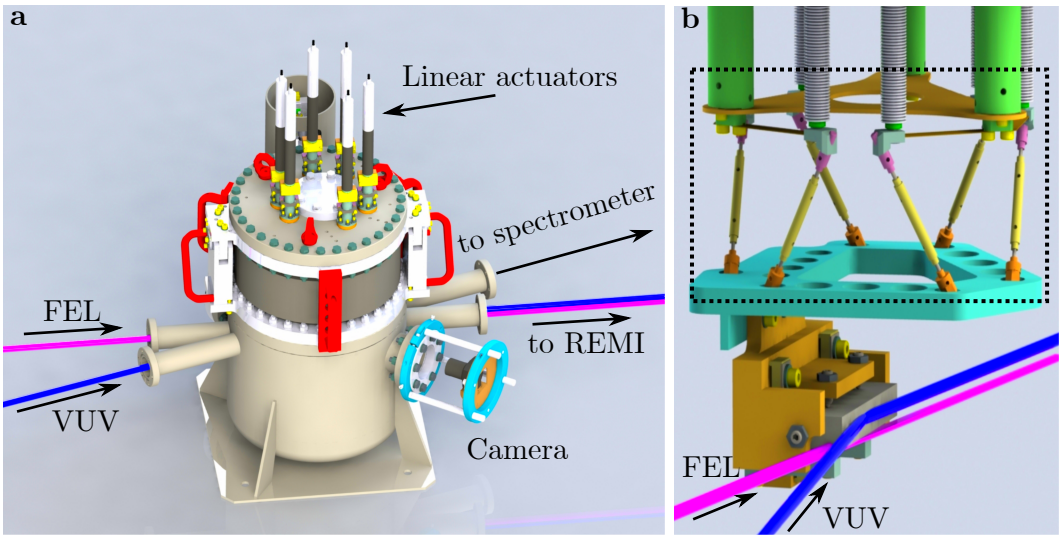

Figure 5.15: Incoupling chamber CAD drawing adapted from [App+20]. a) The chamber is placed at the intersection point between the FL26 and VUV beamline. b) Inner structure in the chamber. The mirror's position is controlled by a hexapod kinematics structure (highlight by the dashed box).

The mirror's holder is directly fixed to a hexapod kinematics structure which provides control of all the six position degrees of freedom. The structure is connected to 6 linear actuators placed on the chamber top flange and it is controlled by a LabView program. A similar design is used for all the optics at FL26 [Sch+19c]. More details on the kinematics structure can be found in Noll *et al.* [Nol+09]. In order to move the mirror out of the beampath, the top flange of the chamber sits on a bellow which is mechanically tilted of 6° (maximum roll possible 8°) by a linear actuator (LGA421S14-B-TJBA-038, Nanotec) with maximum load ∼50 kg. In this configuration, as shown in Fig. 5.16, the VUV beam reaches the inline spectrometer, otherwise it is reflected by the mirror. The tilt mechanism allows to move the mirror without changing its position

with respect to the hexapod kinematics structure and the chamber top flange. The hexapod mechanism is designed for an accurate alignment of the mirror in the beamline, but it does not support a long vertical movement. In order to completely unblock the VUV beam, the mirror and its mount should be lifted by ∼28 mm, while the hexapod vertical movement is limited to 5 mm by the springs which connect the structure to the linear actuators. Moreover, by tilting the top flange, the total incoupling chamber volume remains constant allowing to cancel out any force due to the pressure difference between the inside and outside of the chamber. In comparison, a vertical movement of the whole structure would lead to a load of more than 500 kg plus the weight of the actual components and the bellow forces. The reproducibility of the bellow position from out-position to in-position is sufficiently high that only minor movements of the VUV focus into REMI has been observed (displacement ≪ 20 µm), which can be easily compensated using the hexapod mechanism.

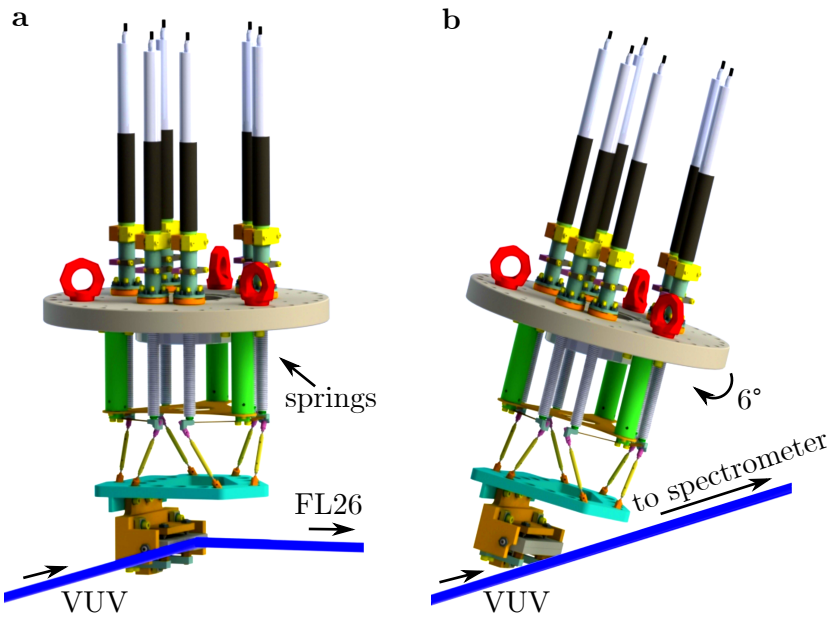

Figure 5.16: Schematic of the tilt mechanism. a) The mirror couples the VUV beam into the FL26 beamline. b) A 6° tilt of the chamber top flange allows to move the mirror out of the beampath and access the inline spectrometer.

For the incoupling is used an off-axis hyperboloidal mirror, designed by OptiXfab GmbH, with a rectangular shape of 100 × 15 mm^2. The entrance and exit arms are equal to 1500 mm and 3000 mm respectively. A 30 nm (±5%) carbon coating layer ensures a reflectivity close to 80% at a grazing angle of 8° for photon energies from <30 to 120 eV [HGD93], as shown in Fig. 5.17.

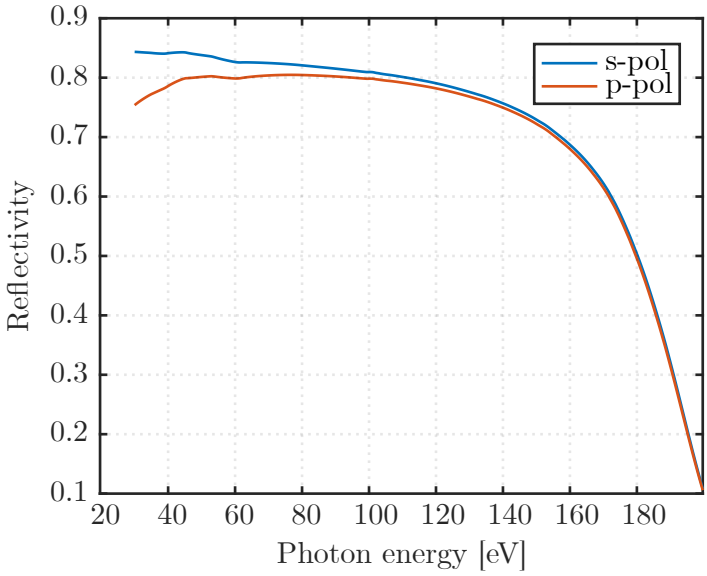

Figure 5.17: Calculated reflectivity of 30 nm of C coating on Si substrate. Grazing angle 8°. Data from [HGD93].

In order to reflect the VUV radiation without blocking completely the FEL beam, a vertical shift of 7.5 mm (half of the mirror height) is set between the two beamlines. While the VUV beam is fully reflected on the mirror surface, the FEL beam is partially blocked by the mirror bottom edge. The truncated area depends on the FEL alignment. Due to this vertical shift, the two beams reach different halves of the split-and-delay unit, which can therefore be used to control their relative delay (max delay ±1500 fs), before being focused by the ellipsoidal mirror spatially overlapped in REMI as sketched in Fig. 5.18.

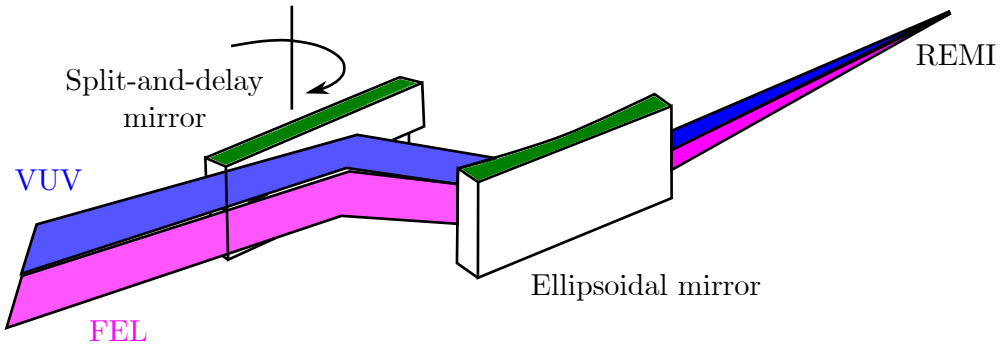

Figure 5.18: Scheme of the pump-probe configuration at FL26. A vertical shift between the VUV and FEL beam allows for control of their relative delay in REMI.

Imaging of VUV beam. The specifications of the incoupling mirror were chosen in order to ensure the spatial overlap between the VUV and FEL beam into REMI. The geometrical beampaths in the optical setup are sketched in Fig. 5.19. The FEL beam propagates from the source point S1 to the split-and delay unit and it is reflected on the ellipsoidal mirror M2. Between these two point there is a distance of around 85 m. However, in the figure the point source S1 is placed much closer to the optical setup for clarity, so the figure is not to scale. Due to the reflection from the split-and-delay unit, in the reference frame of the ellipsoidal mirror the FEL beam source coincides with the virtual point S', which corresponds to one of the foci of the ellipsoidal curve. The virtual image of the FEL beam in S' is therefore transfered in a real image in the second ellipsoidal focus F, placed at the interaction point into REMI.

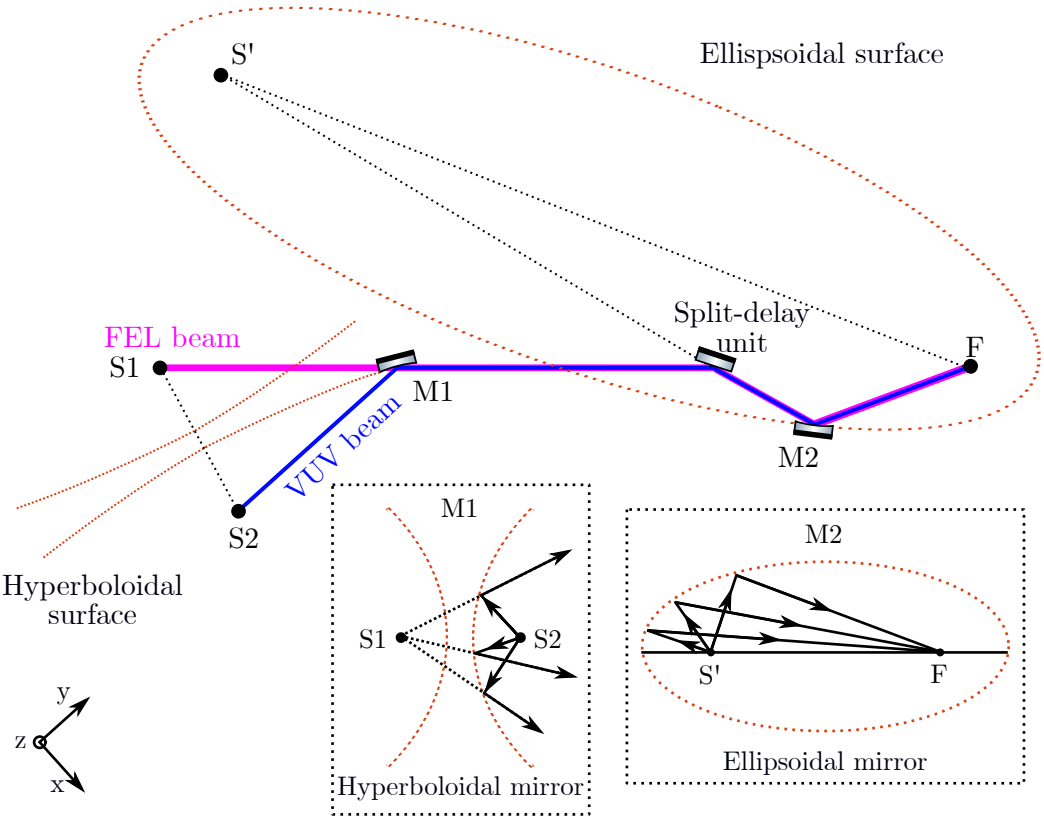

Figure 5.19: Sketch of the geometrical beampaths for the imaging of the FEL and VUV beam. Top view, not to scale. The hyperboloidal mirror (M1) allows for a virtual image of the VUV source (S2) coincident with the real FEL source (S1). The ellipsoidal mirror (M2) focuses both sources spatially overlapped in the REMI interaction point (F).

The VUV beam starts propagating from the source point S2. In order to be focused spatially overlapped with the FEL beam in the position F, the source points of the two beams in the reference frame of the ellipsoidal mirror must coincide. To this end, the incoupling mirror surface is a hyperboloid with foci S1 and S2. The mirror allows then for a virtual image of the VUV source point S2 in the position S1, as shown in the figure. Due to the reflection on the split-and-delay unit, in the reference frame of the ellipsoidal mirror the VUV source point also coincides with S'. The spatial overlap in F is therefore ensured. Starting with this geometric design, the company OptiXfab GmbH performed ray tracing simulations of the entire VUV propagation in the beamline taking in account the finite dimension, divergence and spectral range of the two sources. The final VUV focus in F depends on the real source size and the magnification of the optical system composed by hyperboloidal plus ellipsoidal mirror. The total magnification is not constant with respect to the source size. By considering a divergence of around 1 mrad, calculated for harmonic order 11 from the divergence of the focused driving laser, the simulated VUV spot diameter in the REMI focus results equal to 33 µm for a 50 µm source diameter and 70 µm for a 100 µm source diameter.

5.2.6 Differential pumping system

In order to ensure in the REMI chamber an operation pressure in the range of 10^{-11} mbar, several differential pumping stages are implemented in the FEL beamline [Sch+19c]. However, during operation of the HHG source, the pressure in the SIGC can vary, depending on the generation requirements, between a few mbar and a few hundreds of mbar. The connection of these two different pressure regimes is a critical aspect of the VUV beamline design. Sufficient differential pumping stages needed to be included in the 1.5 m distance that separates the HHG source from the incoupling chamber, where the pressure is required to be $<10^{-7}$ mbar. In case this limit is exceed, the vacuum shutters in FL26 would automatically closed as safety measure preventing the operation of the beamline. Therefore, in this limited space the pressure must drop by several orders of magnitude. To this end, the VUV beamline is divided in 5 parts, as shown in Fig. 5.20, with different pressure regimes: SIGC, HHG chamber, upstream and downstream sections of the filterwheel, and incoupling chamber.

Two tubes of small inner diameter have been included in the design in

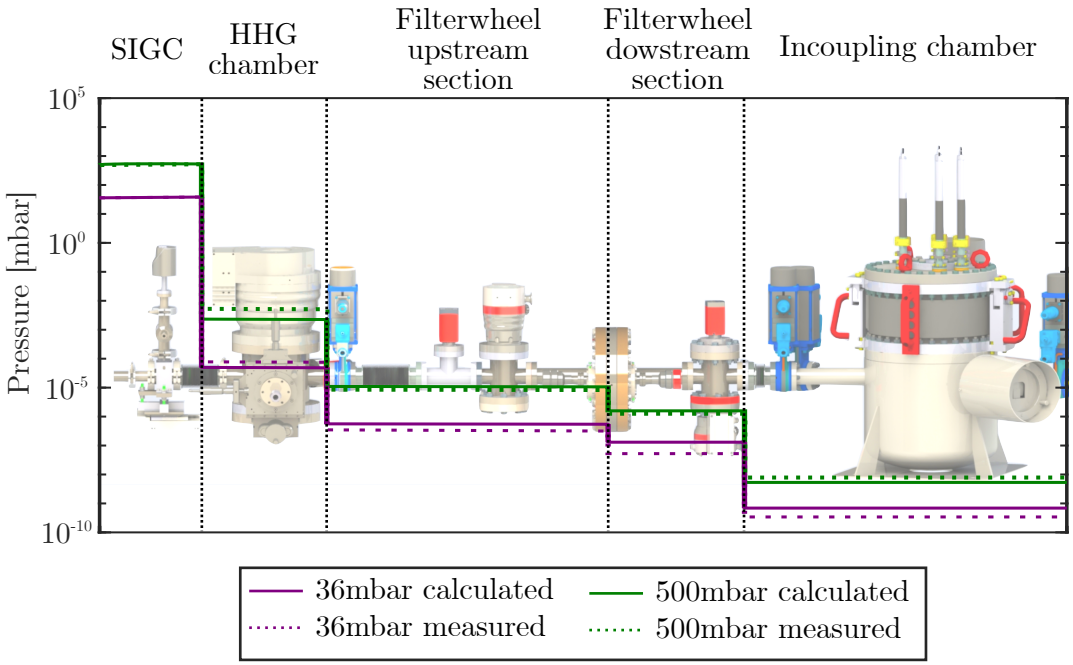

Figure 5.20: Overview of the pressure in the VUV beamline up to the crossing point with the FL26. Calculated (continuous lines) and measured values (dashed lines) for different reservoir argon pressures in the SIGC.

order to reduce the conductivity of the pipe connecting different parts of the beamline and help to keep a large pressure gradient. The dimensions of these differential pumping tubes must allow for the propagation of the VUV beam. A basic description of the gas flow along the beamline, presented in the following, can be used to calculate the expected pressure in each section and to chose the necessary pumping specification.

Gas flow from the termination plate. As already mentioned, the laser-drilled hole in the SIGC termination plate acts as a first differential pumping stage, allowing the propagation of the beam while keeping a substantial pressure gradient between the inside and outside of the gas cell. The average pressure $\bar{P}$ in the HHG chamber depends then on the gas volume flow rate g_{pV} [mbar $\cdot$ L/s] that escapes through the plate. The system is not substantially different from a free-jet (or nozzle) source where a high-pressure gas flow expands into a low-pressure volume. The dynamic can be very well described following the free-jet expansion proposed by Miller in "Free Jet Sources" [Mil88]. For an ideal continuum isentropic flow, neglecting viscous and heat conduction effects (high-speed flow approximation), the mean velocity v_g and the density ρ_g of the expanding gas can be written as a function of the gas proprieties:

$$v_g = M\sqrt{\frac{\gamma R T_0}{W}}\left(1+\frac{\gamma-1}{2}M^2\right)^{-1/2}, \tag{5.1}$$

$$\rho_g = \rho_0\left(1+\frac{\gamma-1}{2}M^2\right)^{-1/(\gamma-1)}, \tag{5.2}$$

where M is the Mach number (ratio of the flow velocity to the speed of sound), $\gamma = 5/3$ the adiabatic index for noble gases, W the gas molar mass, R the ideal gas constant, T_0 and ρ_0 the reservoir temperature and density respectively. For a complete derivation of equations 5.1 and 5.2 please refer to [Mil88]. At the source exit, which corresponds to the opening on the SIGC plate, the gas expansion can be approximated to a quasi one-dimensional flow. From the conservation of the mass follows that the mass flow rate $\dot{m} = \rho v A^*$ (expressed in [g/s]) through the area of the plate opening A^* is constant in time. By combining equations 5.1 and 5.2, $\dot{m}$ can be written as:

$$\dot{m} = \rho v A^* = P_0 A^* \left[\frac{\gamma W}{R T_0}\left(\frac{2}{\gamma+1}\right)^{(\gamma+1)/(\gamma-1)}\right]^{1/2}, \tag{5.3}$$

where the Mach number M is equal to 1 and P_0 indicates the reservoir pressure

in the gas cell. Taking in consideration the general gas equation, the gas flow rate through the plate opening is therefore given by:

$$g_{pV} = \dot{m}\frac{RT_0}{W} = P_0 A^* \left[\frac{\gamma RT_0}{W}\left(\frac{2}{\gamma+1}\right)^{(\gamma+1)/(\gamma-1)}\right]^{1/2} \tag{5.4}$$

and it is expressed in [mbar · L/s]. The average pressure $\bar{P}$ in the HHG chamber depends then on the gas flow rate g_{pV} divided by the effective pumping speed of the turbo pump used in the HHG chamber.

This estimation allows to choose the best turbo pump speed in order to eliminate most of the gas in this first pumping stage. In the VUV beamline design, a HiPace700 (Pfeiffer Vacuum GmbH) was chosen, with a maximum pumping speed around 670 L/s for argon, reaching pressures more than 5 orders of magnitude lower than inside the gas cell.

Gas flow in the beamline. As long as the pressure in the HHG chamber is $\ll 10^{-2}$ mbar (Knudsen number $k_n > 0.5$), the molecular flow regime applies for all the other differential pumping sections along the beamline. In this regime, the gas flow rate g_{pV} depends on the vacuum conductance C (expressed in L/s) of the beamline pipes:

$$g_{pV} = C \cdot (P_{in} - P_{out}), \tag{5.5}$$

where P_{in} and P_{out} are the pressures before and after the pipe, respectively. For long round pipes, the conductance is determined by the pipe length l and inner diameter d:

$$C = \pi\bar{v}\frac{d^3}{12 \cdot l}, \tag{5.6}$$

where $\bar{v}$ is the mean thermal velocity of the gas. Once more, the final average pressure after the differential pumping stage can be calculated dividing the gas flow rate g_{pV} by the pumping speed of the used pump S_{pump}:

$$P_{out} = \frac{g_{pV}}{S_{\text{pump}}} = \frac{C \cdot P_{in}}{S_{\text{pump}} + C}. \tag{5.7}$$

This approach can then be used to calculate the average pressure in all the remaining beamline parts by considering the conductance of the pipes connecting each section with the previous one.

- The filterwheel upstream section is separated from the HHG chamber by a 5 cm steel tube welded on a double-sided blind flange (see inset in Fig. 5.20) with an inner diameter 4 mm placed after the HHG chamber.
- The filterwheel itself can be considered as differential pumping tube: the difference in diameter between the filterwheel flanges (200 mm) and the beamline pipes (40 mm) leads to a change of the pipe conductance. Gas molecules are therefore trapped in the larger volume of the filterwheel and do not reach the upstream beamline sections.
- A second differential pumping tube separates the filterwheel downstream section from the incoupling chamber. In this position, an inner diameter of 10 mm and a tube length of 8 cm ensures that the full VUV beam can pass through the pipe. Due to the considerable volume of the incoupling chamber, in the calculation of the average pressure a correction for outgassing has been included (1.2×10^{-12} mbar $\cdot$ l/s/cm^2 from [Gmb16], after baking for 2 days at 120°). This contribution is added at the total gas flow rate g_{pV} in equation 5.7. An additional tube of 20 mm inner diameter and 5 cm total length is placed at the entrance of the inline spectrometer assembly to further isolate the incoupling chamber.

Fig. 5.20 shows the calculated pressures in all sections for 36 mbar and 500 mbar of argon pressure in the SIGC. The dashed lines indicate the respective measured values, which are in good agreement with the calculated ones. For both reservoir pressures considered, an operation pressure $<10^{-7}$ mbar can be ensured in the incoupling chamber. While the exact pressure value is not the goal of these calculations, they provided a very useful tool during the design phase. A more detailed overview of the final operation pressure in the VUV beamline is depicted in Fig. 5.21. The reservoir pressure in the SIGC is increased up to 700 mbar of argon, while the average pressure of each different beamline sections is observed. Higher values of the reservoir pressure caused a deceleration of the HiPace700 turbo pump speed in the HHG chamber, limiting the pressure range usable. In the range tested, the pressure at the incoupling chamber (green dots in the figure) is constantly much lower than the required limit of 10^{-7} mbar. Moreover, the gas load due to the HHG source is severely reduced through the VUV beamline, as expected, leading to an almost constant measured pressure at the inline spectrometer position (light blue dots).

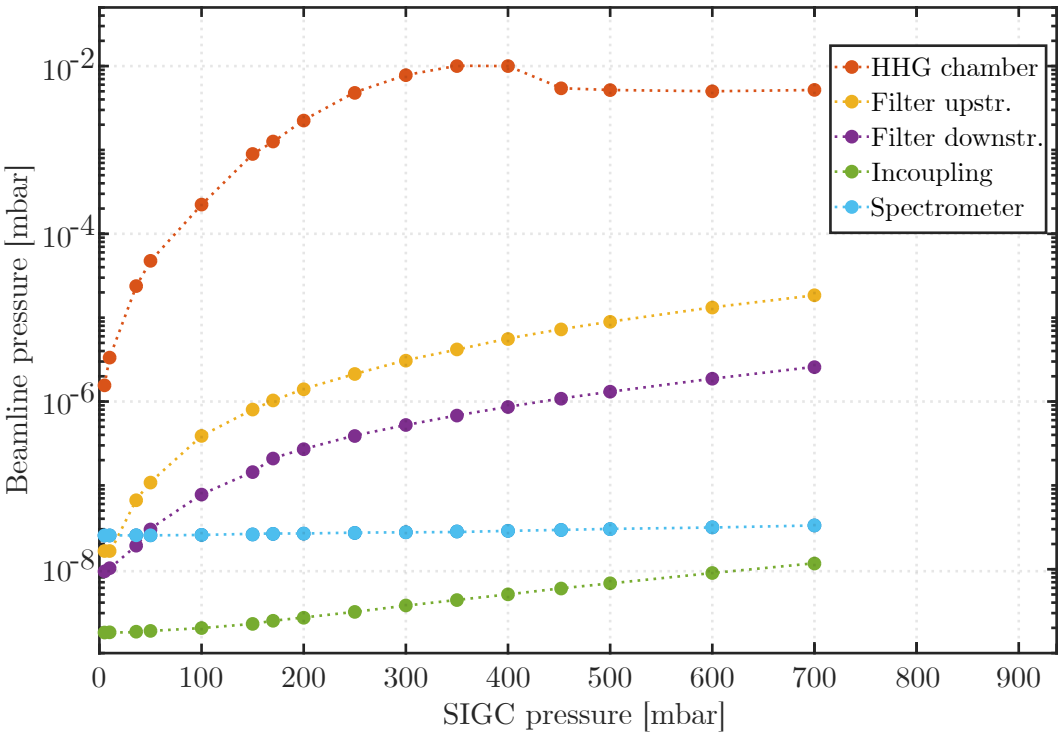

Figure 5.21: Measured pressure in the different VUV beamline sections as a function of the argon pressure in the SIGC. For more than 700 mbar of argon in the SIGC, the first turbo pump, HiPace700, on top of the HHG chamber starts decelerating its speed. In the range considered, the pressure at the intersection point with the FEL beamline (incoupling) is constantly lower than the required limit of 10^{-7} mbar.

Chapter 6

Beamline performance

Between May 2019 and July 2020, four beamtimes with the FLASH2 optical laser have been performed for the commissioning of the VUV source. The main results are summarized in Appi *et al.* [App+20] and are presented in this chapter, including: the generation of high order harmonics (see Section 6.1), the incoupling and focusing of the VUV radiation in the FEL beamline (see Section 6.2), and first photo-ionization tests in argon making use of the reaction microscope (see Section 6.3).

6.1 VUV generation

The first achievement of the VUV source commissioning was the generation of high order harmonics driven by the FLASH2 optical laser beam. The laser and, due to the coherence of the HHG process, also the VUV beam match the burst mode of the FEL beam with an intra-burst repetition rate of 100 kHz. The high intra-burst repetition rate supports an appropriate events rate for coincidence measurements in REMI, but it also limits the laser average pulse energy available. This aspect strongly influences the HHG process conditions. Therefore, the focusing system must be optimized to achieve intensities of $\sim 10^{14}\,\mathrm{W/cm^2}$ in the HHG chamber. Tab. 6.1 shows the laser parameters for two different focusing systems used during commissioning of the VUV source.

In the three beamtimes performed in 2019, pulse energies up to 225 µJ

Table 6.1: Overview of the laser parameters for two different focusing systems used during testing of the new VUV source. The system A was used in May, August and November 2019, while the system B in July 2020. The maximum pulse energy is measured before the focusing optics.

System	Max pulse energy	Pulse duration	Focus diameter
A	225 µJ	15 fs	72 µm
B	210 µJ	<20 fs	50 µm

were focused making use of a telescope (system A) with a defocusing mirror of −500 mm focal length and a focusing mirror of 300 mm, separated by 165 mm distance. With this configuration, the laser focus of 72 µm diameter was placed 56 cm from the last mirror, which corresponds approximately to the center of the HHG chamber. The estimated laser intensity at the beam waist ($1/e^2$) is $\sim 9.5{\cdot}10^{13}\,\mathrm{W/cm^2}$. In order to increase the laser intensity, a new focusing system (B) was installed in July 2020, which includes two separated telescopes as described in Section 5.2.1. In this case a 50 µm diameter focus size was achieved, while keeping the focus position equivalent to the one from the previous configuration. The lower pulse energy available and the slightly longer pulse duration achieved, led to an estimated laser intensity at the beam waist of $\sim 1.4{\cdot}10^{14}\,\mathrm{W/cm^2}$. However, this second configuration should allow for a smaller focus size down to 35 µm diameter, which would correspond to an intensity of $2.8{\cdot}10^{14}\,\mathrm{W/cm^2}$. The discrepancy between the measured focus size and the expected one, suggests the presence of an unknown perturbation source, which affects the beam quality preventing to reach a tighter focus. Further investigations are necessary in order to correct this discrepancy and achieve higher laser intensity.

After generation, the beam propagates up to the inline spectrometer where the radiation is characterized by resolving the spectral components and measuring the average pulse energy, as described in the following.

6.1.1 Spectral components

The grating chip available in the inline spectrometer (see Section 5.2.4) allows to used several grating periods and, therefore, to access different levels of resolutions. By aligning one grating to the slit position, the rest of the chip is covered and only the preferred grating is illuminated by the VUV beam. The

distance from the grating to the MCPs detector can be adjusted depending on the grating period and the spectral range of interest. Fig. 6.1 shows a typical spectrum of the harmonics generated in the SIGC. In this case, the spectrum is resolved using a 1850 lines/mm grating, with a grating-detector distance of 9.5 cm. On the detector the zero diffraction order (the bright line on the left side of Fig. 6.1) is visible, as well as the first diffraction order (on the right side). In the first diffraction order, the different spectral components are spatially separated. From left to right, the harmonic wavelength increases while the relative intensities of the spectral lines is denoted by their brightness.

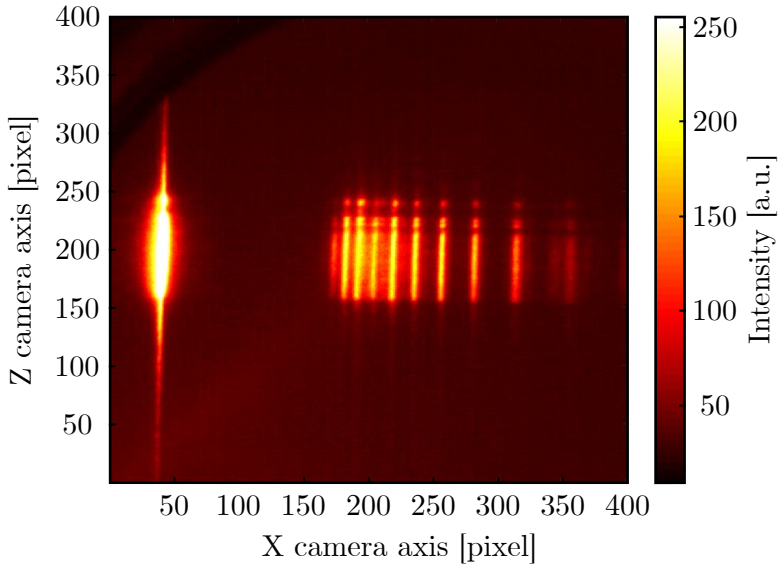

Figure 6.1: Typical image on the spectrometer camera of the resolved VUV spectrum. The bright line, on the left, corresponds to the grating zero order of diffraction, while the first order is visible on the right. The harmonic wavelength increases from left to right.

By integrating the signal along the z-axis, an one dimensional representation of the spectrum is obtained. The x-axis can then be converted in wavelength by taking in account the grating equation:

$$m\lambda_x = d \sin\left(\arctan\frac{X - x_0}{l}\right), \tag{6.1}$$

where m indicates the diffraction order, λ_x the wavelength calibrated axis of the spectrum, d the grating period, X the non-calibrated spectrum axis in pixel, x_0 the position in pixel of the zero order of diffraction and l the distance grating-detector expressed in pixels. The value of x_0 can be determined directly

by the image on the spectrometer camera. The distance grating-detector, however, can be measured and then converted in pixels or can be estimated directly from the experimental data. In the last case, it is necessary to measure the position on the camera of two peaks x_1 and x_2. By assuming that these peaks are harmonic orders of the driving wavelength, the expected wavelengths λ_1 and λ_2 can be expressed using equation 6.1:

$$m\lambda_i = d \sin\left(\arctan\frac{x_i}{l}\right), \tag{6.2}$$

with $i = 1, 2$. From equation 6.2, the term l can be explicated and rewritten as:

$$l = \frac{x_2 - x_1}{\tan\left[\arcsin\left(\frac{m}{d}\lambda_2\right)\right] - \tan\left[\arcsin\left(\frac{m}{d}\lambda_1\right)\right]}, \tag{6.3}$$

which is directly expressed in pixels. While the direct measurement of the grating-detector distance seems to be more straightforward, the second indirect estimation does not rely on the precision of the manual measurement.

The wavelength calibration can be tested making use of an aluminum filter in the beampath. The filter blocks the propagation of any remaining fundamental IR radiation, as well as the orders below the 11^{th} harmonic (see Fig. 5.11). By comparing the spectrum with and without the filter's attenuation is then possible to identify the orders 9^{th} and 7^{th}, which are suppressed by the filter.

Following this procedure, the calibrated harmonic spectrum is obtained. Fig. 6.2 shown typical resulting spectra for different generation gas media in the SIGC. The dotted lines indicate the spectrum after the insertion of a 0.1 µm thick aluminum filter in the beampath. All plots are in agreement with the wavelength calibration. In the data reported, a minimum VUV wavelength of 31 nm, corresponding to the 25^{th} harmonic order, has been observed with a pressure of 21 mbar in argon. In this case, the VUV spectrum extends from 10 to 40 eV which was the initial target range of the source. As expected, in the case of xenon as generation medium, the cutoff is placed at longer wavelength since the ionization potential (12.13 eV) is smaller than for argon (15.76 eV) or krypton (14 eV). For this reason only harmonics up to order 19^{th} are generated in 10 mbar xenon, while a broader spectrum is observed both in krypton and argon. In all spectra are also present secondary peaks around the 7^{th} order. These peaks are contributions of the grating second order of diffraction which is not completely suppressed.

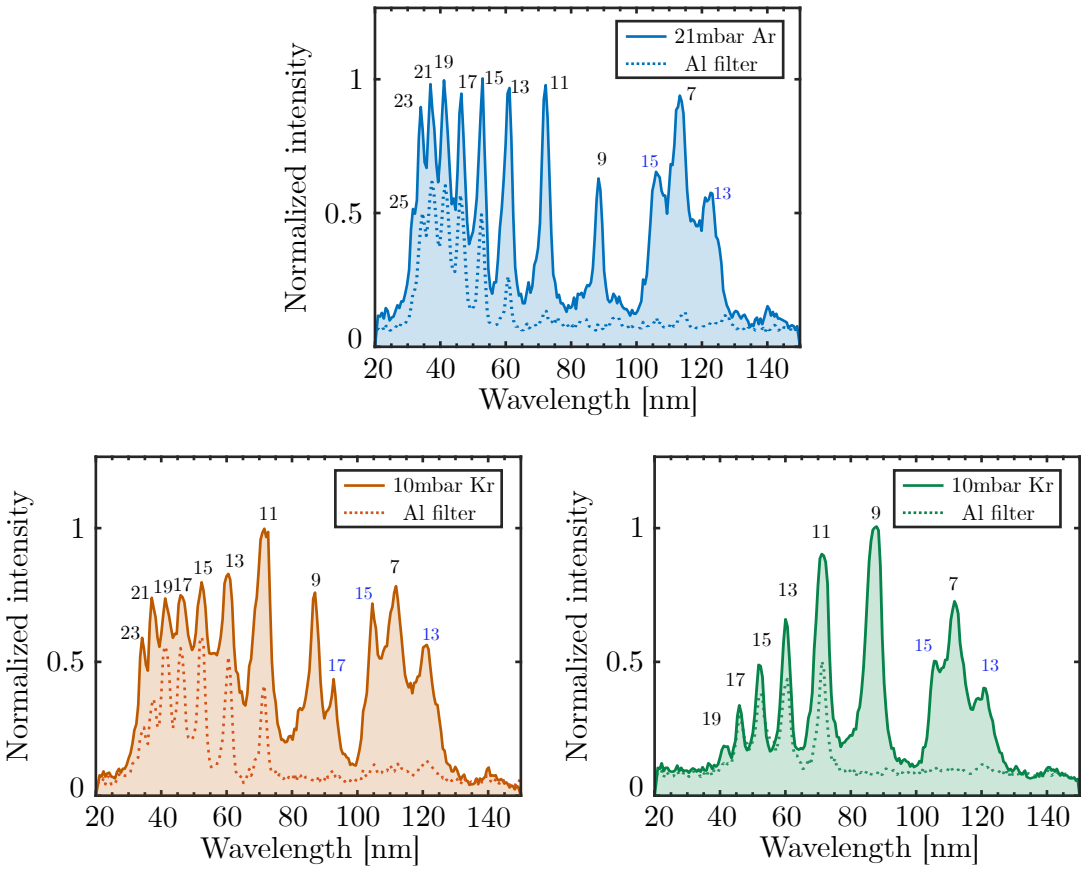

Figure 6.2: Harmonic spectra generated in different gas media with a SIGC configuration (May 2019, focusing system A). For 21 mbar of argon as generation medium, the VUV spectrum extends from 10 to 40 eV. The dotted line indicates the spectra measured after the insertion of a 0.1 µm thick aluminum filter in the beampath for the suppression of the fundamental IR radiation.

Short gas cell test. In the beamtime of July 2020, a test of an alternative configuration for HHG has been performed with a 4 mm long gas cell. The main advantage of a short cell configuration is the limited propagation in the gas medium. Unlike the SIGC, even for very high gas pressure, the reabsorption inside the cell is strongly suppressed since the gas medium is confined only in a small volume around the laser focus. This configuration is particularly suited for efficient HHG in tight focusing geometries provided that the gas cell length is shorter than the Raylength length of the laser focus [Hey+12].

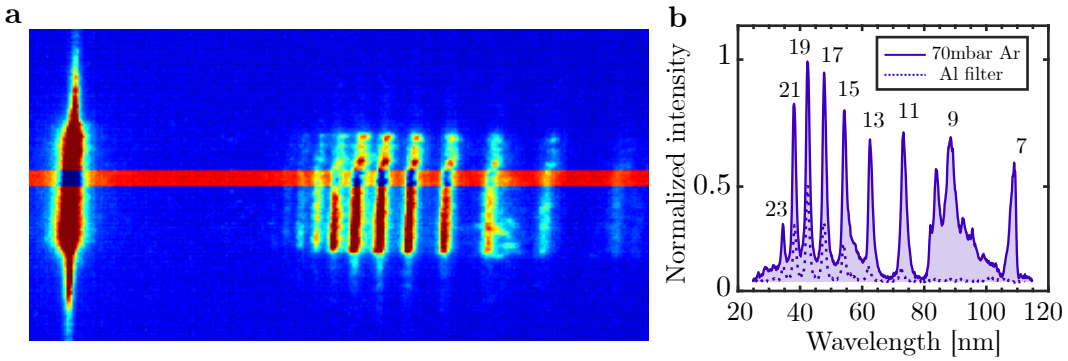

Figure 6.3: VUV spectrum generated with a 4 mm long gas cell. a) Image recorded by the spectrometer camera. The horizontal red line indicates a region of interest (ROI) on the camera. b) Calibrated spectrum with (dashed line) and without (full line) the insertion of a 0.1 µm thick Al filter in the beampath.

The gas cell is placed at the HHG chamber center using the side xyz translation stage (see Fig. 5.9 in Section 5.2.2), which allows for optimization of the cell position respect to the laser focus in all the directions. The gas inlet is connected to a 1/2 inch stainless steel tube inserted thorough the xyz stage. The IR focus enters the cell through a 200 µm pre-drilled hole, while the exit hole is drilled by the laser itself. Fig. 6.3 shows the VUV spectrum obtained in 70 mbar of argon. Harmonics up to order 23$^{\text{rd}}$ are clearly visible in the spectrum. However, the pressure in the beamline increases substantially during operation due to the double opening in the cell, one for the laser input and one for the output. During the performed test, a maximum argon pressure of 160 mbar in the cell was reached, which corresponds to a pressure of 8×10^{-3} mbar in the HHG chamber. Higher pressure values would lead to a deceleration of the HHG chamber turbo pump's speed with consequential shutdown. Therefore, for a stable operation, a different vacuum system is required. The system should ideally allow for pumping of the main gas load in proximity of the cell opening minimizing the effect on the HHG chamber average pressure.

6.1.2 VUV pulse energy

For a complete characterization of the VUV source, it is important to measure the generated VUV pulse energy. This information can be estimated from the signal of the XUV photodiode installed in the inline spectrometer (see Section 5.2.4). The signal from the detector is amplified by a low-noise preamplifier and then read out with an oscilloscope triggered to resolve a single laser burst.

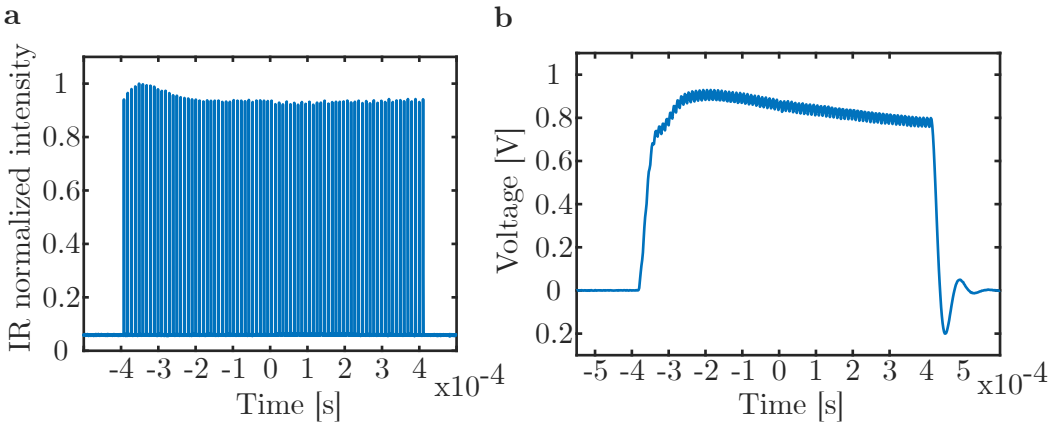

Figure 6.4: Comparison between the burst structure of the IR radiation (a) measured directly at the laser output and the harmonic photodiode trace (b) measured in the in-line spectrometer of the VUV beamline. Figure readapted from [App+20].

Fig. 6.4 shows a comparison between the IR burst pattern (a) measured directly at the laser output and a typical VUV photodiode trace (b) at the inline spectrometer. Even though the sensitivity of the pre-amplifier in the beamline is not optimized to resolve the temporal structure of the VUV signal, the 80 pulses of the burst are visible. The difference between the IR laser envelope shape and the slow modulation of the VUV signal can be attributed to the different electronic settings and the nonlinearity of the HHG process.

By considering the pre-amplification factor and the diode response, the VUV pulse energy can be calculated from the time integral of the photodiode trace $S(t)$. Called n_p the number of pulses in one trace ($n_p = 80$ in this case) and "sens" the preamplifier sensitivity [expressed in A/V], the charge Q_{pulse} produced by the detector is given by:

$$Q_{\text{pulse}} = \frac{1}{n_p} \cdot \text{sens} \cdot \int_{t_0}^{t_1} S(t)\, dt. \tag{6.4}$$

The VUV pulse energy E_{pulse} is connected to the charge Q_{pulse} through the responsivity of the photodiode, which indicates the response curve of the

detector as a function of the wavelength of the incident light. The responsivity resp(λ) is then expressed in [A/W] and can be obtained from the photodiode data sheet. Since the responsivity is a function of the wavelength λ of the detected radiation, the full harmonic spectrum has to be recorded and resolved, in order to estimate its pulse energy.

The VUV pulse energy can be approximated as sum of single harmonic order q contributions, if their relative weight $R(\lambda_q) \leq 1$ is known:

$$E_{\text{pulse}} = a \cdot \sum_q R(\lambda_q), \tag{6.5}$$

where a is an unknown scale factor expressed in [J], which corresponds to the maximum single order contribution to the pulse energy. Equation 6.5 represents the VUV pulse energy measured at the source position, but it becomes incomplete if the detector is placed in a different position. In this case, the equation must be corrected for the presence of filters, or any additional loss along the beamline between the source and the photodiode. In particular, filters attenuate the strength of the beam, but also limit the maximum photon energy which reaches the detector, such that not all harmonic orders generated are detected. Therefore, the VUV pulse energy on the photodiode is then given by:

$$E^*_{\text{pulse}} = a \cdot \sum_q R(\lambda_q) \cdot T(\lambda_q), \tag{6.6}$$

where $T(\lambda_q)$ is the total transmission of the used filters for each single harmonic wavelength λ_q. As a consequence, also the charge Q_{pulse} can be written as a function of the pulse energy E^*_{pulse} corrected by the photodiode responsivity resp(λ_q):

$$Q_{\text{pulse}} = a \cdot \sum_q (R(\lambda_q) \cdot T(\lambda_q) \cdot resp(\lambda_q)). \tag{6.7}$$

By combining equation 6.4 and 6.7, the scale factor a can be made explicit leading to:

$$E^*_{\text{pulse}} = \left(\frac{1}{n_p} \cdot \text{sens} \cdot \int_{t_0}^{t_1} S(t)\, dt \right) \cdot \frac{\sum_q R(\lambda_q)}{\sum_q (R(\lambda_q) \cdot T(\lambda_q) \cdot \text{resp}(\lambda_q))}. \tag{6.8}$$

The VUV pulse energy is then estimated by the photodiode trace and the recorded spectrum, taking in account the correction for losses between source and detector position in the function $T(\lambda_q)$.

However, for the specific case presented in this thesis, a further consideration can be made: the wavelength range detected by the photodiode spans approximately from 30 to 80 nm (see Fig. 6.2), and in this range, both $T(\lambda_q)$ and $\mathrm{resp}(\lambda_q)$ can be assumed constant. Equation 6.8 is therefore simplified to:

$$E^*_{\mathrm{pulse}} = \left(\frac{1}{n_p} \cdot \mathrm{sens} \cdot \int_{t_0}^{t_1} S(t)\, dt \right) \cdot \frac{1}{T \cdot \mathrm{resp}} \tag{6.9}$$

where $T = 0.79^2$ is the transmission coefficient of two 0.1 µm thick aluminum filters [HGD93], and resp =0.26 A/W is the photodiode responsivity in the wavelength range of interest. Note that, a direct measurement of the filters transmission would lead to a more precise estimation of the VUV pulse energy. Metallic foils are easily affected by oxidation, which leads to a decrease of the filter transmission due to the additional layer of oxygen. Even a limited time of exposure in air can cause an important drop in the filter transmission curve.

During the experiments, the analysis just described was used to estimate the VUV pulse energy generated immediately after acquiring the data with the photodiode, allowing for a real-time optimization of the generation conditions. Similarly to the procedure followed in Section 4.2.1, the VUV signal is studied as a function of several generation parameters, such as gas pressure or laser intensity. The goal of the procedure is to reach signal saturation with respect to all the parameters under consideration. Fig. 6.5a and Fig 6.6a depict an example of the trend of the VUV pulse energy with respect to the gas pressure in the SIGC measured with the focusing system A and B (see Tab. 6.1) respectively. In both cases, the gas used as generating medium is argon. In order to minimize the effect of shot-to-shot energy variations, every photodiode trace is averaged over 600 macro-pulses (bursts). The signal reaches a maximum and then starts to decrease. In case of focusing system A (Fig. 6.5a), the optimum is reached at about 40 mbar, while in case of system B (Fig 6.6a) it is at about 200 mbar. A higher optimum pressure is expected in this case, since the volume of interaction in the gas medium is smaller due to the smaller focus size. However, the difference in focus size does not explain alone a factor of 5 in the pressure. This is an indication that the generation conditions for the two cases are different, leading to two different pressure regimes despite the similar VUV output pulse energy.

The same procedure was used to optimize the HHG input driving IR pulse energy. In this case, the conversion efficiency is more significant than the mere VUV pulse energy, which could increase for an increasing input even for a

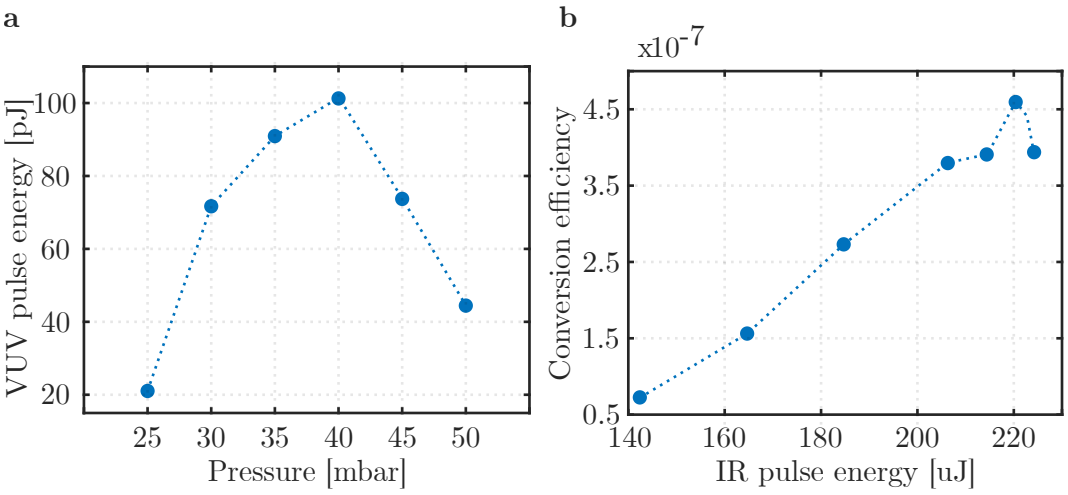

Figure 6.5: Optimization of the VUV signal, measured in November 2019, focusing system A. a) Trend of the VUV pulse energy, corrected for the beamline losses, with respect to the argon pressure in the SIGC. b) Conversion efficiency for the entire VUV spectrum as a function of the input IR pulse energy for a fixed argon pressure of 40 mbar. The input energy was controlled by means of a thin-film polarizer (TFP) attenuator.

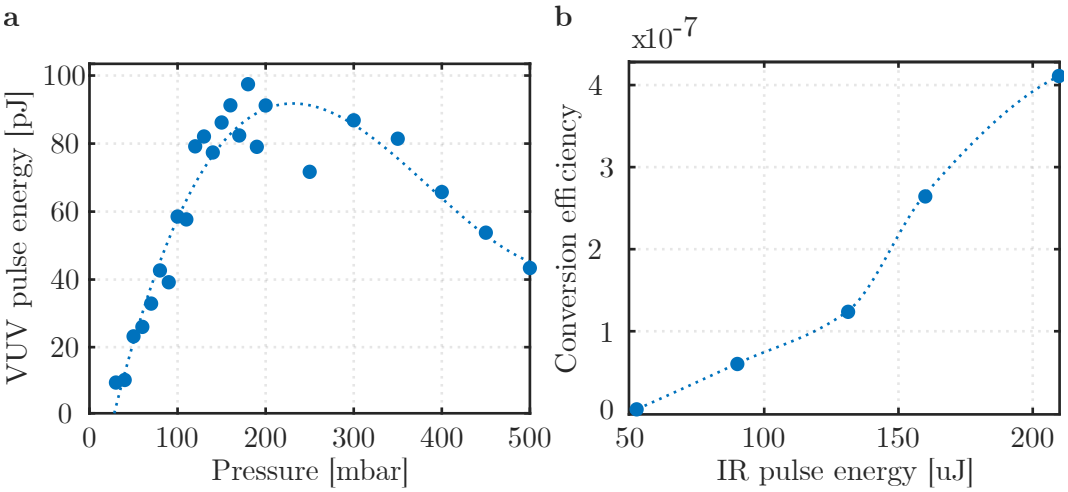

Figure 6.6: Optimization of the VUV signal, measured in July 2020, focusing system B. A 5% oxidation is considered for one Al filter after exposure in air. a) Argon pressure up to 500 mbar are tested in the SIGC. b) By attenuating the driving IR pulse energy with a set of ND filters, no clear saturation of the conversion efficiency is observed.

less efficient generation process. Fig. 6.5b and Fig. 6.6b show the estimated HHG efficiency as a function of the IR pulse energy. Differently from the previous case, the saturation of the signal is not clearly visible. In the case of focusing system A (Fig. 6.5b), a single measurement around 220 µJ led to a conversion efficiency higher than the one achieved for the maximum input pulse energy at 225 µJ, but no clear trend of saturation was observed. During the measurements the IR input pulse energy was controlled by a thin-film polarizer (TFP) attenuator. In case of focusing system B (Fig. 6.6b), the IR input energy is instead attenuated with neutral density (ND) filters, but this method does not allow for a detailed scan around the maximum input energy. The absence of a clear saturation of the signal could indicate a more efficient generation process at higher input pulse energies. The maximum conversion efficiencies measured are $4.6{\cdot}10^{-7}$ and $4.1{\cdot}10^{-7}$ for focusing system A and B respectively. A slightly higher efficiency was achieved using xenon as generating medium. In this case, a total conversion efficiency of $5.7 \cdot 10^{-7}$, corresponding to a maximum harmonic pulse energy of 0.12 nJ [App+20], has been measured with the focusing system A. However, the difference in the spectral range generated, shown in Fig. 6.2, led to a higher single harmonic order efficiency in case of xenon than of argon: for harmonic order 11^{th}, a $\sim 2.7{\cdot}10^{-7}$ efficiency has been achieved using xenon, which correspond to 57.6 pJ in this single harmonic order, compared to $6.6{\cdot}10^{-8}$ in argon. For completeness, it should be noted that during the test with the 4 mm long cell, a maximum conversion efficiency of $1.1{\cdot}10^{-7}$ for the full spectrum has been estimated with 145 mbar of argon. As already mentioned, this configuration is limited by the gas load leaking to the HHG chamber and a different vacuum system is required for stable operation.

In conclusion, during first commissioning test of the HHG source two different focusing systems were used (see Tab. 6.1). They provided similar results with a total VUV conversion efficiency in the 10^{-7} range and pulse energies up to 0.1 nJ. However, the generation studies performed do not ensure a complete optimization of the VUV signal, leaving room for further improvements. In particular, no clear saturation of the signal with respect to the input IR pulse energy has been observed for either focusing system investigated. A higher laser intensity in the gas medium could then allow for a higher generated VUV pulse energy. Further work on the driving laser optical setup and on a reliable automation of the generation parameters control will allow for a more precise HHG optimization and an improvement of the VUV signal is expected.

6.2 Incoupling in the FEL beamline

The coupling of the VUV radiation in the FL26 beamline is achieved by means of the incoupling mirror (see Sec. 5.2.5). The alignment of the mirror is critical and, due to the hyperboloidal surface, it can be quite challenging. For this reason, a first phase of the alignment of incoupling mirror and chamber was carried out together with the surveyors' group of DESY. The chamber is placed on two alignment stages mounted on a granite post, which is directly fixed on the floor of the experimental hall, see Fig. 6.7a. The stages provide flexibility in all directions and were used to readjusted the position of the chamber according to the technical design of the VUV beamline, with respect to references already existing in the experimental hall and on FL26.

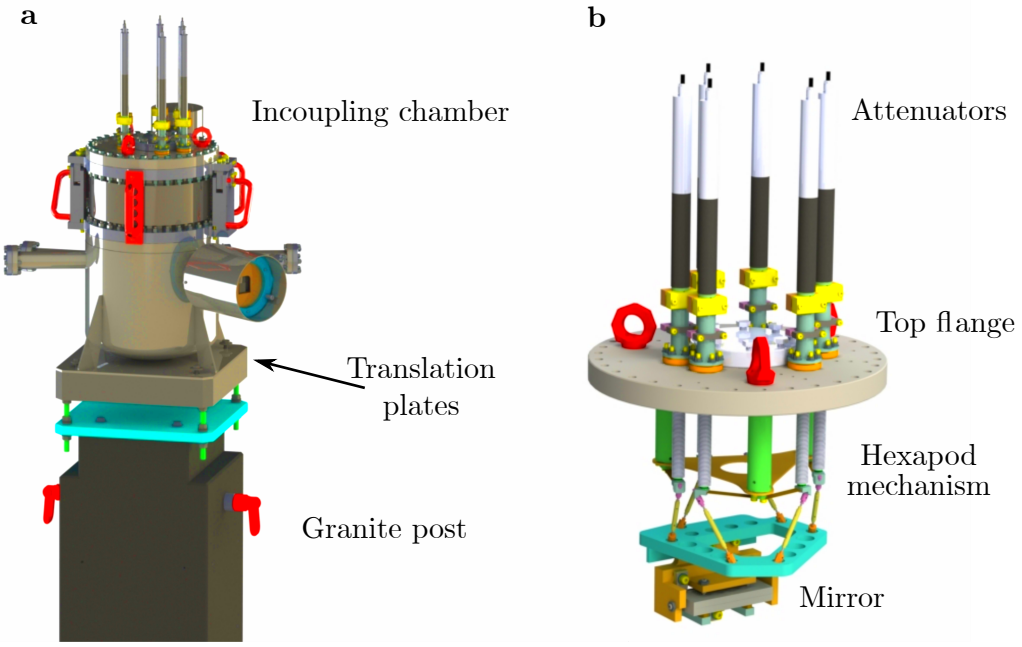

Figure 6.7: CAD drawing of the incoupling chamber and of the mirror mounting. a) The chamber is placed on a granite post fixed on the floor. Translation stage plates between the chamber and the post allow flexibility in the alignment. b) Information on the mirror position inside the chamber are transferred on the outside top flange. Fine adjustments are achieved with the hexapod mechanism on which the mirror holder is attached.

New references were also set in respect to the position of the mirror inside the chamber. For this procedure (called *fiducialization*), the top flange of the chamber on which the mirror holder is connected, see Fig. 6.7b, was placed on an external support. Using a dummy mirror in the holder, the information

of the mirror position were transfered on new references on the outside of the chamber top flange. The dummy mirror was then replaced with the real one in a portable clean room and the whole structure was craned back on the incoupling chamber. Due to the new references on the top flange, the relative position of the mirror is then known even when the chamber is closed. The top flange was slightly re-positioned in order to improve the mirror position with respect to the FL26 beamline references. This procedure ensures that the mirror is as close as possible to the nominal position specified in the technical design, proving a starting point for a more fine adjustment.

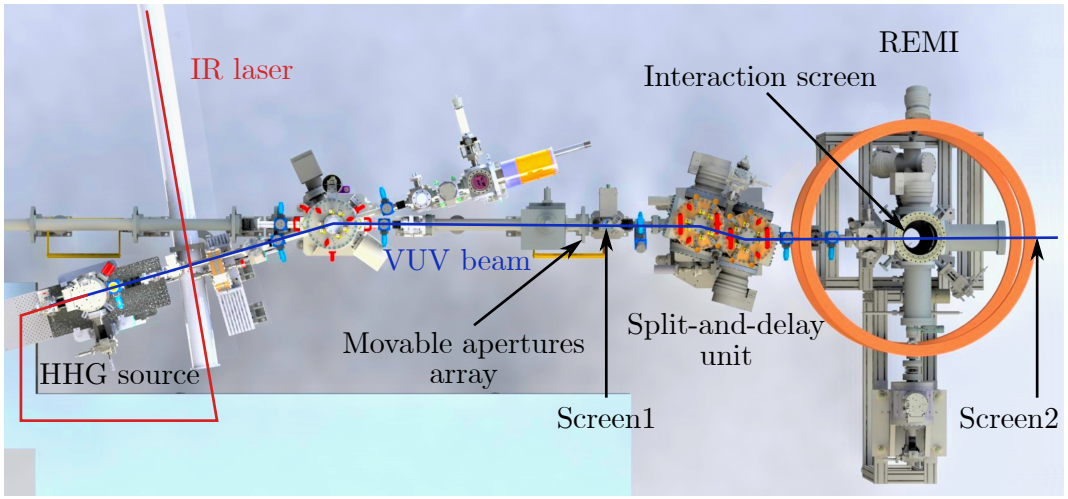

Figure 6.8: Positioning of the screens along FL26 used for the alignment of the IR and VUV beam. Screen1 is placed between the movable apertures array and the split-and-delay unit, Screen2 at the end of the endstation, while a third screen is at the interaction region inside REMI.

In a second phase of the alignment, the mirror was moved by means of the hexapod mechanism in the chamber while monitoring the beam position on the screens of FL26, see Fig. 6.8. Three different screens were used: Screen1 placed before the split-and-delay unit, Screen2 placed downstream of the REMI chamber, and the "interaction screen" in the focus point of the FEL beam. These screens are generally used for the alignment of the FEL beam together with an array of movable apertures. Taking in account the vertical shift between FEL and VUV beam in the technical design, during the alignment procedure, one of the apertures of the movable array was fixed 7.5 mm higher than the FEL nominal position. Due to its low intensity, the VUV beam is visible only in the interaction screen inside REMI . However, fluorescence from the IR beam can be easily observed on Screen1 and Screen2, which are Ce:YAG screens.

This fundamental radiation was therefore used for the alignment procedure, described in the following steps:

- The driving IR beam was aligned to the inline spectrometer, following the references on the optical breadboard.
- The incoupling mirror was inserted in the beampath and, by means of the only hexapod mechanism, it was translated to keep its center on the IR beam, monitoring Screen1.
- The mirror was then tilted to center the beam on the fixed aperture, monitoring Screen2.

After several iterations, the IR beam passed through the aperture and it was visible on all screens. Finally, the driving beam was blocked by means of an Al filter and the VUV radiation was observed on the interaction screen. Minor adjustment of the mirror position allowed to center the VUV focus on the same reference usually used for the FEL beam alignment. Fig 6.9 shows the image of the focused VUV beam. From a 2D gaussian fit of the spot, a diameter of 24.3 µm and of 18.3 µm is estimated in the horizontal and vertical axis, respectively. By taking in account the simulated spot size presented in Section 5.2.4, the VUV source point in the HHG chamber results <50 µm, which is smaller than the driving laser beam diameter in the gas (72 µm, focusing system A) as expected.

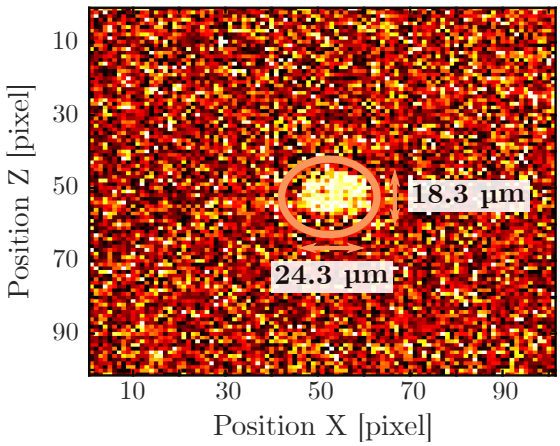

Figure 6.9: Focused VUV beam in REMI centered on the nominal FEL position (red circle). IR radiation blocked. A diameter of 24.3 µm and of 18.3 µm is calculated in the horizontal and vertical axis, respectively.

6.3 Commissioning experiment in REMI

After the successful alignment of the incoupling mirror, a first commissioning experiment was carried out using the focused VUV beam in REMI. The reaction microscope allows for the detection of ions and electrons from photo-ionization of a supersonic gas jet target. For this experiment, the VUV beam was focused into an argon target. Since the first ionization potential I_p of argon is 15.759(1) eV [Lia21], photo-ionization events are expected by all the harmonic orders ≥11 (17.5 eV). The results are presented in the following.

Photo-ion rate. The measured Ar^+ ion rates per pulse and estimated photon numbers are reported on Tab. 6.2 for three generation gas media in the HHG source.

Table 6.2: a) Ar^+ ion rate per pulse measured in REMI for three generation gas media in the HHG source. b) Estimated VUV photons per pulse in REMI in case of a 4 mm aperture in the beampath. Data from [App+20].

(a)

	Al filter	Small aperture	None
Xe	0.075	0.405	0.504
Kr	/	0.110	/
Ar	0.005	0.012	0.032

(b)

Small aperture
3.1×10^6
1.1×10^6
0.27×10^6

The experiment was repeated for different conditions: with the insertion of a 0.1 µm thick aluminum filter ("Al filter" in Tab. 6.2), with a 4 mm aperture instead of the filter ("Small aperture") and without any of the two ("None"). As already explained, the aluminum filter is used to block the remaining IR light, but it also affects the transmission of the VUV beam. Alternatively to the filter, an aperture can be used to block most of the IR beam, while letting the main part of the VUV beam propagate. This method relies on the different divergence between the fundamental and the harmonic radiation. In this case, the IR light is never completely suppressed but the transmission of the VUV beam is mostly not affected. A comparison between these options shows that the Ar^+ ion rate in xenon is increased up to 5 times for an aperture with respect to the aluminum filter case. Without any blocking of the IR beam, the Ar^+ ion rate measured is the highest, but the contribution to the ionization by IR photons is unknown.

Moreover, the measured Ar^+ ion rate in case of xenon as generation medium, is always higher compared to the other gases, followed by krypton and argon. This is in agreement with the expectations since the ionization potential of xenon is the lowest, leading to an more efficient HHG process in the intensity range used as estimated by the photodiode measurements in Section 6.1.2. From the ion rate, the absolute photon number per pulse can be estimated taking in account the photo-ionization cross-sections [Ala16] at the harmonic photon energies. A maximum of 3.1×10^6 photons per pulse has been estimated for HHG in xenon, which corresponds to 0.01 nJ per pulse. To compare correctly this result with the photodiode estimation, multiple corrections must be accounted for. The coupling of the VUV beam in the FEL beamline until the REMI chamber requires reflections on three mirrors with a reflectivity of 80% each (total 50%). In addition, harmonics below the 11^{th} order do not provide enough photon energy for single-photon ionization of argon atoms and therefore will not generate a signal. By taking in account these corrections, the estimations of the pulse energy from the photodiode and the REMI measurements are consistent with each other.

The overall stability of the VUV source in terms of beam pointing and photon flux was also evaluated by the Ar^+ ion rate in a 14-hours-long measurement. Fig. 6.10 shows fluctuations of less than 20 % over the whole measurement, demonstrating that the VUV source is sufficiently stable for long time experiments.

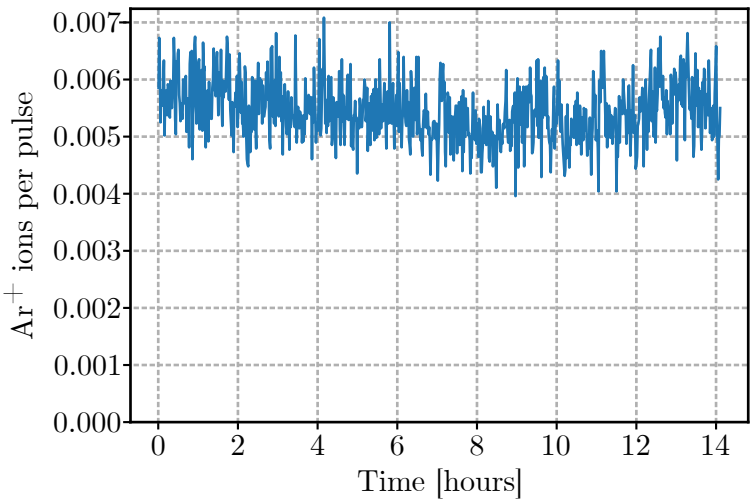

Figure 6.10: Ar^+ ion rate per pulse averaged over 1 minute for a 14-hours-long measurement. Figure adapted from [App+20].

Photo-electron momentum. Further information are given by the reconstructed momenta of the detected photo-electrons, depict in Fig. 6.11 in case of argon as generation gass used in the HHG source. The 2D distribution is shown as a function of the longitudinal and transverse momentum, $p_{\parallel}$ and $p_{\perp}$, with respect to the polarization axis in cylindrical coordinates. The brightness indicates the electron count rate.

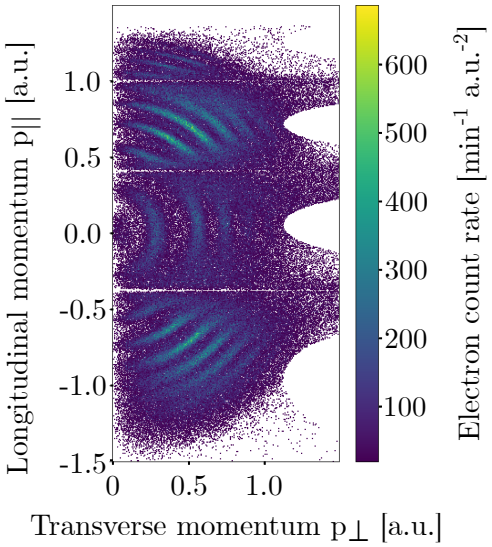

Figure 6.11: Argon photo-electron momentum distributions. Half circles correspond to constant kinetic energy of the electron. VUV radiation generated in 40 mbar of argon with an 4 mm aperture used to block the fundamental IR radiation.

As expected, several discrete lines of constant kinetic energy are present. The harmonic spectrum is reflected in the electron momentum distributions: each discrete line represents the contribution of one harmonic order to the photo-ionization, with the electron energy equal to the harmonic photon energy minus the target binding energy I_p. A direct comparison between the harmonic spectra observed on the inline spectrometer and the photo-electron rate is given in Fig. 6.12 for three different generating media used in the HHG source. Starting from the first line (11^{th} harmonic) above the ionization threshold, clearly all the spectra components of the VUV beam reach the interaction region in REMI and contribute to the photo-ionization.

The photo-electron momenta allow also to test the influence of the IR beam on the photo-ionization. Fig. 6.13 shows a comparison between the reconstructed momenta with and without the aluminum filter or the 4 mm aperture in the VUV beampath. If the fundamental radiation is not suppressed

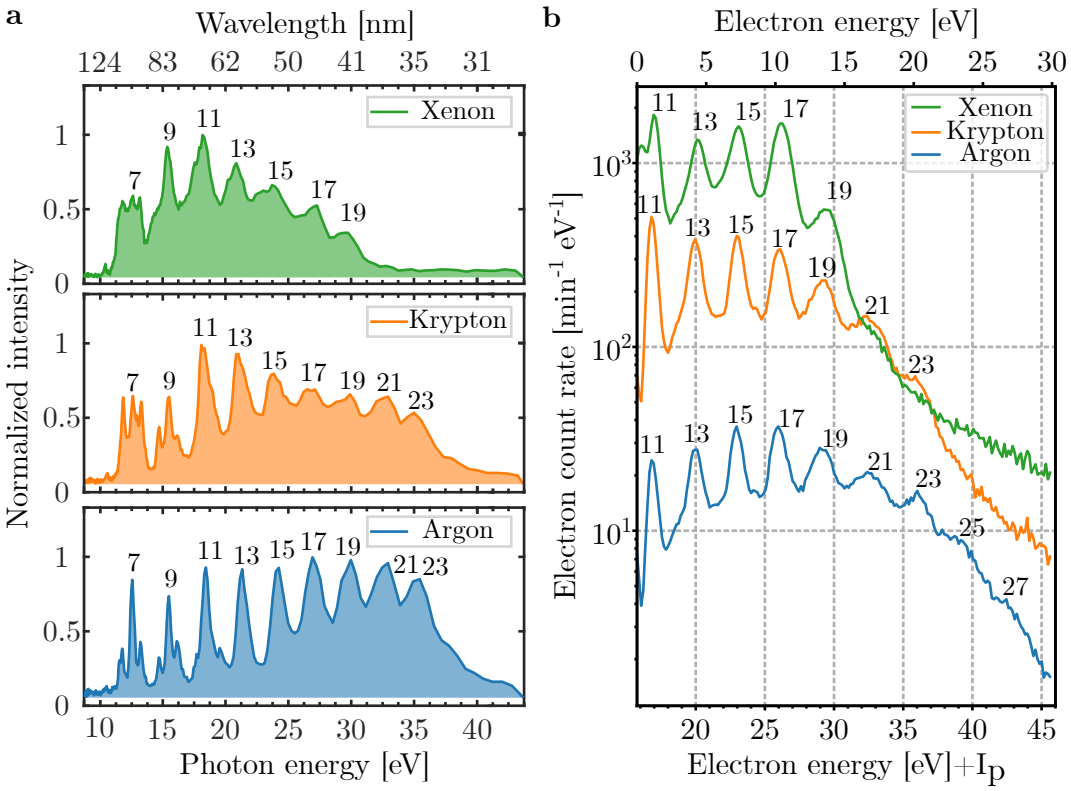

Figure 6.12: Comparison between the harmonic spectra detected with the inline spectrometer (a) and the photo-electron energy distributions measured in REMI (b). The harmonic orders are indicated by the black numbers. Figure adapted from [App+20].

(Fig. 6.13c), the photo-electrons energy is modulated by the presence of IR photons and sidebands close to each harmonic order contribution appear. With the insertion of the filter (Fig. 6.13a), this effect is completely suppressed but the electron rate is significantly reduced, leading to longer acquisition times. The insertion of an aperture (Fig. 6.13b) leads to a good compromise without visible sidebands and with an events rate not so strongly reduced, providing a valuable alternative to the use of filters.

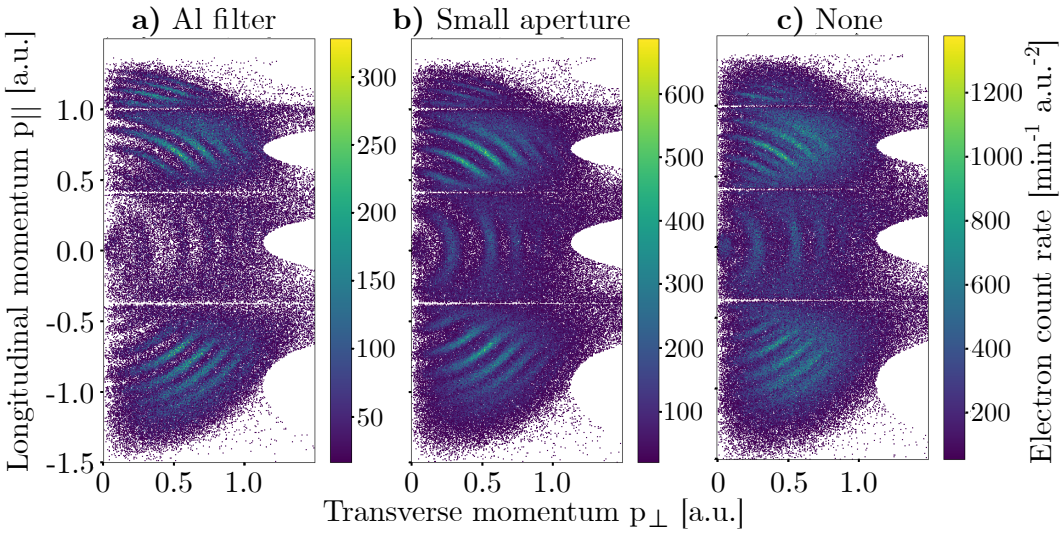

Figure 6.13: Comparison of argon photo-electron momenta between a) a 0.1 µm Al filter, b) a 4 mm aperture and c) none, inserted in the beampath. The VUV radiation was generated in 40 mbar of argon in the HHG source. Figure adapted from [App+20].

In summary, during commissioning of the beamline the generation of VUV radiation in different gas media and its characterization in terms of spectral components and pulse energy was achieved. The radiation in the spectral range from 10 to 40 eV with 0.1 nJ pulse energy was successfully coupled into the FL26 beamline and focused in the reaction microscope, where first photo-ionization tests in argon were performed. A 14-hours-long measurement of the Ar^+ ion rate in REMI shown that the HHG source can be employed in long time acquisitions without external adjustments.

6.4 Development perspectives for the VUV beamline

In order to increase the performance of the HHG source in terms of VUV pulse energy and to facilitate the control of the beamline status, several improvements to the beamline have been already planned or are under discussion. Additionally, the current capabilities of the source can be extended by employing different driving wavelengths available in the experimental hall, which would allow for a very versatile setup. The most important upgrades are shortly described in the following.

Beamline upgrades. From the VUV generation tests described in Section 6.1, it results that higher driving laser intensities in the gas medium could lead to a more efficient HHG process. This assertion is supported by the fact that no saturation of the conversion efficiency has been observed with respect of the input pulse energy. Additionally, the cutoff energy reached in the HHG spectrum, which is directly related to the laser intensity, is lower than expected. In the initial experiments employing a Ti:Sapphire CPA system, described in Section 4.2, a cutoff energy of 52.5 eV (corresponding to harmonic order 33) was detected for HHG in argon compared to the VUV beamline result of 39.7 eV (harmonic order 25) in Section 6.1. In order to solve this issue, it is necessary to perform further tests on the laser optical setup and focusing system to identify any source of perturbation. A strong degradation over time of the silver-coated mirrors quality in the laser optical setup has been observed. The reasons for this degradation, and the relation with the not ideal laser focusing conditions, are still under investigation. Since no degradation on dielectric-coated mirrors has been observed, all silver-coated mirrors in the optical setup will soon be exchanged with broadband dielectric-coated ones. Due to the higher reflectivity ($> 99\%$ instead of 95%) of broadband dielectric-coated mirrors, a small increase of the IR pulse energy at the focusing system is expected.

Moreover, the HHG optimization procedure requires to scan several generation parameters. While the pressure in the SIGC is controlled by a regulating valve and can be changed remotely, the plate position with respect to the focus and the input pulse energy are scanned manually. With the automation of the control for these parameters, the optimization procedure could be less time consuming, more precise and user friendly.

Another important upgrade concerns the installation of VUV reserved apertures. As shown in Section 6.3, the use of a small aperture, instead of metallic filters, is a valid method to suppress the remaining fundamental IR light without affecting the transmission of the VUV beam. The aperture array present at FL26 is not suitable for the simultaneous propagation of VUV and FEL beams due to their difference in height. In order to decouple the size control of the two beams, a set of apertures reserved to the VUV beam will be soon installed in the filterwheel, while an already existing second aperture array, placed upstream of the incoupling chamber, will be used for the FEL beam.

Extension of the source capabilities. The HHG process strongly depends on the driving laser parameters, in particular on the input pulse energy and wavelength. Within the mentioned program, *FLASH2020+*, the optical laser of the FLASH II experimental hall will be upgraded. Pulse energies up to 1 mJ, 3 times higher than the currently available value, are expected to be delivered at the experimental endstations. The higher pulse energy will allow to relax the focusing conditions for HHG and, therefore, to facilitate the phase matching of the process. Moreover, additional driving wavelengths can be used to expand the capabilities of the VUV source. Recently, the mid-infrared (MIR) Yb:YAG Innoslab amplifier (1030 nm, 1 ps) used as OPCPA pump has been post-compressed down to 60 fs pulses [Vio+21] for pump-probe experiments. The pulses are spectrally broadened in a 2 m long multi-pass cell (MPC) unit, then they are compressed and frequency-doubled. Pulse energies up to 800 µJ at 1030 nm and 225 µJ at 515 nm are now available at the beamline FL24. Both wavelengths could be used in the future as driver of the HHG process. In particular, a MIR driver would allow for an extension of the HHG spectrum potentially up to hundreds of eV. Additionally the 1030 nm and the 780 nm beams can be employed in sum-frequency generation (SFG) schemes to deliver visible and UV pulses. Preliminary simulations show the possibility to generate up to 400 µJ pulse energy at 450 nm and 300 µJ at 313 nm with pulse duration of 20 fs. These short wavelengths, as well as the 515 nm beam, would lead to more narrow HHG spectra but with a higher conversion efficiency per harmonic order [Com+19b]. All these possible drivers for the HHG process offer great potential to the VUV source. Nevertheless, the driver laser, its parameters, the harmonics generation conditions and the optimization of the process must be all chosen accordingly to the specific application under study.

For instance, transient absorption experiments could benefit from a broad harmonic spectrum, therefore, a NIR or MIR driver would be preferred. For pump-probe experiments in REMI that address specific electronic energy levels, an optimization of the signal around the harmonic orders of interest could be more favorable. Additionally, the use of a short-wavelength driver would allow for a higher photon flux compared to a longer driver.

Chapter 7

Conclusion

7.1 Summary

In this work, the novel VUV beamline at the free-electron laser FLASH has been presented. The beamline is based on high order harmonic generation in gas driven by NIR femtosecond pulses delivered by the OPCPA laser system of the FLASH2 experimental hall. The laser system is optically synchronized with the unique FEL burst timing for pump-probe experiments. The VUV radiation is coupled in the FEL endstation REMI, which features a reaction microscope for investigations of ionization dynamics in gas targets. With this unique setup, the combination of a HHG-based source and a FEL is made possible for the first time in a permanent installation. The complementary properties of these two sources allow to expand the available parameter space for two-color time-resolved studies in the XUV spectral range at femtosecond timescales.

Due to the ultra-high vacuum required during operation of the reaction microscope, the VUV beamline design had to be optimized in terms of pressure conditions, while keeping its length suitable to the limited available space in the experimental hall. Preliminary studies on a semi-infinite gas cell have shown the suitability of this configuration for HHG at the input pulse energy range provided by the OPCPA system. Taking advantage of the abrupt transition from gas to vacuum of such configuration, a compact and reliable system

of differential pumping stages was implemented along the VUV beamline in order to achieve the vacuum requirements. Additionally, the emitted VUV spectrum can be resolved in an inline spectrometer, which makes use of a compact geometry based on transmission gratings, while a rotatable double filterwheel allows for its spectral tuning. The coupling of the VUV radiation into the FEL beamline is achieved via a hyperboloidal carbon-coated mirror, which is followed by a pre-existing split-and-delay unit and a focusing mirror for pump-probe experiments in REMI. The hyperboloidal mirror specifications and alignment are critical for the correct focusing of the VUV beam, which must match the FEL focus position despite the two source points being placed more than 80 m away from each other.

First results have shown the generation of VUV radiation in the spectral range from 10 to 40 eV with 0.1 nJ pulse energy at the source position. The beam was successfully focused down to a 20 µm diameter into REMI and employed for first proof-of-principle studies enabling the detection of photo-ions and photo-electrons from an argon gas target. A 14-hours-long measurement of the Ar^+ ion rate in REMI showed the source capabilities for future long time VUV-XUV pump-probe experiments.

7.2 Outlook

The VUV beamline at FLASH represents an unique permanent installation which allows for the combination of a HHG-based source and a FEL beam. The beamline is an addition on the already innovative REMI endstation, where FEL-FEL and FEL-NIR pump-probe schemes are also available in combination with a reaction microscope for coincident particle detection and with a, soon to be installed, XUV spectrometer for transient absorption spectroscopy experiments. The endstation combines, therefore, three state-of-art light sources with two powerful detectors for novel investigations of ultrafast dynamics in atomic and molecular targets.

A first application employing the VUV beamline is scheduled for October 2021. It involves FEL-pump HHG-probe experiments for electron dynamics studies in O_2 molecule using the new XUV spectrometer. In the spectrometer the FEL and VUV beam are refocused downstream of REMI in a gas target for transient absorption spectroscopy experiments. Since the two beams spatially overlap only in the focus, their spectra can be detected separately after the

interaction with the target. In the proposed experiment, the chosen target is the O_2 molecule which, when ionized, presents several excited states each with a corresponding potential energy curve [Mar+82]. The different dissociation channels can be tracked by means of time-resolved techniques gaining insight on the dissociation dynamics [Mag+12; Cör+15]. By taking advantage of the combination between FEL and HHG-based source at the REMI endstation, the dissociation pathways of the molecule can be temporally and spectrally investigated. The narrow FEL spectrum is able to directly ionize the O_2 molecule and can be used to select a specific molecular excitation energy. Meanwhile, the broad HHG spectrum allows to identify several absorption resonances of atomic and molecular fragments in the region from 10 to 40 eV making use of transient absorption spectroscopy. A depletion of the absorption signal would indicate the molecule dissociation and, by varying the time delay between pump and probe pulse, the dissociation dynamics can be resolved. The experiment can be repeated for several different pathways by tuning the FEL photon energy at the excitation energy required.

In addition to transient absorption spectroscopy, molecular dynamics studies at REMI would also benefit of the two-color pump-probe scheme. For instance, a VUV photon can be used to perturb the target under investigation by creating an excited molecular ion, while the FEL photon will completely ionize the system. By recording the resulting molecular fragments with the reaction microscope, information on the dynamics and the geometrical structure of the molecule can be deduced. Depending on the target under study, the photon energies of the FEL and VUV pulse can be chosen accordingly to the dynamics of interest taking advantages of the spectral tunability of the two sources. Proposed experiments include fragmentation dynamics of small molecules, real-time tracking of charge distribution, relaxation dynamics in rare gas clusters and atomic nonlinearities in high frequency fields. However, coincident measurements in REMI will be affected by the currently limited pulse energy of the VUV beam (0.1 nJ at the source), with respect to the more energetic FEL, which will lead to very long acquisition times. A further optimization of the generated pulse energy, in the specific spectral range of interest, is then required to perform successful FEL-HHG pump-probe experiments in REMI.

Bibliography

[Abe+19] Rafael Abela, Arturo Alarcon, Jürgen Alex, Christopher Arrell, Vladimir Arsov, Simona Bettoni, Markus Bopp, Christoph Bostedt, H-H Braun, Marco Calvi, et al. "The SwissFEL soft X-ray free-electron laser beamline: Athos". In: *Journal of synchrotron radiation* 26.4 (2019), pp. 1073–1084. DOI: 10.1107/S1600577519003928

[Ack+07] Wet al Ackermann, G Asova, V Ayvazyan, A Azima, N Baboi, J Bähr, V Balandin, B Beutner, A Brandt, A Bolzmann, et al. "Operation of a free-electron laser from the extreme ultraviolet to the water window". In: *Nature photonics* 1.6 (2007), p. 336. DOI: 10.1038/nphoton.2007.76

[Ala16] Robert Pugliese Alain Bertrand Giorgio Paolucci. *Atomic Calculation of Photoionization Cross-Sections and Asymmetry Parameters*. 2016

[All+12] E Allaria, Roberto Appio, L Badano, WA Barletta, S Bassanese, SG Biedron, A Borga, E Busetto, D Castronovo, P Cinquegrana, et al. "Highly coherent and stable pulses from the FERMI seeded free-electron laser in the extreme ultraviolet". In: *Nature Photonics* 6.10 (2012), pp. 699–704. DOI: 10.1038/nphoton.2012.233

[All+13b] E Allaria, D Castronovo, P Cinquegrana, P Craievich, Massimo Dal Forno, MB Danailov, G D'Auria, A Demidovich, G De Ninno, S Di Mitri, et al. "Two-stage seeded soft-X-ray free-electron laser". In: *Nature Photonics* 7.11 (2013), pp. 913–918. DOI: 10.1038/nphoton.2013.277

[All+14] Enrico Allaria et al. "Control of the Polarization of a Vacuum-Ultraviolet, High-Gain, Free-Electron Laser". In: *Phys. Rev. X* 4 (4 Dec. 2014), p. 041040. DOI: 10.1103/PhysRevX.4.041040

[All+15] E. Allaria et al. "The FERMI free-electron lasers". In: *Journal of Synchrotron Radiation* 22.3 (May 2015), pp. 485–491. DOI: 10.1107/S1600577515005366

[Ama+12] J Amann, W Berg, V Blank, F-J Decker, Y Ding, P Emma, Y Feng, J Frisch, D Fritz, J Hastings, et al. "Demonstration of self-seeding in a hard-X-ray free-electron laser". In: *Nature photonics* 6.10 (2012), pp. 693–698. DOI: 10.1038/nphoton.2012.180

[App+20] Elisa Appi, Christina C Papadopoulou, Jose Louise Mapa, Nishad Wesavkar, Christoph Jusko, Philip Mosel, Skirmantas Ališauskas, Tino Lang, Christoph M Heyl, Bastian Manschwetus, et al. "A synchronized VUV light source based on high-order harmonic generation at FLASH". In: *Scientific Reports* 10.1 (2020), pp. 1–11. DOI: 10.1038/s41598-020-63019-2

[Ayv+06] Valeri Ayvazyan, N Baboi, J Bähr, V Balandin, B Beutner, A Brandt, I Bohnet, A Bolzmann, R Brinkmann, OI Brovko, et al. "First operation of a free-electron laser generating GW power radiation at 32 nm wavelength". In: *The European Physical Journal D-Atomic, Molecular, Optical and Plasma Physics* 37.2 (2006), pp. 297–303. DOI: 10.1140/epjd/e2005-00308-1

[Azo+19] Doron Azoury, Omer Kneller, Michael Krüger, Barry D Bruner, Oren Cohen, Yann Mairesse, and Nirit Dudovich. "Interferometric attosecond lock-in measurement of extreme-ultraviolet circular dichroism". In: *Nature Photonics* 13.3 (2019), pp. 198–204. DOI: 10.1038/s41566-019-0350-5

[Bal+92] Ph Balcou, C Cornaggia, ASL Gomes, LA Lompre, and Anne L'Huillier. "Optimizing high-order harmonic generation in strong fields". In: *Journal of Physics B: Atomic, Molecular and Optical Physics* 25.21 (1992), p. 4467. DOI: 10.1088/0953-4075/25/21/014

[BCG01] M. Bellini, C. Corsi, and M. C. Gambino. "Neutral depletion and beam defocusing in harmonic generation from strongly ionized media". In: *Phys. Rev. A* 64 (2 July 2001), p. 023411. DOI: 10.1103/PhysRevA.64.023411

[BDS19] Axel Brachmann, M Dunham, and JF Schmerge. *LCLS-II-Status and Upgrades*. Tech. rep. SLAC National Accelerator Lab., Menlo

Park, CA (United States), 2019. DOI: 10.18429/JACoW-FEL2019-FRA02

[Ben+14] Craig Benko, Thomas K Allison, Arman Cingöz, Linqiang Hua, François Labaye, Dylan C Yost, and Jun Ye. "Extreme ultraviolet radiation with coherence time greater than 1 s". In: *Nature Photonics* 8.7 (2014), pp. 530–536. DOI: 10.1038/nphoton.2014.132

[Bia+21a] Elisa Biasin, Zachary W Fox, Amity Andersen, Kathryn Ledbetter, Kasper S Kjær, Roberto Alonso-Mori, Julia M Carlstad, Matthieu Chollet, James D Gaynor, James M Glownia, et al. "Direct observation of coherent femtosecond solvent reorganization coupled to intramolecular electron transfer". In: *Nature chemistry* (2021), pp. 1–7. DOI: 10.1038/s41557-020-00629-3

[BIJ08] E Brunetti, R Issac, and DA Jaroszynski. "Quantum path contribution to high-order harmonic spectra". In: *Physical Review A* 77.2 (2008), p. 023422. DOI: 10.1103/PhysRevA.77.023422

[BKC13] Anton Barty, Jochen Küpper, and Henry N. Chapman. "Molecular Imaging Using X-Ray Free-Electron Lasers". In: *Annual Review of Physical Chemistry* 64.1 (2013), pp. 415–435. DOI: 10.1146/annurev-physchem-032511-143708

[BMM20] Johan Bielecki, Filipe RNC Maia, and Adrian P Mancuso. "Perspectives on single particle imaging with x rays at the advent of high repetition rate x-ray free electron laser sources". In: *Structural Dynamics* 7.4 (2020), p. 040901. DOI: 10.1063/4.0000024

[BPN84] R Bonifacio, C Pellegrini, and LM Narducci. "Collective instabilities and high-gain regime free electron laser". In: *AIP conference proceedings*. Vol. 118. 1. American Institute of Physics. 1984, pp. 236–259. DOI: doi.org/10.1063/1.34640

[Bra+07] M. Braun et al. "Ultrafast Changes of Molecular Crystal Structure Induced by Dipole Solvation". In: *Phys. Rev. Lett.* 98 (24 June 2007), p. 248301. DOI: 10.1103/PhysRevLett.98.248301

[Bri+09] J.-P. Brichta, M. C. H. Wong, J. B. Bertrand, H.-C. Bandulet, D. M. Rayner, and V. R. Bhardwaj. "Comparison and real-time monitoring of high-order harmonic generation in different sources". In: *Phys. Rev. A* 79 (3 Mar. 2009), p. 033404. DOI: 10.1103/PhysRevA.79.033404

[Bro15] WS Brocklesby. "Progress in high average power ultrafast lasers". In: *The European Physical Journal Special Topics* 224.13 (2015), pp. 2529–2543. DOI: 10.1140/epjst/e2015-02562-0

[Bru90] F. Brunel. "Harmonic generation due to plasma effects in a gas undergoing multiphoton ionization in the high-intensity limit". In: *J. Opt. Soc. Am. B* 7.4 (Apr. 1990), pp. 521–526. DOI: 10.1364/JOSAB.7.000521

[Cal+14] F. Calegari et al. "Ultrafast electron dynamics in phenylalanine initiated by attosecond pulses". In: *Science* 346.6207 (2014), pp. 336–339. DOI: 10.1126/science.1254061

[Cal+16] Francesca Calegari, Giuseppe Sansone, Salvatore Stagira, Caterina Vozzi, and Mauro Nisoli. "Advances in attosecond science". In: *Journal of Physics B: Atomic, Molecular and Optical Physics* 49.6 (Feb. 2016), p. 062001. DOI: 10.1088/0953-4075/49/6/062001

[Cal+21] Carlo Callegari, Alexei N. Grum-Grzhimailo, Kenichi L. Ishikawa, Kevin C. Prince, Giuseppe Sansone, and Kiyoshi Ueda. "Atomic, molecular and optical physics applications of longitudinally coherent and narrow bandwidth Free-Electron Lasers". In: *Physics Reports* 904 (2021). Atomic, molecular and optical physics applications of longitudinally coherent and narrow bandwidth Free-Electron Lasers, pp. 1–59. DOI: 10.1016/j.physrep.2020.12.002

[Cas+13] J C Castagna, B Murphy, J Bozek, and N Berrah. "X-ray split and delay system for soft x-rays at LCLS". In: *Journal of Physics: Conference Series* 425.15 (Mar. 2013), p. 152021. DOI: 10.1088/1742-6596/425/15/152021

[Cav+07] Adrian L Cavalieri, Norbert Müller, Th Uphues, Vladislav S Yakovlev, Andrius Baltuška, Balint Horvath, B Schmidt, L Blümel, R Holzwarth, Stefan Hendel, et al. "Attosecond spectroscopy in condensed matter". In: *Nature* 449.7165 (2007), pp. 1029–1032. DOI: 10.1038/nature06229

[Cha+20] Yao Chang et al. "Ultraviolet photochemistry of ethane: implications for the atmospheric chemistry of the gas giants". In: *Chem. Sci.* 11 (19 2020), pp. 5089–5097. DOI: 10.1039/D0SC01746A

[Che+10] M.-C. Chen, P. Arpin, T. Popmintchev, M. Gerrity, B. Zhang, M. Seaberg, D. Popmintchev, M. M. Murnane, and H. C. Kapteyn. "Bright, Coherent, Ultrafast Soft X-Ray Harmonics Spanning the Water Window from a Tabletop Light Source". In: *Phys. Rev.*

Lett. 105 (17 Oct. 2010), p. 173901. DOI: 10.1103/PhysRevLett.105.173901

[CHW16] Aaron von Conta, Martin Huppert, and Hans Jakob Wörner. "A table-top monochromator for tunable femtosecond XUV pulses generated in a semi-infinite gas cell: Experiment and simulations". In: *Review of Scientific Instruments* 87.7 (2016), p. 073102. DOI: 10.1063/1.4955263

[CM07] A. Couairon and A. Mysyrowicz. "Femtosecond filamentation in transparent media". In: *Physics Reports* 441.2 (2007), pp. 47–189. DOI: 10.1016/j.physrep.2006.12.005

[Com+19b] A Comby, D Descamps, S Beauvarlet, A Gonzalez, F Guichard, S Petit, Y Zaouter, and Y Mairesse. "Cascaded harmonic generation from a fiber laser: a milliwatt XUV source". In: *Optics express* 27.15 (2019), pp. 20383–20396. DOI: 10.1364/OE.27.020383

[Con+99b] E. Constant, D. Garzella, P. Breger, E. Mével, Ch. Dorrer, C. Le Blanc, F. Salin, and P. Agostini. "Optimizing High Harmonic Generation in Absorbing Gases: Model and Experiment". In: *Phys. Rev. Lett.* 82 (8 Feb. 1999), pp. 1668–1671. DOI: 10.1103/PhysRevLett.82.1668

[Con01] Robert E Continetti. "Coincidence spectroscopy". In: *Annual review of physical chemistry* 52.1 (2001), pp. 165–192. DOI: 10.1146/annurev.physchem.52.1.165

[Con98] Jean-Patrick Connerade. *Highly excited atoms*. 9. Cambridge University Press, 1998

[Cör+15] Philipp Cörlin, Andreas Fischer, Michael Schönwald, Alexander Sperl, Tomoya Mizuno, Uwe Thumm, Thomas Pfeifer, and Robert Moshammer. "Probing calculated O_2^+ potential-energy curves with an XUV-IR pump-probe experiment". In: *Phys. Rev. A* 91 (4 Apr. 2015), p. 043415. DOI: 10.1103/PhysRevA.91.043415

[Cor93] P. B. Corkum. "Plasma perspective on strong field multiphoton ionization". In: *Phys. Rev. Lett.* 71 (13 Sept. 1993), pp. 1994–1997. DOI: 10.1103/PhysRevLett.71.1994

[Cza+07] A Czasch, J Milnes, N Hay, W Wicking, and O Jagutzki. "Position- and time-sensitive single photon detector with delay-line readout". In: *Nuclear Instruments and Methods in Physics Research Section A: Accelerators, Spectrometers, Detectors and Associated Equip-*

ment 580.2 (2007), pp. 1066–1070. DOI: 10.1016/j.nima.2007.06.063

[Dan+14] Miltcho B. Danailov et al. "Towards jitter-free pump-probe measurements at seeded free electron laser facilities". In: *Opt. Express* 22.11 (June 2014), pp. 12869–12879. DOI: 10.1364/OE.22.012869

[Dea+77] D. A. G. Deacon, L. R. Elias, J. M. J. Madey, G. J. Ramian, H. A. Schwettman, and T. I. Smith. "First Operation of a Free-Electron Laser". In: *Phys. Rev. Lett.* 38 (16 Apr. 1977), pp. 892–894. DOI: 10.1103/PhysRevLett.38.892

[Dec+19] Winfried Decking, F Brinker, L Froehlich, R Kammering, T Limberg, S Liu, D Noelle, M Omet, M Scholz, T Wamsat, et al. "Status of the European XFEL". In: *10th Int. Particle Accelerator Conf* 17.17.5 (2019), pp. 10–16. DOI: 10.18429/JACoW-IPAC2019-TUPRB020

[Din+21a] Thomas Ding et al. "XUV pump–XUV probe transient absorption spectroscopy at FELs". In: *Faraday Discuss.* (2021). DOI: 10.1039/D0FD00107D

[DJP92] A. Dubietis, G. Jonušauskas, and A. Piskarskas. "Powerful femtosecond pulse generation by chirped and stretched pulse parametric amplification in BBO crystal". In: *Optics Communications* 88.4 (1992), pp. 437–440. DOI: 10.1016/0030-4018(92)90070-8

[DLM12] J M Dahlström, A L'Huillier, and A Maquet. "Introduction to attosecond delays in photoionization". In: *Journal of Physics B: Atomic, Molecular and Optical Physics* 45.18 (Aug. 2012), p. 183001. DOI: 10.1088/0953-4075/45/18/183001

[Dom+20] Péter Dombi, Zsuzsanna Pápa, Jan Vogelsang, Sergey V. Yalunin, Murat Sivis, Georg Herink, Sascha Schäfer, Petra Groß, Claus Ropers, and Christoph Lienau. "Strong-field nano-optics". In: *Rev. Mod. Phys.* 92 (2 June 2020), p. 025003. DOI: 10.1103/RevModPhys.92.025003

[Dör+00] R. Dörner, V. Mergel, O. Jagutzki, L. Spielberger, J. Ullrich, R. Moshammer, and H. Schmidt-Böcking. "Cold Target Recoil Ion Momentum Spectroscopy: a 'momentum microscope' to view atomic collision dynamics". In: *Physics Reports* 330.2 (2000), pp. 95–192. DOI: 10.1016/S0370-1573(99)00109-X

[Dor+19] Kevin M Dorney, Laura Rego, Nathan J Brooks, Julio San Román, Chen-Ting Liao, Jennifer L Ellis, Dmitriy Zusin, Christian Gentry,

Quynh L Nguyen, Justin M Shaw, et al. “Controlling the polarization and vortex charge of attosecond high-harmonic beams via simultaneous spin–orbit momentum conservation”. In: *Nature photonics* 13.2 (2019), pp. 123–130. DOI: 10.1038/s41566-018-0304-3

[Ell+17] Jennifer L Ellis, Kevin M Dorney, Charles G Durfee, Carlos Hernández-Garcı
a, Franklin Dollar, Christopher A Mancuso, Tingting Fan, Dmitriy Zusin, Christian Gentry, Patrik Grychtol, et al. “Phase matching of noncollinear sum and difference frequency high harmonic generation above and below the critical ionization level”. In: *Optics express* 25.9 (2017), pp. 10126–10144. DOI: 10.1364/OE.25.010126

[Ema+15a] Florian Emaury, Andreas Diebold, Clara J Saraceno, and Ursula Keller. “Compact extreme ultraviolet source at megahertz pulse repetition rate with a low-noise ultrafast thin-disk laser oscillator”. In: *Optica* 2.11 (2015), pp. 980–984. DOI: 10.1364/OPTICA.2.000980

[Emm+10] Paul Emma, R Akre, J Arthur, R Bionta, C Bostedt, J Bozek, A Brachmann, P Bucksbaum, Ryan Coffee, F-J Decker, et al. “First lasing and operation of an ångstrom-wavelength free-electron laser”. In: *nature photonics* 4.9 (2010), pp. 641–647. DOI: 10.1038/nphoton.2010.176

[Erk+18] Benjamin Erk, Jan P Müller, Cédric Bomme, Rebecca Boll, Günter Brenner, Henry N Chapman, Jonathan Correa, Stefan Düsterer, Siarhei Dziarzhytski, Stefan Eisebitt, et al. “CAMP@FLASH: an end-station for imaging, electron-and ion-spectroscopy, and pump–probe experiments at the FLASH free-electron laser”. In: *Journal of synchrotron radiation* 25.5 (2018), pp. 1529–1540. DOI: 10.1107/S1600577518008585

[Fan+15] Tingting Fan et al. “Bright circularly polarized soft X-ray high harmonics for X-ray magnetic circular dichroism”. In: *Proceedings of the National Academy of Sciences* 112.46 (2015), pp. 14206–14211. DOI: 10.1073/pnas.1519666112

[FD18] Chao Feng and Hai-Xiao Deng. “Review of fully coherent free-electron lasers”. In: *Nuclear Science and Techniques* 29.11 (2018), pp. 1–15. DOI: 10.1007/s41365-018-0490-1

[Fee+17a] James S Feehan, Jonathan HV Price, Thomas J Butcher, William S Brocklesby, Jeremy G Frey, and David J Richardson. "Efficient high-harmonic generation from a stable and compact ultrafast Yb-fiber laser producing 100 μJ, 350 fs pulses based on bendable photonic crystal fiber". In: *Applied Physics B* 123.1 (2017), p. 43. DOI: 10.1007/s00340-016-6620-8

[Fen+20] Tianli Feng, Anke Heilmann, Martin Bock, Lutz Ehrentraut, Tobias Witting, Haohai Yu, Holger Stiel, Stefan Eisebitt, and Matthias Schnürer. "27 W 2.1 μm OPCPA system for coherent soft X-ray generation operating at 10 kHz". In: *Opt. Express* 28.6 (Mar. 2020), pp. 8724–8733. DOI: 10.1364/OE.386588

[Fer+16] Eugenio Ferrari, Carlo Spezzani, Franck Fortuna, Renaud Delaunay, Franck Vidal, Ivaylo Nikolov, Paolo Cinquegrana, Bruno Diviacco, David Gauthier, Giuseppe Penco, et al. "Widely tunable two-colour seeded free-electron laser source for resonant-pump resonant-probe magnetic scattering". In: *Nature Communications* 7.1 (2016), pp. 1–8. DOI: 10.1038/ncomms10343

[Fer+88] M Ferray, A L'Huillier, X F Li, L A Lompre, G Mainfray, and C Manus. "Multiple-harmonic conversion of 1064 nm radiation in rare gases". In: *Journal of Physics B: Atomic, Molecular and Optical Physics* 21.3 (Feb. 1988), pp. L31–L35. DOI: 10.1088/0953-4075/21/3/001

[Fle+14] Avner Fleischer, Ofer Kfir, Tzvi Diskin, Pavel Sidorenko, and Oren Cohen. "Spin angular momentum and tunable polarization in high-harmonic generation". In: *Nature Photonics* 8.7 (2014), pp. 543–549. DOI: 10.1038/nphoton.2014.108

[FMS08] M. V. Frolov, N. L. Manakov, and Anthony F. Starace. "Wavelength Scaling of High-Harmonic Yield: Threshold Phenomena and Bound State Symmetry Dependence". In: *Phys. Rev. Lett.* 100 (17 May 2008), p. 173001. DOI: 10.1103/PhysRevLett.100.173001

[FPA+16] B Faatz, E Plönjes, S Ackermann, et al. "Simultaneous operation of two soft x-ray free-electron lasers driven by one linear accelerator". In: *New Journal of Physics* 18.6 (June 2016), p. 062002. DOI: 10.1088/1367-2630/18/6/062002

[FT92] Gy. Farkas and Cs. Tóth. "Proposal for attosecond light pulse generation using laser induced multiple-harmonic conversion pro-

cesses in rare gases". In: *Physics Letters A* 168.5 (1992), pp. 447–450. DOI: 10.1016/0375-9601(92)90534-S

[Fu+20] Yuxi Fu, Kotaro Nishimura, Renzhi Shao, Akira Suda, Katsumi Midorikawa, Pengfei Lan, and Eiji J Takahashi. "High efficiency ultrafast water-window harmonic generation for single-shot soft X-ray spectroscopy". In: *Communications Physics* 3.1 (2020), pp. 1–10. DOI: 10.1038/s42005-020-0355-x

[FW01] Simin Feng and Herbert G. Winful. "Physical origin of the Gouy phase shift". In: *Opt. Lett.* 26.8 (Apr. 2001), pp. 485–487. DOI: 10.1364/OL.26.000485

[Gan+20] Rashid A Ganeev, Ganjaboy S Boltaev, Sergey Y Stremoukhov, Vyacheslav V Kim, Anatoly V Andreev, and Ali S Alnaser. "High-order harmonic generation during different overlaps of two-colored pulses in laser-produced plasmas and gases". In: *The European Physical Journal D* 74.10 (2020), pp. 1–9. DOI: 10.1140/epjd/e2020-10176-6

[Gar+17] Dennis F Gardner, Michael Tanksalvala, Elisabeth R Shanblatt, Xiaoshi Zhang, Benjamin R Galloway, Christina L Porter, Robert Karl Jr, Charles Bevis, Daniel E Adams, Henry C Kapteyn, et al. "Subwavelength coherent imaging of periodic samples using a 13.5 nm tabletop high-harmonic light source". In: *Nature Photonics* 11.4 (2017), pp. 259–263. DOI: 10.1038/nphoton.2017.33

[Gib+03] Emily A. Gibson et al. "Coherent Soft X-ray Generation in the Water Window with Quasi-Phase Matching". In: *Science* 302.5642 (2003), pp. 95–98. DOI: 10.1126/science.1088654

[Gmb16] VACOM Vakuum Komponenten & Messtechnik GmbH. "Outgassing Rates of Aluminum compared to Stainless Steel". In: *White Paper WP00002 Rev. A* (2016)

[Goh+05] Christoph Gohle, Thomas Udem, Maximilian Herrmann, Jens Rauschenberger, Ronald Holzwarth, Hans A Schuessler, Ferenc Krausz, and Theodor W Hänsch. "A frequency comb in the extreme ultraviolet". In: *Nature* 436.7048 (2005), pp. 234–237. DOI: 10.1038/nature03851

[Goh+15] S.J. Goh, H.J.M. Bastiaens, B Vratzov, Q. Huang, F. Bijkerk, and K.J. Boller. "Fabrication and characterization of free-standing, high-line-density transmission gratings for the vacuum UV to soft

X-ray range". In: *Opt. Express* 23.4 (Feb. 2015), pp. 4421–4434. DOI: 10.1364/OE.23.004421

[GR19] Shambhu Ghimire and David A Reis. "High-harmonic generation from solids". In: *Nature physics* 15.1 (2019), pp. 10–16. DOI: 10.1038/s41567-018-0315-5

[Gre+20] Christian Grebing, Michael Müller, Joachim Buldt, Henning Stark, and Jens Limpert. "Kilowatt-average-power compression of millijoule pulses in a gas-filled multi-pass cell". In: *Opt. Lett.* 45.22 (Nov. 2020), pp. 6250–6253. DOI: 10.1364/OL.408998

[GS02] Mette B Gaarde and Kenneth J Schafer. "Quantum path distributions for high-order harmonics in rare gas atoms". In: *Physical Review A* 65.3 (2002), p. 031406. DOI: 10.1103/PhysRevA.65.031406

[GTS08] Mette B Gaarde, Jennifer L Tate, and Kenneth J Schafer. "Macroscopic aspects of attosecond pulse generation". In: *Journal of Physics B: Atomic, Molecular and Optical Physics* 41.13 (June 2008), p. 132001. DOI: 10.1088/0953-4075/41/13/132001

[GZB16] Zhong Guan, Xiao-Xin Zhou, and Xue-Bin Bian. "High-order-harmonic generation from periodic potentials driven by few-cycle laser pulses". In: *Physical Review A* 93.3 (2016), p. 033852. DOI: 10.1103/PhysRevA.83.021405

[Häd+10] S Hädrich, J Rothhardt, M Krebs, F Tavella, A Willner, J Limpert, and A Tünnermann. "High harmonic generation by novel fiber amplifier based sources". In: *Optics express* 18.19 (2010), pp. 20242–20250. DOI: 10.1364/OE.18.020242

[Har+17a] Anne Harth et al. "Compact 200 kHz HHG source driven by a few-cycle OPCPA". In: *Journal of Optics* 20.1 (Dec. 2017), p. 014007. DOI: 10.1088/2040-8986/aa9b04

[Hen+01] M Hentschel, R Kienberger, Ch Spielmann, Georg A Reider, N Milosevic, Thomas Brabec, Paul Corkum, Ulrich Heinzmann, Markus Drescher, and Ferenc Krausz. "Attosecond metrology". In: *Nature* 414.6863 (2001), pp. 509–513. DOI: 10.1038/35107000

[Her+02] J.-F. Hergott, M. Kovacev, H. Merdji, C. Hubert, Y. Mairesse, E. Jean, P. Breger, P. Agostini, B. Carré, and P. Salières. "Extreme-ultraviolet high-order harmonic pulses in the microjoule range". In: *Phys. Rev. A* 66 (2 Aug. 2002), p. 021801. DOI: 10.1103/PhysRevA.66.021801

[Hey+12] CM Heyl, J Güdde, Anne L'Huillier, and U Höfer. "High-order harmonic generation with μJ laser pulses at high repetition rates". In: *Journal of Physics B: Atomic, Molecular and Optical Physics* 45.7 (2012), p. 074020. DOI: 10.1088/0953-4075/45/7/074020

[Hey+16a] C M Heyl, C L Arnold, A Couairon, and A L'Huillier. "Introduction to macroscopic power scaling principles for high-order harmonic generation". In: *Journal of Physics B: Atomic, Molecular and Optical Physics* 50.1 (Dec. 2016), p. 013001. DOI: 10.1088/1361-6455/50/1/013001

[Hey+16b] C. M. Heyl et al. "Scale-invariant nonlinear optics in gases". In: *Optica* 3.1 (Jan. 2016), pp. 75–81. DOI: 10.1364/OPTICA.3.000075

[Hey+18] CM Heyl, SB Schoun, G Porat, H Green, and J Ye. "A nozzle for high-density supersonic gas jets at elevated temperatures". In: *Review of Scientific Instruments* 89.11 (2018), p. 113114. DOI: 10.1063/1.5051586

[HGD93] B.L. Henke, E.M. Gullikson, and J.C. Davis. "X-ray interactions: Photoabsorption, scattering, transmission, and reflection at E = 50-30,000 eV, Z = 1-92". In: *Atomic Data and Nuclear Data Tables; (United States)* 54.2 (July 1993). DOI: 10.1006/adnd.1993.1013

[Hil+20b] Vinzenz Hilbert, Maxim Tschernajew, Robert Klas, Jens Limpert, and Jan Rothhardt. "A compact, turnkey, narrow-bandwidth, tunable, and high-photon-flux extreme ultraviolet source". In: *AIP Advances* 10.4 (2020), p. 045227. DOI: 10.1063/1.5133154

[HK00] Zhirong Huang and Kwang-Je Kim. "Three-dimensional analysis of harmonic generation in high-gain free-electron lasers". In: *Phys. Rev. E* 62 (5 Nov. 2000), pp. 7295–7308. DOI: 10.1103/PhysRevE.62.7295

[HK07] Zhirong Huang and Kwang-Je Kim. "Review of x-ray free-electron laser theory". In: *Phys. Rev. ST Accel. Beams* 10 (3 Mar. 2007), p. 034801. DOI: 10.1103/PhysRevSTAB.10.034801

[HL12] Zhirong Huang and Ingolf Lindau. "SACLA hard-X-ray compact FEL". In: *Nature Photonics* 6.8 (2012), pp. 505–506. DOI: 10.1038/nphoton.2012.184

[HMH93] S.E. Harris, J.J. Macklin, and T.W. Hänsch. "Atomic scale temporal structure inherent to high-order harmonic generation". In:

Optics Communications 100.5 (1993), pp. 487–490. DOI: 10.1016/0030-4018(93)90250-9

[Hög+19] Maximilian Högner, Tobias Saule, Stephan Heinrich, Nikolai Lilienfein, Dominik Esser, Michael Trubetskov, Volodymyr Pervak, and Ioachim Pupeza. "Cavity-enhanced noncollinear high-harmonic generation". In: *Optics express* 27.14 (2019), pp. 19675–19691. DOI: 10.1364/OE.27.019675

[Hol+16] Marcel Holtz, Christoph Hauf, Antonio-Andres Hernández Salvador, Rene Costard, Michael Woerner, and Thomas Elsaesser. "Shift-current-induced strain waves in $LiNbO_3$ mapped by femtosecond x-ray diffraction". In: *Phys. Rev. B* 94 (10 Sept. 2016), p. 104302. DOI: 10.1103/PhysRevB.94.104302

[HSB20] Liran Hareli, Georgiy Shoulga, and Alon Bahabad. "Phase matching and quasi-phase matching of high-order harmonic generation-a tutorial". In: *Journal of Physics B: Atomic, Molecular and Optical Physics* (2020). DOI: 10.1088/1361-6455/abb937

[Hua+18] Pei-Chi Huang, Carlos Hernández-Garcı
a, Jen-Ting Huang, Po-Yao Huang, Chih-Hsuan Lu, Laura Rego, Daniel D Hickstein, Jennifer L Ellis, Agnieszka Jaron-Becker, Andreas Becker, et al. "Polarization control of isolated high-harmonic pulses". In: *Nature Photonics* 12.6 (2018), pp. 349–354. DOI: 10.1038/s41566-018-0145-0

[HZS19] T Helk, Michael Zürch, and C Spielmann. "Perspective: Towards single shot time-resolved microscopy using short wavelength table-top light sources". In: *Structural Dynamics* 6.1 (2019), p. 010902. DOI: 10.1063/1.5082686

[Iri+20] Akinori Irizawa et al. "Spatially Resolved Spectral Imaging by A THz-FEL". In: *Condensed Matter* 5.2 (2020). DOI: 10.3390/condmat5020038

[Ish+12] Tetsuya Ishikawa, Hideki Aoyagi, Takao Asaka, Yoshihiro Asano, Noriyoshi Azumi, Teruhiko Bizen, Hiroyasu Ego, Kenji Fukami, Toru Fukui, Yukito Furukawa, et al. "A compact X-ray free-electron laser emitting in the sub-ångström region". In: *nature photonics* 6.8 (2012), pp. 540–544. DOI: 10.1038/nphoton.2012.141

[Jon+05] R Jason Jones, Kevin D Moll, Michael J Thorpe, and Jun Ye. "Phase-coherent frequency combs in the vacuum ultraviolet via high-harmonic generation inside a femtosecond enhancement cav-

ity". In: *Physical Review Letters* 94.19 (2005), p. 193201. DOI: 10.1103/PhysRevLett.94.193201

[JY02] R Jason Jones and Jun Ye. "Femtosecond pulse amplification by coherent addition in a passive optical cavity". In: *Optics letters* 27.20 (2002), pp. 1848–1850. DOI: 10.1364/OL.27.001848

[Kan+17] Heung-Sik Kang, Chang-Ki Min, Hoon Heo, Changbum Kim, Haeryong Yang, Gyujin Kim, Inhyuk Nam, Soung Youl Baek, Hyo-Jin Choi, Geonyeong Mun, et al. "Hard X-ray free-electron laser with femtosecond-scale timing jitter". In: *Nature Photonics* 11.11 (2017), pp. 708–713. DOI: 10.1038/s41566-017-0029-8

[Kan+20a] Natsuki Kanda, Tomohiro Imahoko, Koji Yoshida, Akihiro Tanabashi, A Amani Eilanlou, Yasuo Nabekawa, Tetsumi Sumiyoshi, Makoto Kuwata-Gonokami, and Katsumi Midorikawa. "Opening a new route to multiport coherent XUV sources via intracavity high-order harmonic generation". In: *Light: Science & Applications* 9.1 (2020), pp. 1–9. DOI: 10.1038/s41377-020-00405-5

[Kan+95] C. Kan, C. E. Capjack, R. Rankin, and N. H. Burnett. "Spectral and temporal structure in high harmonic emission from ionizing atomic gases". In: *Phys. Rev. A* 52 (6 Dec. 1995), R4336–R4339. DOI: 10.1103/PhysRevA.52.R4336

[Kas+20] Gregor Kastirke et al. "Photoelectron Diffraction Imaging of a Molecular Breakup Using an X-Ray Free-Electron Laser". In: *Phys. Rev. X* 10 (2 June 2020), p. 021052. DOI: 10.1103/PhysRevX.10.021052

[Kaz+03] S. Kazamias, D. Douillet, F. Weihe, C. Valentin, A. Rousse, S. Sebban, G. Grillon, F. Augé, D. Hulin, and Ph. Balcou. "Global Optimization of High Harmonic Generation". In: *Phys. Rev. Lett.* 90 (19 May 2003), p. 193901. DOI: 10.1103/PhysRevLett.90.193901

[Kim+14] Takashi Kimura, Yasumasa Joti, Akemi Shibuya, Changyong Song, Sangsoo Kim, Kensuke Tono, Makina Yabashi, Masatada Tamakoshi, Toshiyuki Moriya, Tairo Oshima, et al. "Imaging live cell in micro-liquid enclosure by X-ray laser diffraction". In: *Nature communications* 5.1 (2014), pp. 1–7. DOI: 10.1038/ncomms4052

[Kla+20b] Robert Klas, Joachim Buldt, Henning Stark, Alexander Kirsche, Martin Gebhardt, Jan Rothhardt, and Jens Limpert. "Sub-20 fs high-energy pulse generation at 515 nm with 50 W of average

power". In: *Laser Congress 2020 (ASSL, LAC)*. Optical Society of America, 2020, AF3A.4. DOI: 10.1364/ASSL.2020.AF3A.4

[Ko+17] In Ko, Heung-Sik Kang, Hoon Heo, Changbum Kim, Gyujin Kim, Chang-Ki Min, Haeryong Yang, Soung Baek, Hyo-Jin Choi, Geonyeong Mun, et al. "Construction and commissioning of PAL-XFEL facility". In: *Applied Sciences* 7.5 (2017), p. 479. DOI: 10.3390/app7050479

[Kov+12] Katalin Kovács, Emeric Balogh, János Hebling, Valer Toşa, and Katalin Varjú. "Quasi-Phase-Matching High-Harmonic Radiation Using Chirped THz Pulses". In: *Phys. Rev. Lett.* 108 (19 May 2012), p. 193903. DOI: 10.1103/PhysRevLett.108.193903

[KP14] Alan Kastengren and Christopher F Powell. "Synchrotron X-ray techniques for fluid dynamics". In: *Experiments in fluids* 55.3 (2014), pp. 1–15. DOI: 10.1007/s00348-014-1686-8

[Kra+18] Peter M Kraus, Michael Zürch, Scott K Cushing, Daniel M Neumark, and Stephen R Leone. "The ultrafast X-ray spectroscopic revolution in chemical dynamics". In: *Nature Reviews Chemistry* 2.6 (2018), pp. 82–94. DOI: 10.1038/s41570-018-0008-8

[Kre+13] Martin Kretschmar, Carlos Hernández-Garcıá, Daniel S. Steingrube, Luis Plaja, Uwe Morgner, and Milutin Kovačev. "Spatial contributions of electron trajectories to high-order-harmonic radiation originating from a semi-infinite gas cell". In: *Phys. Rev. A* 88 (1 July 2013), p. 013805. DOI: 10.1103/PhysRevA.88.013805

[KS80] AM Kondratenko and EL Saldin. "Generating of coherent radiation by a relativistic electron beam in an ondulator". In: *Part. Accel.* 10 (1980), pp. 207–216

[KSK92] Jeffrey L Krause, Kenneth J Schafer, and Kenneth C Kulander. "High-order harmonic generation from atoms and ions in the high intensity regime". In: *Physical Review Letters* 68.24 (1992), p. 3535. DOI: 10.1103/PhysRevLett.68.3535

[KTK19] Shota Kimura, Shuntaro Tani, and Yohei Kobayashi. "Kerr-lens mode locking above a 20 GHz repetition rate". In: *Optica* 6.5 (May 2019), pp. 532–533. DOI: 10.1364/OPTICA.6.000532

[Küh+17] Sergei Kühn et al. "The ELI-ALPS facility: the next generation of attosecond sources". In: *Journal of Physics B: Atomic, Molecular and Optical Physics* 50.13 (June 2017), p. 132002. DOI: 10.1088/1361-6455/aa6ee8

[Kur+13] Heiko G. Kurz, Daniel S. Steingrube, Detlev Ristau, Manfred Lein, Uwe Morgner, and Milutin Kovačev. "High-order-harmonic generation from dense water microdroplets". In: *Phys. Rev. A* 87 (6 June 2013), p. 063811. DOI: 10.1103/PhysRevA.87.063811

[Lab+19] F. Labaye, M. Gaponenko, N. Modsching, P. Brochard, C. Paradis, S. Schilt, V. J. Wittwer, and T. Südmeyer. "XUV Sources Based on Intra-Oscillator High Harmonic Generation With Thin-Disk Lasers: Current Status and Prospects". In: *IEEE Journal of Selected Topics in Quantum Electronics* 25.4 (2019), pp. 1–19. DOI: 10.1109/JSTQE.2019.2926024

[Lai+15] Chien-Jen Lai et al. "Multi-mJ mid-infrared kHz OPCPA and Yb-doped pump lasers for tabletop coherent soft x-ray generation". In: *Journal of Optics* 17.9 (Sept. 2015), p. 094009. DOI: 10.1088/2040-8978/17/9/094009

[Lam+09] G. Lambert, T. Hara, M. Labat, T. Tanikawa, Y. Tanaka, M. Yabashi, D. Garzella, B. Carré, and M. E. Couprie. "Seed level requirement for improving the temporal coherence of a Free-Electron Laser". In: *EPL (Europhysics Letters)* 88.5 (Dec. 2009), p. 54002. DOI: 10.1209/0295-5075/88/54002

[Lan+19] T. Lang et al. "Versatile OPCPA Pump-Probe Laser System for the FLASH2 XUV FEL Beamline at DESY". In: *2019 Conference on Lasers and Electro-Optics Europe European Quantum Electronics Conference (CLEO/Europe-EQEC)*. June 2019, pp. 1–1. DOI: 10.1109/CLEOE-EQEC.2019.8871596

[Lew+94] M. Lewenstein, Ph. Balcou, M. Yu. Ivanov, Anne L'Huillier, and P. B. Corkum. "Theory of high-harmonic generation by low-frequency laser fields". In: *Phys. Rev. A* 49 (3 Mar. 1994), pp. 2117–2132. DOI: 10.1103/PhysRevA.49.2117

[Li+20] Jie Li, Jian Lu, Andrew Chew, Seunghwoi Han, Jialin Li, Yi Wu, He Wang, Shambhu Ghimire, and Zenghu Chang. "Attosecond science based on high harmonic generation from gases and solids". In: *Nature Communications* 11.1 (2020), pp. 1–13. DOI: 10.1038/s41467-020-16480-6

[Lia21] Sharon G. Lias. "Ionization Energy Evaluation". In: *NIST Chemistry WebBook, NIST Standard Reference Database Number 69* (retrieved April 2021). DOI: 10.18434/T4D303

[Lim+06] J. Limpert, F. Roser, T. Schreiber, and A. Tunnermann. "High-power ultrafast fiber laser systems". In: *IEEE Journal of Selected Topics in Quantum Electronics* 12.2 (2006), pp. 233–244. DOI: 10.1109/JSTQE.2006.872729

[LNM20] Yu-Chieh Lin, Yasuo Nabekawa, and Katsumi Midorikawa. "Optical parametric amplification of sub-cycle shortwave infrared pulses". In: *Nature communications* 11.1 (2020), pp. 1–14. DOI: 10.1038/s41467-020-17247-9

[LSL95] Maciej Lewenstein, Pascal Salières, and Anne L'Huillier. "Phase of the atomic polarization in high-order harmonic generation". In: *Phys. Rev. A* 52 (6 Dec. 1995), pp. 4747–4754. DOI: 10.1103/PhysRevA.52.4747

[Luu+18] Tran Trung Luu, Zhong Yin, Arohi Jain, Thomas Gaumnitz, Yoann Pertot, Jun Ma, and Hans Jakob Wörner. "Extreme–ultraviolet high–harmonic generation in liquids". In: *Nature communications* 9.1 (2018), pp. 1–10. DOI: 10.1038/s41467-018-06040-4

[Mad71] John MJ Madey. "Stimulated emission of bremsstrahlung in a periodic magnetic field". In: *Journal of Applied Physics* 42.5 (1971), pp. 1906–1913. DOI: 10.1063/1.1660466

[Mag+12] M. Magrakvelidze et al. "Tracing nuclear-wave-packet dynamics in singly and doubly charged states of N_2 and O_2 with XUV-pump–XUV-probe experiments". In: *Phys. Rev. A* 86 (1 July 2012), p. 013415. DOI: 10.1103/PhysRevA.86.013415

[Mak+20] Ioannis Makos, I Orfanos, Arjun Nayak, Jasper Peschel, Balázs Major, Ioannis Liontos, Emmanuel Skantzakis, N Papadakis, Constantinos Kalpouzos, Mathieu Dumergue, et al. "A 10-gigawatt attosecond source for non-linear XUV optics and XUV-pump-XUV-probe studies". In: *Scientific reports* 10.1 (2020), pp. 1–18. DOI: 10.1038/s41598-020-60331-9

[Mar+82] Christel M. Marian, Ralf Marian, Sigrid D. Peyerimhoff, Bernd A. Hess, Robert J. Buenker, and Georg Seger. "Ab initio CI calculation of $O2^+$ predissociation phenomena induced by a spin-orbit coupling mechanism". In: *Molecular Physics* 46.4 (1982), pp. 779–810. DOI: 10.1080/00268978200101591

[MBM16] Settimio Mobilio, Federico Boscherini, and Carlo Meneghini. *Synchrotron Radiation*. Springer, 2016. DOI: 10.1007/978-3-642-55315-8

[McN09] Brian McNeil. "First light from hard X-ray laser". In: *Nature Photonics* 3.7 (2009), pp. 375–377. DOI: 10.1038/nphoton.2009.110

[McP+87] A. McPherson, G. Gibson, H. Jara, U. Johann, T. S. Luk, I. A. McIntyre, K. Boyer, and C. K. Rhodes. "Studies of multiphoton production of vacuum-ultraviolet radiation in the rare gases". In: *J. Opt. Soc. Am. B* 4.4 (Apr. 1987), pp. 595–601. DOI: 10.1364/JOSAB.4.000595

[Mei+20] Severin Meister, Hannes Lindenblatt, Florian Trost, Kirsten Schnorr, Sven Augustin, Markus Braune, Rolf Treusch, Thomas Pfeifer, and Robert Moshammer. "Atomic, Molecular and Cluster Science with the Reaction Microscope Endstation at FLASH2". In: *Applied Sciences* 10.8 (2020), p. 2953. DOI: 10.3390/app10082953

[Mia+15] Jianwei Miao, Tetsuya Ishikawa, Ian K. Robinson, and Margaret M. Murnane. "Beyond crystallography: Diffractive imaging using coherent x-ray light sources". In: *Science* 348.6234 (2015), pp. 530–535. DOI: 10.1126/science.aaa1394

[Mil+05] DM Mills, JR Helliwell, Å Kvick, T Ohta, IA Robinson, and A Authier. "Report of the Working Group on Synchrotron Radiation Nomenclature–brightness, spectral brightness or brilliance?" In: *Journal of synchrotron radiation* 12.3 (2005), pp. 385–385. DOI: 10.1107/S090904950500796X

[Mil+17] Christopher Milne, Thomas Schietinger, Masamitsu Aiba, Arturo Alarcon, Jürgen Alex, Alexander Anghel, Vladimir Arsov, Carl Beard, Paul Beaud, Simona Bettoni, et al. "SwissFEL: the Swiss X-ray free electron laser". In: *Applied Sciences* 7.7 (2017), p. 720. DOI: 10.3390/app7070720

[Mil88] DR Miller. *Free Jet Sources, Atomic and Molecular Beam Methods*. 1988

[MNS08] Katsumi Midorikawa, Yasuo Nabekawa, and Akira Suda. "XUV multiphoton processes with intense high-order harmonics". In: *Progress in Quantum Electronics* 32.2 (2008), pp. 43–88. DOI: 10.1016/j.pquantelec.2008.04.001

[Mos+96] R. Moshammer, M. Unverzagt, W. Schmitt, J. Ullrich, and H. Schmidt-Böcking. "A 4π recoil-ion electron momentum analyzer:

a high-resolution "microscope" for the investigation of the dynamics of atomic, molecular and nuclear reactions". In: *Nuclear Instruments and Methods in Physics Research Section B: Beam Interactions with Materials and Atoms* 108.4 (1996), pp. 425–445. DOI: 10.1016/0168-583X(95)01259-1

[Mou86] P. F. Moulton. "Spectroscopic and laser characteristics of Ti:Al2O3". In: *J. Opt. Soc. Am. B* 3.1 (Jan. 1986), pp. 125–133. DOI: 10.1364/JOSAB.3.000125

[MS20] Robert Moshammer and Kirsten Schnorr. "Molecular Physics and Gas-Phase Chemistry with Free-Electron Lasers". In: *Synchrotron Light Sources and Free-Electron Lasers: Accelerator Physics, Instrumentation and Science Applications* (2020), pp. 1493–1524. DOI: 10.1007%2F978-3-030-23201-6_26

[MS92] Kenzo Miyazaki and Hirofumi Sakai. "High-order harmonic generation in rare gases with intense subpicosecond dye laser pulses". In: *Journal of Physics B: Atomic, Molecular and Optical Physics* 25.3 (1992), p. L83. DOI: 10.1088/0953-4075/25/3/006

[MSS12] J. Miao, R. L. Sandberg, and C. Song. "Coherent X-Ray Diffraction Imaging". In: *IEEE Journal of Selected Topics in Quantum Electronics* 18.1 (2012), pp. 399–410. DOI: 10.1109/JSTQE.2011.2157306

[Nam+18] Inhyuk Nam, Chang-Ki Min, Changbum Kim, Haeryong Yang, Gyujin Kim, Hoon Heo, Soonnam Kwon, Sang Han Park, and Heung-Sik Kang. "Soft X-ray harmonic lasing self-seeded free electron laser at Pohang Accelerator Laboratory X-ray free electron laser". In: *Applied Physics Letters* 112.21 (2018), p. 213506. DOI: 10.1063/1.5030443

[Nol+09] Tino Noll, Karsten Holldack, Gerd Reichardt, Olaf Schwarzkopf, and Thomas Zeschke. "Parallel kinematics for nanoscale Cartesian motions". In: *Precision Engineering* 33.3 (2009), pp. 291–304. DOI: 10.1016/j.precisioneng.2008.07.001

[Owa+18] Shigeki Owada et al. "A soft X-ray free-electron laser beamline at SACLA: the light source, photon beamline and experimental station". In: *Journal of Synchrotron Radiation* 25.1 (Jan. 2018), pp. 282–288. DOI: 10.1107/S1600577517015685

[Pap+01] Nektarios Andrea Papadogiannis, C Kalpouzos, E Goulielmakis, G Nersisyan, D Charalambidis, F Augé, F Weihe, and Ph Balcou.

"Kilohertz extreme-ultraviolet light source based on femtosecond high-order harmonic generation from noble gases". In: *Applied Physics B* 73.7 (2001), pp. 687–692. DOI: 10.1007/s003400100734

[Par+18] Sang Han Park, Minseok Kim, Changi-Ki Min, Intae Eom, Inhyuk Nam, Heung-Soo Lee, Heung-Sik Kang, Hyeong-Do Kim, Ho Young Jang, Seonghan Kim, et al. "PAL-XFEL soft X-ray scientific instruments and X-ray optics: First commissioning results". In: *Review of Scientific Instruments* 89.5 (2018), p. 055105. DOI: 10.1063/1.5023557

[Pau+01] P. M. Paul, E. S. Toma, P. Breger, G. Mullot, F. Augé, Ph. Balcou, H. G. Muller, and P. Agostini. "Observation of a Train of Attosecond Pulses from High Harmonic Generation". In: *Science* 292.5522 (2001), pp. 1689–1692. DOI: 10.1126/science.1059413

[PE20] Bastian Pfau and Stefan Eisebitt. "X-Ray holography". In: *Synchrotron Light Sources and Free-Electron Lasers: Accelerator Physics, Instrumentation and Science Applications* (2020), pp. 1295–1335. DOI: 10.1007%2F978-3-030-23201-6_28

[PH19] Nathalie Picqué and Theodor W Hänsch. "Frequency comb spectroscopy". In: *Nature Photonics* 13.3 (2019), pp. 146–157. DOI: 10.1038/s41566-018-0347-5

[PHZ94] S. Pedersen, J. L. Herek, and A. H. Zewail. "The Validity of the "Diradical" Hypothesis: Direct Femtoscond Studies of the Transition-State Structures". In: *Science* 266.5189 (1994), pp. 1359–1364. DOI: 10.1126/science.266.5189.1359

[PMV19] Peng Peng, Claude Marceau, and David M Villeneuve. "Attosecond imaging of molecules using high harmonic spectroscopy". In: *Nature Reviews Physics* 1.2 (2019), pp. 144–155. DOI: 10.1038/s42254-018-0015-1

[Pop+09a] Tenio Popmintchev, Ming-Chang Chen, Alon Bahabad, Michael Gerrity, Pavel Sidorenko, Oren Cohen, Ivan P. Christov, Margaret M. Murnane, and Henry C. Kapteyn. "Phase matching of high harmonic generation in the soft and hard X-ray regions of the spectrum". In: *Proceedings of the National Academy of Sciences* 106.26 (2009), pp. 10516–10521. DOI: 10.1073/pnas.0903748106

[Pop+09b] Tenio Popmintchev, Ming-Chang Chen, Alon Bahabad, Michael Gerrity, Pavel Sidorenko, Oren Cohen, Ivan P Christov, Margaret M Murnane, and Henry C Kapteyn. "Phase matching of high

harmonic generation in the soft and hard X-ray regions of the spectrum". In: *Proceedings of the National Academy of Sciences* 106.26 (2009), pp. 10516–10521. DOI: 10.1073/pnas.0903748106

[Pop+12] Tenio Popmintchev et al. "Bright Coherent Ultrahigh Harmonics in the keV X-ray Regime from Mid-Infrared Femtosecond Lasers". In: *Science* 336.6086 (2012), pp. 1287–1291. DOI: 10.1126/science.1218497

[Pop04] Vladimir S Popov. "Tunnel and multiphoton ionization of atoms and ions in a strong laser field (Keldysh theory)". In: *Physics-Uspekhi* 47.9 (2004), p. 855. DOI: 10.1070/PU2004v047n09ABEH001812

[Pra+20] Eduard Prat, Rafael Abela, Masamitsu Aiba, Arturo Alarcon, Jürgen Alex, Yunieski Arbelo, Christopher Arrell, Vladimir Arsov, Camila Bacellar, Carl Beard, et al. "A compact and cost-effective hard x-ray free-electron laser driven by a high-brightness and low-energy electron beam". In: *Nature Photonics* 14.12 (2020), pp. 748–754. DOI: 10.1038/s41566-020-00712-8

[PSG06] T Pfeifer, C Spielmann, and G Gerber. "Femtosecond x-ray science". In: *Reports on Progress in Physics* 69.2 (Jan. 2006), pp. 443–505. DOI: 10.1088/0034-4885/69/2/r04

[Pup+21] Ioachim Pupeza, Chuankun Zhang, Maximilian Högner, and Jun Ye. "Extreme-ultraviolet frequency combs for precision metrology and attosecond science". In: *Nature Photonics* (2021), pp. 1–12. DOI: 10.1038/s41566-020-00741-3

[Red+11] H. Redlin, A. Al-Shemmary, A. Azima, N. Stojanovic, F. Tavella, I. Will, and S. Düsterer. "The FLASH pump–probe laser system: Setup, characterization and optical beamlines". In: *Nuclear Instruments and Methods in Physics Research Section A: Accelerators, Spectrometers, Detectors and Associated Equipment* 635.1, Supplement (2011). PhotonDiag 2010, S88–S93. DOI: 10.1016/j.nima.2010.09.159

[Red+15] Maurizio Reduzzi et al. "Advances in high-order harmonic generation sources for time-resolved investigations". In: *Journal of Electron Spectroscopy and Related Phenomena* 204 (2015). Gas phase spectroscopic and dynamical studies at Free-Electron Lasers and other short wavelength sources, pp. 257–268. DOI: 10.1016/j.elspec.2015.09.002

[Röh+19] R. Röhlsberger, C. G. Schroer, R. Wanzenberg, S. Klumpp, and W. Wurth. "Light Source Upgrades at DESY: PETRA IV and FLASH2020+". In: *Synchrotron Radiation News* 32.1 (2019), pp. 27–31. DOI: 10.1080/08940886.2019.1559605

[Rot+14c] Jan Rothhardt, Manuel Krebs, Steffen Hädrich, Stefan Demmler, Jens Limpert, and Andreas Tünnermann. "Absorption-limited and phase-matched high harmonic generation in the tight focusing regime". In: *New Journal of Physics* 16.3 (Mar. 2014), p. 033022. DOI: 10.1088/1367-2630/16/3/033022

[RR15] Artem Rudenko and Daniel Rolles. "Time-resolved studies with FELs". In: *Journal of Electron Spectroscopy and Related Phenomena* 204 (2015). Gas phase spectroscopic and dynamical studies at Free-Electron Lasers and other short wavelength sources, pp. 228–236. DOI: 10.1016/j.elspec.2015.07.010

[RSW19] Jörg Rossbach, Jochen R. Schneider, and Wilfried Wurth. "10 years of pioneering X-ray science at the Free-Electron Laser FLASH at DESY". In: *Physics Reports* 808 (2019). 10 years of pioneering X-ray science at the Free-Electron Laser FLASH at DESY, pp. 1–74. DOI: 10.1016/j.physrep.2019.02.002

[Rud+13] Piotr Rudawski, CM Heyl, Fernando Brizuela, Jörg Schwenke, Anders Persson, Erik Mansten, Rafal Rakowski, Linnea Rading, Filippo Campi, Byunghoon Kim, et al. "A high-flux high-order harmonic source". In: *Review of Scientific Instruments* 84.7 (2013), p. 073103. DOI: 10.1063/1.4812266

[Run+98] Andy Rundquist, Charles G. Durfee, Zenghu Chang, Catherine Herne, Sterling Backus, Margaret M. Murnane, and Henry C. Kapteyn. "Phase-Matched Generation of Coherent Soft X-rays". In: *Science* 280.5368 (1998), pp. 1412–1415. DOI: 10.1126/science.280.5368.1412

[Rus+14] Peter Russbueldt, Dieter Hoffmann, Marco Höfer, Jens Löhring, Jörg Luttmann, Ansgar Meissner, Johannes Weitenberg, Martin Traub, Thomas Sartorius, Dominik Esser, et al. "Innoslab amplifiers". In: *IEEE Journal of Selected Topics in Quantum Electronics* 21.1 (2014), pp. 447–463. DOI: 10.1109/JSTQE.2014.2333234

[Sal+98] Pascal Salières, Philippe Antoine, Armelle de Bohan, and Maciej Lewenstein. "Temporal and Spectral Tailoring of High-Order

Harmonics". In: *Phys. Rev. Lett.* 81 (25 Dec. 1998), pp. 5544–5547. DOI: 10.1103/PhysRevLett.81.5544

[Sal+99] Pascal Salières, Anne L'Huillier, Philippe Antoine, and Maciej Lewenstein. "Study of The Spatial and Temporal Coherence of High-Order Harmonics". In: ed. by Benjamin Bederson and Herbert Walther. Vol. 41. Advances In Atomic, Molecular, and Optical Physics. Academic Press, 1999, pp. 83–142. DOI: 10.1016/S1049-250X(08)60219-0

[Sar+15] C. J. Saraceno, F. Emaury, C. Schriber, A. Diebold, M. Hoffmann, M. Golling, T. Südmeyer, and U. Keller. "Toward Millijoule-Level High-Power Ultrafast Thin-Disk Oscillators". In: *IEEE Journal of Selected Topics in Quantum Electronics* 21.1 (2015), pp. 106–123. DOI: 10.1109/JSTQE.2014.2341588

[Sar+19] Clara J Saraceno, Dirk Sutter, Thomas Metzger, and Marwan Abdou Ahmed. "The amazing progress of high-power ultrafast thin-disk lasers". In: *Journal of the European Optical Society-Rapid Publications* 15.1 (2019), pp. 1–7. DOI: 10.1186/s41476-019-0108-1

[Sav+17] Evgeny Savelyev, Rebecca Boll, Cédric Bomme, Nora Schirmel, Harald Redlin, Benjamin Erk, Stefan Düsterer, Erland Müller, Hauke Höppner, Sven Toleikis, et al. "Jitter-correction for IR/UV-XUV pump-probe experiments at the FLASH free-electron laser". In: *New Journal of Physics* 19.4 (2017), p. 043009. DOI: 10.1088/1367-2630/aa652d

[Say+21] Muhammed Sayrac, Alexandre A. Kolomenskii, Jian Dong, and Hans A. Schuessler. "Generation of even and odd harmonics in the XUV region with controlling the relative delay and polarization of two-color fields". In: *Optik* 226 (2021), p. 165966. DOI: 10.1016/j.ijleo.2020.165966

[Sch+00] R. W. Schoenlein, S. Chattopadhyay, H. H. W. Chong, T. E. Glover, P. A. Heimann, C. V. Shank, A. A. Zholents, and M. S. Zolotorev. "Generation of Femtosecond Pulses of Synchrotron Radiation". In: *Science* 287.5461 (2000), pp. 2237–2240. DOI: 10.1126/science.287.5461.2237

[Sch+07] K. Schiessl, K. L. Ishikawa, E. Persson, and J. Burgdörfer. "Quantum Path Interference in the Wavelength Dependence of High-

Harmonic Generation". In: *Phys. Rev. Lett.* 99 (25 Dec. 2007), p. 253903. DOI: 10.1103/PhysRevLett.99.253903

[Sch+15] Sebastian Schulz, Ivanka Grguraš, C Behrens, Hubertus Bromberger, JT Costello, MK Czwalinna, M Felber, MC Hoffmann, M Ilchen, HY Liu, et al. "Femtosecond all-optical synchronization of an X-ray free-electron laser". In: *Nature communications* 6 (2015), p. 5938. DOI: 10.1038/ncomms6938

[Sch+19a] N. Schirmel, S. Alisauskas, T. Huülsenbusch, B. Manschwetus, C. Mohr, L. Winkelmann, U. Große-Wortmann, J. Zheng, T. Lang, and I. Hartl. "Long-Term Stabilization of Temporal and Spectral Drifts of a Burst-Mode OPCPA System". In: *Conference on Lasers and Electro-Optics*. Optical Society of America, 2019, STu4E.4. DOI: 10.1364/CLEO_SI.2019.STu4E.4

[Sch+19c] Georg Schmid et al. "Reaction microscope endstation at FLASH2". In: *Journal of Synchrotron Radiation* 26.3 (May 2019), pp. 854–867. DOI: 10.1107/S1600577519002236

[Sch+19d] Robert Schoenlein, Thomas Elsaesser, Karsten Holldack, Zhirong Huang, Henry Kapteyn, Margaret Murnane, and Michael Woerner. "Recent advances in ultrafast X-ray sources". In: *Philosophical Transactions of the Royal Society A* 377.2145 (2019), p. 20180384. DOI: doi.org/10.1098/rsta.2018.0384

[Sch15] Peter Schwerdtfeger. "Table of experimental and calculated static dipole polarizabilities for the electronic ground states of the neutral elements (in atomic units)". In: *Centre for Theoretical Chemistry and Physics, Massey University* (2015)

[Sed+17] EA Seddon, JA Clarke, DJ Dunning, C Masciovecchio, CJ Milne, F Parmigiani, D Rugg, JCH Spence, NR Thompson, K Ueda, et al. "Short-wavelength free-electron laser sources and science: a review". In: *Reports on Progress in Physics* 80.11 (2017), p. 115901. DOI: 10.1088/1361-6633/aa7cca

[Ser+07] Jozsef Seres, VS Yakovlev, Enikő Seres, Ch Streli, Peter Wobrauschek, Ch Spielmann, and Ferenc Krausz. "Coherent superposition of laser-driven soft-X-ray harmonics from successive sources". In: *Nature Physics* 3.12 (2007), pp. 878–883. DOI: 10.1038/nphys775

[Shi+09] A. D. Shiner, C. Trallero-Herrero, N. Kajumba, H.-C. Bandulet, D. Comtois, F. Légaré, M. Giguère, J-C. Kieffer, P. B. Corkum,

and D. M. Villeneuve. “Wavelength Scaling of High Harmonic Generation Efficiency”. In: *Phys. Rev. Lett.* 103 (7 Aug. 2009), p. 073902. DOI: 10.1103/PhysRevLett.103.073902

[Sin+12] A. Singer et al. “Spatial and temporal coherence properties of single free-electron laser pulses”. In: *Opt. Express* 20.16 (July 2012), pp. 17480–17495. DOI: 10.1364/OE.20.017480

[SLL95] Pascal Salières, Anne L’Huillier, and Maciej Lewenstein. “Coherence Control of High-Order Harmonics”. In: *Phys. Rev. Lett.* 74 (19 May 1995), pp. 3776–3779. DOI: 10.1103/PhysRevLett.74.3776

[SM00] MS Smyth and JHJ Martin. “x Ray crystallography”. In: *Molecular Pathology* 53.1 (2000), p. 8. DOI: 10.1136/mp.53.1.8

[SM12] Ilme Schlichting and Jianwei Miao. “Emerging opportunities in structural biology with X-ray free-electron lasers”. In: *Current Opinion in Structural Biology* 22.5 (2012). Carbohydrates and glycoconjugates ? Biophysical methods, pp. 613–626. DOI: 10.1016/j.sbi.2012.07.015

[SM85] Donna Strickland and Gerard Mourou. “Compression of amplified chirped optical pulses”. In: *Optics communications* 55.6 (1985), pp. 447–449. DOI: 10.1016/0030-4018(85)90120-8

[SSY08] E.L. Saldin, E.A. Schneidmiller, and M.V. Yurkov. “Coherence properties of the radiation from X-ray free electron laser”. In: *Optics Communications* 281.5 (2008), pp. 1179–1188. DOI: 10.1016/j.optcom.2007.10.044

[ST03] P Suortti and W Thomlinson. “Medical applications of synchrotron radiation”. In: *Physics in Medicine and Biology* 48.13 (June 2003), R1–R35. DOI: 10.1088/0031-9155/48/13/201

[Ste+09] Daniel S. Steingrube, Tobias Vockerodt, Emilia Schulz, Uwe Morgner, and Milutin Kovačev. “Phase matching of high-order harmonics in a semi-infinite gas cell”. In: *Phys. Rev. A* 80 (4 Oct. 2009), p. 043819. DOI: 10.1103/PhysRevA.80.043819

[Sto+07] Mark I Stockman, Matthias F Kling, Ulf Kleineberg, and Ferenc Krausz. “Attosecond nanoplasmonic-field microscope”. In: *Nature Photonics* 1.9 (2007), pp. 539–544. DOI: 10.1038/nphoton.2007.169

[Sut+04] Julia R Sutherland, EL Christensen, ND Powers, SE Rhynard, JC Painter, and J Peatross. “High harmonic generation in a semi-infinite gas cell”. In: *Optics Express* 12.19 (2004), pp. 4430–4436. DOI: 10.1364/OPEX.12.004430

[Tak+02] Eiji Takahashi, Yasuo Nabekawa, Tatsuya Otsuka, Minoru Obara, and Katsumi Midorikawa. "Generation of highly coherent submicrojoule soft x rays by high-order harmonics". In: *Physical Review A* 66.2 (2002), p. 021802. DOI: 10.1103/PhysRevA.66.021802

[Tat+07] J. Tate, T. Auguste, H. G. Muller, P. Salières, P. Agostini, and L. F. DiMauro. "Scaling of Wave-Packet Dynamics in an Intense Midinfrared Field". In: *Phys. Rev. Lett.* 98 (1 Jan. 2007), p. 013901. DOI: 10.1103/PhysRevLett.98.013901

[TG09] U. Teubner and P. Gibbon. "High-order harmonics from laser-irradiated plasma surfaces". In: *Rev. Mod. Phys.* 81 (2 Apr. 2009), pp. 445–479. DOI: 10.1103/RevModPhys.81.445

[TNM02] Eiji Takahashi, Yasuo Nabekawa, and Katsumi Midorikawa. "Generation of 10-μJ coherent extreme-ultraviolet light by use of high-order harmonics". In: *Opt. Lett.* 27.21 (Nov. 2002), pp. 1920–1922. DOI: 10.1364/OL.27.001920

[Tru+18] Nguyen Xuan Truong, Reza Safaei, Vincent Cardin, Scott M Lewis, Xiang Li Zhong, François Légaré, and Melissa A Denecke. "Coherent Tabletop EUV Ptychography of Nanopatterns". In: *Scientific reports* 8.1 (2018), pp. 1–9. DOI: 10.1038/s41598-018-34257-2

[Ull+03] J Ullrich, R Moshammer, A Dorn, R D rner, L Ph H Schmidt, and H Schmidt-B cking. "Recoil-ion and electron momentum spectroscopy: reaction-microscopes". In: *Reports on Progress in Physics* 66.9 (Aug. 2003), pp. 1463–1545. DOI: 10.1088/0034-4885/66/9/203

[URM12] Joachim Ullrich, Artem Rudenko, and Robert Moshammer. "Free-electron lasers: New avenues in molecular physics and photochemistry". In: *Annual review of physical chemistry* 63 (2012), pp. 635–660. DOI: 10.1146/annurev-physchem-032511-143720

[Vil+17] DM Villeneuve, Paul Hockett, MJJ Vrakking, and Hiromichi Niikura. "Coherent imaging of an attosecond electron wave packet". In: *Science* 356.6343 (2017), pp. 1150–1153. DOI: 10.1126/science.aam8393

[Vio+21] Anne-Lise Viotti, Skirmantas Alisauskas, Ammar Bin Wahid, Prannay Balla, Nora Schirmel, Bastian Manschwetus, Ingmar Hartl, and Christoph M. Heyl. "60 fs, 1030nm FEL pump–probe laser based on a multi-pass post-compressed Yb:YAG source".

In: *Journal of Synchrotron Radiation* 28.1 (Jan. 2021), pp. 36–43. DOI: 10.1107/S1600577520015052

[Wan+00] Yingsong Wang, Yaqing Liu, Xiaodong Yang, and Zhizhan Xu. "Spectral splitting in high-order harmonic generation". In: *Phys. Rev. A* 62 (6 Nov. 2000), p. 063806. DOI: 10.1103/PhysRevA.62.063806

[WD+17] Hans Weise, Winfried Decking, et al. "Commissioning and first lasing of the European XFEL". In: *Proc. of FEL17, MOC03, Santa Fe, NM, www. JACoW. org* (2017). DOI: 10.18429/JACoW-FEL2017-MOC03

[Yam+17] Masaki Yamamoto, Kunio Hirata, Keitaro Yamashita, Kazuya Hasegawa, Go Ueno, Hideo Ago, and Takashi Kumasaka. "Protein microcrystallography using synchrotron radiation". In: *IUCrJ* 4.5 (2017), pp. 529–539. DOI: 10.1107/S2052252517008193

[Ye+20] Peng Ye et al. "Attosecond pulse generation at ELI-ALPS 100 kHz repetition rate beamline". In: *Journal of Physics B: Atomic, Molecular and Optical Physics* 53.15 (June 2020), p. 154004. DOI: 10.1088/1361-6455/ab92bf

[Yu+00] L.-H. Yu et al. "High-Gain Harmonic-Generation Free-Electron Laser". In: *Science* 289.5481 (2000), pp. 932–934. DOI: 10.1126/science.289.5481.932

[Zap+18] Ekaterina Zapolnova, Torsten Golz, Rui Pan, Karsten Klose, Siegfried Schreiber, and Nikola Stojanovic. "THz pulse doubler at FLASH: double pulses for pump–probe experiments at X-ray FELs". In: *Journal of synchrotron radiation* 25.1 (2018), pp. 39–43. DOI: 10.1107/S1600577517015442

[ZB20] Ai-Wu Zeng and Xue-Bin Bian. "Impact of Statistical Fluctuations on High Harmonic Generation in Liquids". In: *Phys. Rev. Lett.* 124 (20 May 2020), p. 203901. DOI: 10.1103/PhysRevLett.124.203901

[Zew00] Ahmed H Zewail. "Femtochemistry: Atomic-scale dynamics of the chemical bond". In: *The Journal of Physical Chemistry A* 104.24 (2000), pp. 5660–5694. DOI: 10.1021/jp001460h

[Zew94] Ahmed H. Zewail. "Femtochemistry". In: *Femtochemistry: Ultrafast Dynamics of the Chemical Bond*. 1994, pp. 3–22. DOI: 10.1142/9789814287609_0001

[Zha+20a] Chunyang Zhai, Renzhi Shao, Pengfei Lan, Bincheng Wang, Yinfu Zhang, Hua Yuan, Stephen Maina Njoroge, Lixin He, and Peixiang Lu. "Ellipticity control of high-order harmonic generation with nearly orthogonal two-color laser fields". In: *Phys. Rev. A* 101 (5 May 2020), p. 053407. DOI: 10.1103/PhysRevA.101.053407

[Zho+00] Fangchuan Zhong, Jian Deng, Xueyuan Hu, Zhong Li, Zhengquan Zhang, and Zhizhan Xu. "The effect of ionization of gases on the high harmonic splitting". In: *Physics Letters A* 278.1 (2000), pp. 35–43. DOI: 10.1016/S0375-9601(00)00746-5

[Zho+20] Guanqun Zhou, Franz-Josef Decker, Yuantao Ding, Yi Jiao, Alberto A Lutman, Timothy J Maxwell, Tor O Raubenheimer, Jiuqing Wang, Aaron J Holman, Cheng-Ying Tsai, et al. "Attosecond coherence time characterization in Hard X-Ray free-electron Laser". In: *Scientific reports* 10.1 (2020), pp. 1–8. DOI: 10.1038/s41598-020-60328-4

References Fig. 2.2 and 2.3

[1] R. Klas, S. Demmler, M. Tschernajew, S. Hädrich, Y. Shamir, A. Tünnermann, J. Rothhardt, and J. Limpert. "Table-top milliwatt-class extreme ultraviolet high harmonic light source". In: *Optica* 3.11 (Nov. 2016), pp. 1167–1170. DOI: 10.1364/OPTICA.3.001167

[2] Steffen Hädrich, Arno Klenke, Jan Rothhardt, Manuel Krebs, Armin Hoffmann, Oleg Pronin, Vladimir Pervak, Jens Limpert, and Andreas Tünnermann. "High photon flux table-top coherent extreme-ultraviolet source". In: *Nature Photonics* 8.10 (2014), pp. 779–783. DOI: 10.1038/nphoton.2014.214

[3] Steffen Hädrich, Manuel Krebs, Armin Hoffmann, Arno Klenke, Jan Rothhardt, Jens Limpert, and Andreas Tünnermann. "Exploring new avenues in high repetition rate table-top coherent extreme ultraviolet sources". In: *Light: Science & Applications* 4.8 (2015). DOI: 10.1038/lsa.2015.93

[4] Jan Rothhardt et al. "High-repetition-rate and high-photon-flux 70 eV high-harmonic source for coincidence ion imaging of gas-phase molecules". In: *Opt. Express* 24.16 (Aug. 2016), pp. 18133–18147. DOI: 10.1364/OE.24.018133

[5] Jan Rothhardt, Manuel Krebs, Steffen Hädrich, Stefan Demmler, Jens Limpert, and Andreas Tünnermann. "Absorption-limited and phase-matched high harmonic generation in the tight focusing regime". In: *New Journal of Physics* 16.3 (Mar. 2014), p. 033022. DOI: 10.1088/1367-2630/16/3/033022

[6] Amélie Cabasse, Guillaume Machinet, Antoine Dubrouil, Eric Cormier, and Eric Constant. "Optimization and phase matching of fiber-laser-

driven high-order harmonic generation at high repetition rate". In: *Opt. Lett.* 37.22 (Nov. 2012), pp. 4618–4620. DOI: 10.1364/OL.37.004618

[7] A Comby et al. "Bright, polarization-tunable high repetition rate extreme ultraviolet beamline for coincidence electron–ion imaging". In: *Journal of Physics B: Atomic, Molecular and Optical Physics* 53.23 (Nov. 2020), p. 234003. DOI: 10.1088/1361-6455/abbe27

[8] Maxim Tschernajew et al. "High Repetition Rate High Harmonic Generation with Ultra-high Photon Flux". In: *Laser Congress 2020 (ASSL, LAC)*. Optical Society of America, 2020, JTh2A.21. DOI: 10.1364/ASSL.2020.JTh2A.21

[9] A Comby, D Descamps, S Beauvarlet, A Gonzalez, F Guichard, S Petit, Y Zaouter, and Y Mairesse. "Cascaded harmonic generation from a fiber laser: a milliwatt XUV source". In: *Optics express* 27.15 (2019), pp. 20383–20396. DOI: 10.1364/OE.27.020383

[10] E. Constant, D. Garzella, P. Breger, E. Mével, Ch. Dorrer, C. Le Blanc, F. Salin, and P. Agostini. "Optimizing High Harmonic Generation in Absorbing Gases: Model and Experiment". In: *Phys. Rev. Lett.* 82 (8 Feb. 1999), pp. 1668–1671. DOI: 10.1103/PhysRevLett.82.1668

[11] Eleonora Lorek, Esben Witting Larsen, Christoph Michael Heyl, Stefanos Carlström, David Paleček, Donatas Zigmantas, and Johan Mauritsson. "High-order harmonic generation using a high-repetition-rate turnkey laser". In: *Review of Scientific Instruments* 85.12 (2014), p. 123106. DOI: 10.1063/1.4902819

[12] A. Willner et al. "Coherent Control of High Harmonic Generation via Dual-Gas Multijet Arrays". In: *Phys. Rev. Lett.* 107 (17 Oct. 2011), p. 175002. DOI: 10.1103/PhysRevLett.107.175002

[13] Florian Emaury, Andreas Diebold, Clara J Saraceno, and Ursula Keller. "Compact extreme ultraviolet source at megahertz pulse repetition rate with a low-noise ultrafast thin-disk laser oscillator". In: *Optica* 2.11 (2015), pp. 980–984. DOI: 10.1364/OPTICA.2.000980

[14] Chengyuan Ding, Wei Xiong, Tingting Fan, Daniel D. Hickstein, Tenio Popmintchev, Xiaoshi Zhang, Mike Walls, Margaret M. Murnane, and Henry C. Kapteyn. "High flux coherent super-continuum soft X-ray source driven by a single-stage, 10mJ, Ti:sapphire amplifier-pumped OPA". In: *Opt. Express* 22.5 (Mar. 2014), pp. 6194–6202. DOI: 10.1364/OE.22.006194

[15] Vinzenz Hilbert, Maxim Tschernajew, Robert Klas, Jens Limpert, and Jan Rothhardt. "A compact, turnkey, narrow-bandwidth, tunable, and high-photon-flux extreme ultraviolet source". In: *AIP Advances* 10.4 (2020), p. 045227. DOI: 10.1063/1.5133154

[16] Anne Harth et al. "Compact 200 kHz HHG source driven by a few-cycle OPCPA". In: *Journal of Optics* 20.1 (Dec. 2017), p. 014007. DOI: 10.1088/2040-8986/aa9b04

[17] Michele Puppin, Yunpei Deng, CW Nicholson, Johannes Feldl, NBM Schröter, Hendrik Vita, PS Kirchmann, Claude Monney, Laurenz Rettig, Martin Wolf, et al. "Time-and angle-resolved photoemission spectroscopy of solids in the extreme ultraviolet at 500 kHz repetition rate". In: *Review of Scientific Instruments* 90.2 (2019), p. 023104. DOI: 10.1063/1.5081938

[18] Jan Rothhardt, Steffen Hädrich, Arno Klenke, Stefan Demmler, Armin Hoffmann, Thomas Gotschall, Tino Eidam, Manuel Krebs, Jens Limpert, and Andreas Tünnermann. "53 W average power few-cycle fiber laser system generating soft x rays up to the water window". In: *Optics letters* 39.17 (2014), pp. 5224–5227. DOI: 10.1364/OL.39.005224

[19] Martin Gebhardt, Tobias Heuermann, Ziyao Wang, Mathias Lenski, Christian Gaida, Robert Klas, Alexander Kirsche, Steffen Hädrich, Jan Rothhardt, and Jens Limpert. "Soft x-ray high order harmonic generation driven by high repetition rate ultrafast thulium-doped fiber lasers". In: *Fiber Lasers XVII: Technology and Systems*. Ed. by Liang Dong. Vol. 11260. International Society for Optics and Photonics. SPIE, 2020, pp. 84–89. DOI: 10.1117/12.2546151

[20] R. Klas, A. Kirsche, M. Gebhardt, J. Buldt, H. Stark, S. Hädrich, J. Rothhardt, and J. Limpert. *Ultra-short-pulse high-average-power Megahertz-repetition-rate coherent extreme-ultraviolet light source*. 2020

[21] Ioachim Pupeza, Simon Holzberger, T Eidam, Henning Carstens, D Esser, J Weitenberg, P Rußbüldt, Jens Rauschenberger, J Limpert, Th Udem, et al. "Compact high-repetition-rate source of coherent 100 eV radiation". In: *Nature Photonics* 7.8 (2013), pp. 608–612. DOI: 10.1038/nphoton.2013.156

[22] Chuankun Zhang, Stephen B. Schoun, Christoph M. Heyl, Gil Porat, Mette B. Gaarde, and Jun Ye. "Noncollinear Enhancement Cavity for Record-High Out-Coupling Efficiency of an Extreme-UV Frequency Comb". In: *Phys. Rev. Lett.* 125 (9 Aug. 2020), p. 093902. DOI: 10.1103/PhysRevLett.125.093902

[23] Akira Ozawa, Zhigang Zhao, Makoto Kuwata-Gonokami, and Yohei Kobayashi. "High average power coherent vuv generation at 10 MHz repetition frequency by intracavity high harmonic generation". In: *Opt. Express* 23.12 (June 2015), pp. 15107–15118. DOI: 10.1364/OE.23.015107

[24] H. Carstens et al. "High-harmonic generation at 250 MHz with photon energies exceeding 100 eV". In: *Optica* 3.4 (Apr. 2016), pp. 366–369. DOI: 10.1364/OPTICA.3.000366

[25] Tobias Saule, Stephan Heinrich, Johannes Schötz, Nicolai Lilienfein, Maximilian Högner, O deVries, M Plötner, Johannes Weitenberg, D Esser, J Schulte, et al. "High-flux ultrafast extreme-ultraviolet photoemission spectroscopy at 18.4 MHz pulse repetition rate". In: *Nature communications* 10.1 (2019), pp. 1–10. DOI: 10.1038/s41467-019-08367-y

[26] Gil Porat, Christoph M Heyl, Stephen B Schoun, Craig Benko, Nadine Dörre, Kristan L Corwin, and Jun Ye. "Phase-matched extreme-ultraviolet frequency-comb generation". In: *Nature Photonics* 12.7 (2018), pp. 387–391. DOI: 10.1038/s41566-018-0199-z

[27] Natsuki Kanda, Tomohiro Imahoko, Koji Yoshida, Akihiro Tanabashi, A Amani Eilanlou, Yasuo Nabekawa, Tetsumi Sumiyoshi, Makoto Kuwata-Gonokami, and Katsumi Midorikawa. "Opening a new route to multiport coherent XUV sources via intracavity high-order harmonic generation". In: *Light: Science & Applications* 9.1 (2020), pp. 1–9. DOI: 10.1038/s41377-020-00405-5

[28] James S Feehan, Jonathan HV Price, Thomas J Butcher, William S Brocklesby, Jeremy G Frey, and David J Richardson. "Efficient high-harmonic generation from a stable and compact ultrafast Yb-fiber laser producing 100 μJ, 350 fs pulses based on bendable photonic crystal fiber". In: *Applied Physics B* 123.1 (2017), p. 43. DOI: 10.1007/s00340-016-6620-8

[29] Thomas RM Barends, Lutz Foucar, Albert Ardevol, Karol Nass, Andrew Aquila, Sabine Botha, R Bruce Doak, Konstantin Falahati, Elisabeth Hartmann, Mario Hilpert, et al. "Direct observation of ultrafast collective motions in CO myoglobin upon ligand dissociation". In: *Science* 350.6259 (2015), pp. 445–450. DOI: 10.1126/science.aac5492

[30] Kanupriya Pande, Christopher DM Hutchison, Gerrit Groenhof, Andy Aquila, Josef S Robinson, Jason Tenboer, Shibom Basu, Sébastien Boutet, Daniel P DePonte, Mengning Liang, et al. "Femtosecond structural dynamics drives the trans/cis isomerization in photoactive yellow

protein". In: *Science* 352.6286 (2016), pp. 725–729. DOI: 10.1126/science.aad5081

[31] Jesse N Clark, Loren Beitra, Gang Xiong, David M Fritz, Henrik T Lemke, Diling Zhu, Matthieu Chollet, Garth J Williams, Marc M Messerschmidt, Brian Abbey, et al. "Imaging transient melting of a nanocrystal using an X-ray laser". In: *Proceedings of the National Academy of Sciences* 112.24 (2015), pp. 7444–7448. DOI: 10.1073/pnas.1417678112

[32] P Radcliffe, S Düsterer, A Azima, H Redlin, J Feldhaus, John Dardis, K Kavanagh, H Luna, J Pedregosa Gutierrez, Patrick Yeates, et al. "Single-shot characterization of independent femtosecond extreme ultraviolet free electron and infrared laser pulses". In: *Applied physics letters* 90.13 (2007), p. 131108. DOI: 10.1063/1.2716360

[33] Kasra Amini, Rebecca Boll, Alexandra Lauer, Michael Burt, Jason WL Lee, Lauge Christensen, Felix Brauβe, Terence Mullins, Evgeny Savelyev, Utuq Ablikim, et al. "Alignment, orientation, and Coulomb explosion of difluoroiodobenzene studied with the pixel imaging mass spectrometry (PImMS) camera". In: *The Journal of chemical physics* 147.1 (2017), p. 013933. DOI: 10.1063/1.4982220

[34] Georg Schmid, Kirsten Schnorr, Sven Augustin, Severin Meister, Hannes Lindenblatt, Florian Trost, Yifan Liu, Tsveta Miteva, Mathieu Gisselbrecht, Stefan Düsterer, et al. "Tracing charge transfer in argon dimers by XUV-pump IR-probe experiments at FLASH". In: *The Journal of chemical physics* 151.8 (2019), p. 084314. DOI: 10.1063/1.5116234

[35] Gareth O Williams, S Künzel, S Daboussi, B Iwan, AI Gonzalez, W Boutu, V Hilbert, U Zastrau, HJ Lee, B Nagler, et al. "Tracking the ultrafast XUV optical properties of x-ray free-electron-laser heated matter with high-order harmonics". In: *Physical Review A* 97.2 (2018), p. 023414. DOI: 10.1103/PhysRevA.97.023414

[36] Friedrich Roth et al. "Direct observation of charge separation in an organic light harvesting system by femtosecond time-resolved XPS". In: *Nature Communications* 12.1 (Feb. 2021), p. 1196. DOI: 10.1038/s41467-021-21454-3

[37] E. Allaria et al. "Two-colour pump–probe experiments with a twin-pulse-seed extreme ultraviolet free-electron laser". In: *Nature Communications* 4.1 (Sept. 2013), p. 2476. DOI: 10.1038/ncomms3476

[38] Elisa Biasin et al. “Direct observation of coherent femtosecond solvent reorganization coupled to intramolecular electron transfer”. In: *Nature Chemistry* (Feb. 2021). DOI: 10.1038/s41557-020-00629-3

[39] Thomas Ding et al. “XUV pump–XUV probe transient absorption spectroscopy at FELs”. In: *Faraday Discuss.* (2021). DOI: 10.1039/D0FD00107D

Acknowledgements

I would like to express my gratitude for the many people who contributed to this work and supported me along the past few years. First of all, many thanks to my supervisor, Milutin Kovačev, who has guided me during the good and bad times of my PhD work. I am grateful to him and to Uwe Morgner for giving me the opportunity to work on this interesting project and for welcoming me in their research group. I would like to extend my thanks also to Robert Moshammer for promoting and supporting this project as part of the developments of the REMI endstation.

In addition, this work would not have been possible without the involvement of many people at DESY. Thanks to Ingmar Hart, Tino Lang, Bastian Manschwetus and Christoph Heyl for the time spent in countless SynVLiFL meetings and the efforts made since the early stages of the project. A special thanks to Skirmantas Ališauskas, who always supported me and shared his competence and experience. It has been a pleasure working with you. Surely I can not fully express my appreciation for my "partner in crime", Christina Papadopoulou, who has been a vital part of this work for the last three years. Thank you for everything you have done, for all the work together, for the many holidays and long weekends spent alone at the beamline. I am truly grateful for your tireless work and true friendship.

An equal genuine thanks to Josè Louise Mapa for all his work on the technical design and his dedication to the project. We started from scratch and improved our knowledge step by step along the way. Thank you. I also had great pleasure in working with Maciej Brachmanski and Markus Braune. Your contributions and expertises have been essential for the design and installation

of the setup. Many thanks also to Hannes Lindenblatt, Florian Trost and Severin Meister from MPI in Heidelberg for their contribution in the REMI measurements and the many technical discussions on the beamline design.

My sincere thanks to all the AGMorgner in Hannover, especially to the "downstairs guys" for an inspiring and friendly workplace. Above all, my gratitude goes to Christoph Jusko and Philip Mosel for all the time spent together in and outside the laboratory between untamable dragons, summer travels to DESY and endless discussions. Christoph, you were present since day one and kept me going until the end. Thank you for being my companion in this journey.

I am also extremely grateful for the support and love of my friends and family. To the always inspiring Maria Elena and to the PhD wanderers Silvia, Giulia and Ugo, thank you for your positive contribution to my mental health! Many thanks to my family which has been always encouraging and never doubted my success. Mamma, papà, Nenna, Marco, Francy e Berni grazie del vostro sostegno e di farmi sentire (volente o meno) la vostra presenza. Un grazie speciale a Frida e Sebastiano che mi ricordano come guardare alle cose nella giusta prospettiva. Finally, thanks to my favorite postdoc-laboratory buddy-supporter-reviewer-editor-husband, Giorgio. I am forever grateful for everything you have done and your constant support.

Vielen Dank!